GEORGIA INSTITUTE OF TECHNOLOGY
OFFICE OF CONTRACT ADMINISTRATION
SPONSORED PROJECT INITIATION

Date: *April 9, 1979*

Project Title: *Investigation of the Effects of Microstructure on the Deformation Modes & Mechanical Properties of Ti-6Al-2Cb-1Ta-0.8Mo.*

Project No: *E-19-678* Green card

Project Director: *Dr. E. A. Starke, Jr.*

Sponsor: *Office of Naval Research*

Agreement Period: From *2/1/79* Until *1/31/83* ~~*1/31/81*~~ *(R&D Period)*

Type Agreement: *Contract No. N00014-79-C-0207*

Amount: *$125,000 (Partially funded at $60,000 through 1/31/80)*

Reports Required: *Progress Reports, Final Report*

Sponsor Contact Person (s):

Technical Matters

Director, Metallurgy & Ceramics Program
Materials Sciences Division
Office of Naval Research
800 North Quincy Street
Arlington, VA 22217

Contractual Matters
(thru OCA)

Office of Naval Research
Resident Representative
325 Hinman Research Building
Georgia Institute of Technology
Atlanta, GA 30332

Defense Priority Rating: *DO-C9 under DMS Reg. 1*

Assigned to: *Chemical Engineering* (School/Laboratory)

COPIES TO:

- Project Director
- Division Chief (EES)
- School/Laboratory Director
- Dean/Director–EES
- Accounting Office
- Procurement Office
- Security Coordinator (OCA)
- Reports Coordinator (OCA)
- Library, Technical Reports Section
- EES Information Office
- EES Reports & Procedures
- Project File (OCA)
- Project Code (GTRI)
- Other _____

CA–3 (3/76)

GEORGIA INSTITUTE OF TECHNOLOGY OFFICE OF CONTRACT ADMINISTRATION

SPONSORED PROJECT TERMINATION/CLOSEOUT SHEET

Date January 13, 1984

Project No. E-19-678 School/~~Lab~~ Chemical Engr.

Includes Subproject No.(s)

Project Director(s) Dr. E. A. Starke, Jr. GTRI / ~~GIT~~

Sponsor Office of Naval Research

Title "Investigation of the Effects of Microstructure on the Deformation Modes and Mechanical Properties of Ti-6Al-2Cb-1 Ta-0.3 mo.

Effective Completion Date: 1/31/83 (Performance) 5/31/83 (Reports)

Grant/Contract Closeout Actions Remaining:

- [X] None
- [ ] Final Invoice or Final Fiscal Report
- [ ] Closing Documents
- [ ] Final Report of Inventions
- [ ] Govt. Property Inventory & Related Certificate
- [ ] Classified Material Certificate
- [ ] Other

Continues Project No. Continued by Project No.

COPIES TO:

Project Director
Research Administrative Network
Research Property Management
Accounting
Procurement/EES Supply Services
Research Security Services
Reports Coordinator (OCA)
Legal Services

Library
GTRI
Research Communications (2)
Project File
Other

Form OCA 60:1028

E-19-678

SIX MONTH SUMMARY REPORT

THE OFFICE OF NAVAL RESEARCH
CONTRACT NO. N00014-79-C-0207

The attached is a summary report which briefly describes the background, objectives, programs, conclusions and future plans of our research, "Investigation of the Effects of Microstructure on the Deformation Modes and Mechanical Properties of Ti-6Al-2Nb-Ta-0.8Mo." The report is primarily concerned with progress since our last report which was dated October, 1979 and is in the format presented at the Second Review on the ONR Ti-100 Materials Technology held at the Naval Academy, Annapolis, MD, 25-26 June 1980. A brief description will be given for each slide when they are not self-explanatory.

Edgar A. Starke, Jr.
Principal Investigator

SLIDE 1

INVESTIGATION OF THE EFFECTS OF MICROSTRUCTURE ON THE DEFORMATION MODES AND MECHANICAL PROPERTIES OF Ti-6Al-2Nb-1Ta-0.8Mo

OBJECTIVE: TO QUANTIFY THE MICROSTRUCTURE, DETERMINE THE DEFORMATION MODES AND BEHAVIOR OF TI-6211, AND ESTABLISH FUNCTIONAL RELATIONSHIPS BETWEEN THESE FACTORS.

RESEARCHERS: S.B. CHAKRABORTTY
A. GYSLER
F.S. LIN
E.A. STARKE, JR.

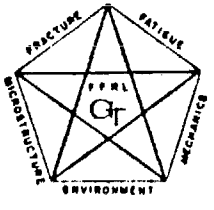

REVIEW OF FIRST SIX MONTH MEETING

As-Received Microstructure-Widmanstätten $\alpha+\beta$

Microstructure Modifications by HT and Slow Cool.

1. Changed prior β grain size
2. Changed thickness of α in prior βGB
3. Changed size of α
4. Changed shape of α
5. Changed Widmanstätten Colony Size

Features kept constant

1. Volume fraction of β
2. Chemical composition of α and β

SLIDE 3

RESULTS OF INITIAL STUDY

1. Heat treatments had **little** effect on YS and UTS.
   Reasons:
   (a) Strength of phases constant since composition constant.
   (b) Volume fraction of α and β constant.

2. Heat treatments had **large** effect on ductility and fracture mode.
   Reasons:
   (a) morphology and distribution of phases control strain distribution.
   (b) features that lead to strain localization decrease ductility.

3. Heat treatments above β transus greatly reduced ductility.
   Reason: α phase at prior β-grain boundaries lead to strain localization in this region.

Results suggest that increase in strength with no loss in ductility may be obtained by:

1. Eliminating excursions above the β transus temperature during heat treatment.

2. Changing major deformation barrier from colony boundary to α/β interface boundary.

3. Increasing the volume fraction of β phase by holding at selectively higher temperatures within the alpha-beta phase field.

4. Quenching to transform β into martensite and super-saturate aluminum in α phase.

5. Aging at low temperature to precipitate Ti_3Al and strengthen the α phase.

SLIDE 5

As an aid in selecting the heat treatments for this experimental program the equilibrium volume fraction of the beta phase was determined as a function of temperature from 700°C to the alpha-beta transus. As-received samples were heated to 1050° and held for 40 minutes. They were then cooled at 1°C/minute to a preselected temperature and quenched in water. The volume fraction of the beta phase was determined from both scanning and transmission electron micrographs.

SLIDE 5

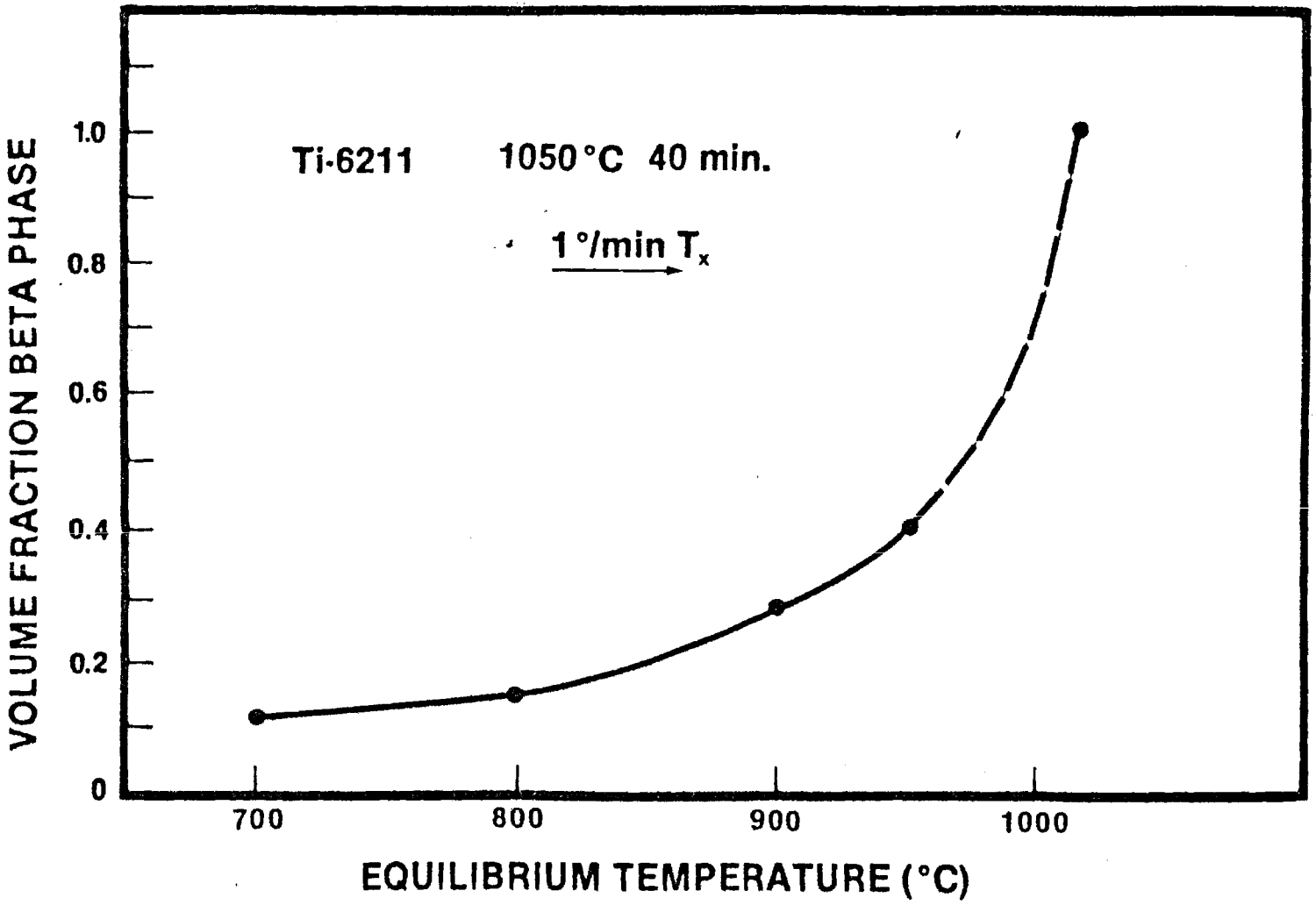
Ti-6211 1050°C 40 min.
1°/min T_x
VOLUME FRACTION BETA PHASE
0
0.2
0.4
0.6
0.8
1.0
700
800
900
1000
EQUILIBRIUM TEMPERATURE (°C)

SLIDE 6

Shows the monotonic properties of six different treatments. The heat treatment temperature was varied from 800°C to 1050°C. The HT time was 40 minutes--which had been found sufficient to reach equilibrium conditions. An aging treatment of two hours at 500°C was given to all samples. However, samples from two quenching temperatures--800°C and 950°C were also tested in the as-quenched condition.

SLIDE 6

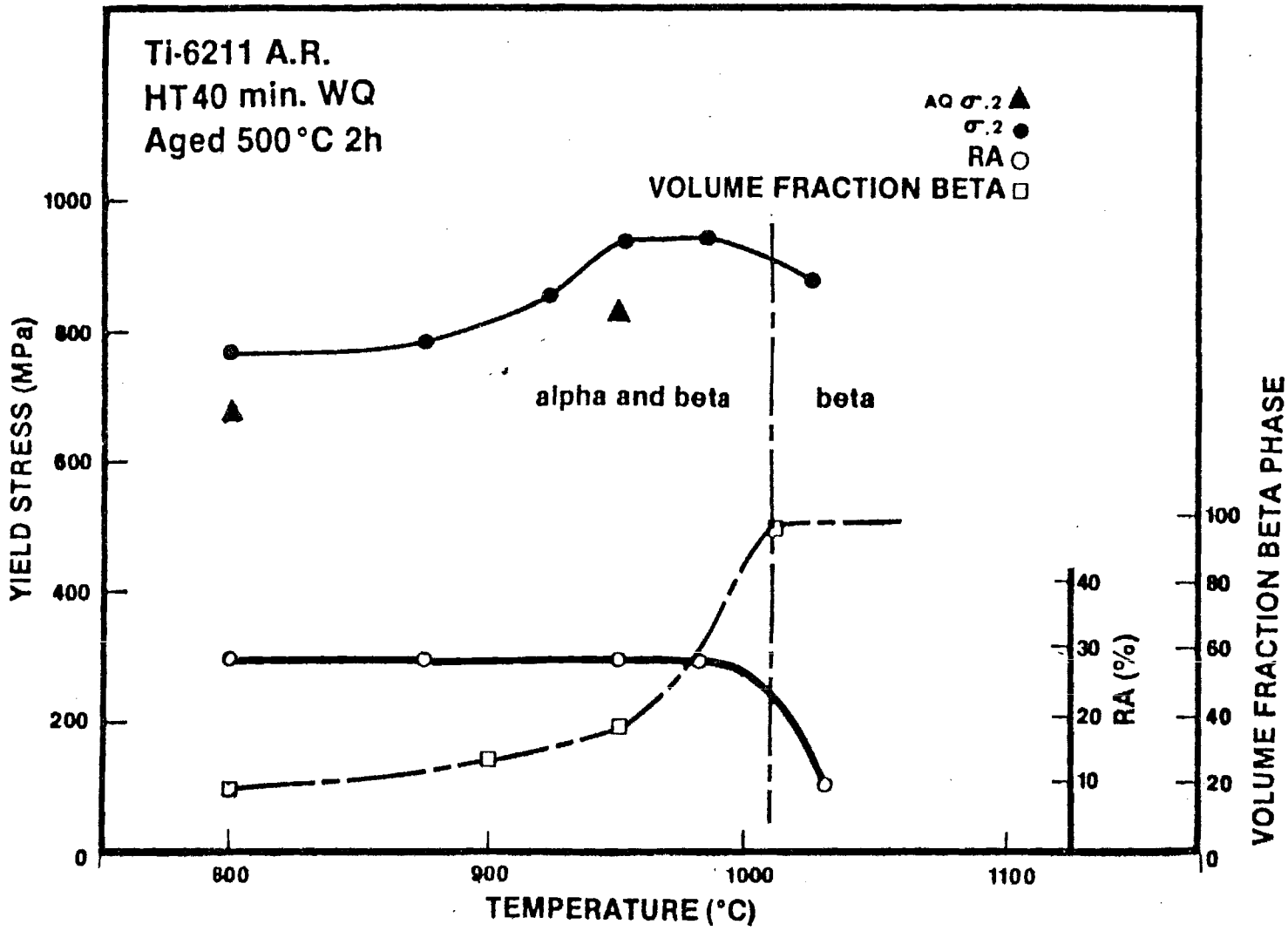
Ti-6211 A.R.
HT40 min. WQ
Aged 500°C 2h
AQ σ.2 ▲
σ.2 ●
RA ○
VOLUME FRACTION BETA □
alpha and beta
beta
YIELD STRESS (MPa)
1000
800
600
400
200
0
RA (%)
40
30
20
10
VOLUME FRACTION BETA PHASE
100
80
60
40
20
0
800
900
1000
1100
TEMPERATURE (°C)

SLIDE 7

This shows the microstructure of the 800°C samples and 950°C sample. The beta phase for the 800°C treatment is discontinuous and represents about 15 volume percent. The 950°C samples has about 40 volume percent transformed beta (martensite) and the transformed beta is continuous.

SLIDE 7

Ti-6Al-2Nb-1Ta-0.8Mo

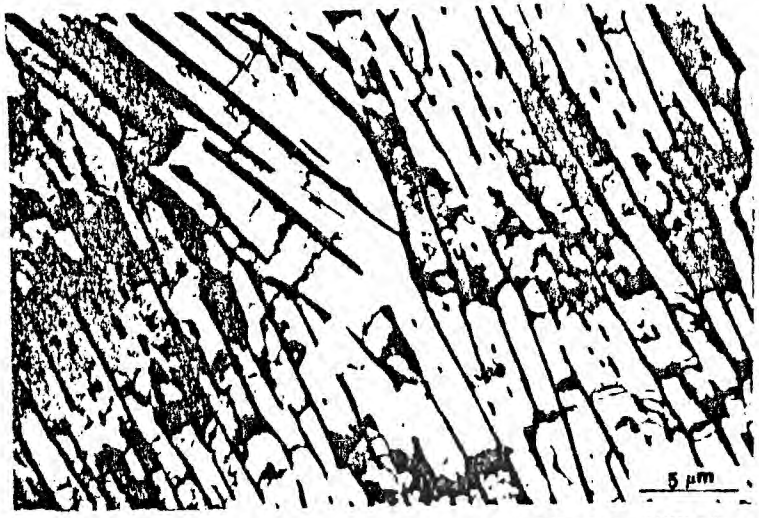

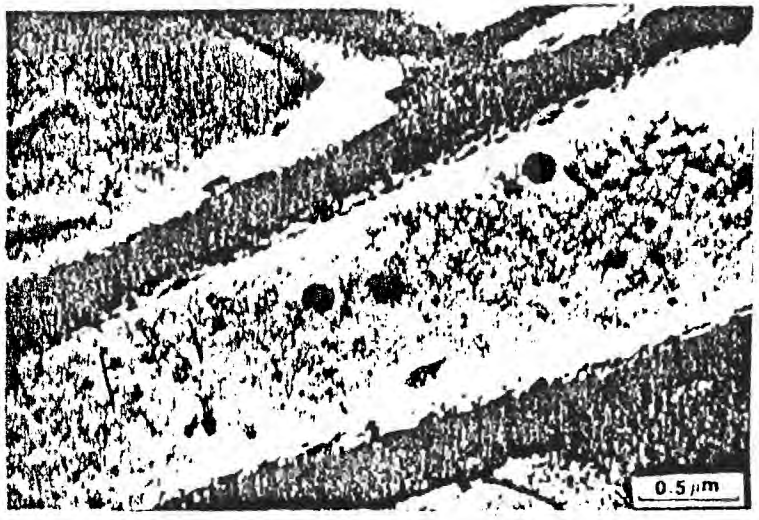

HT 800 °C 40 min. WQ Aged 500 °C 2h

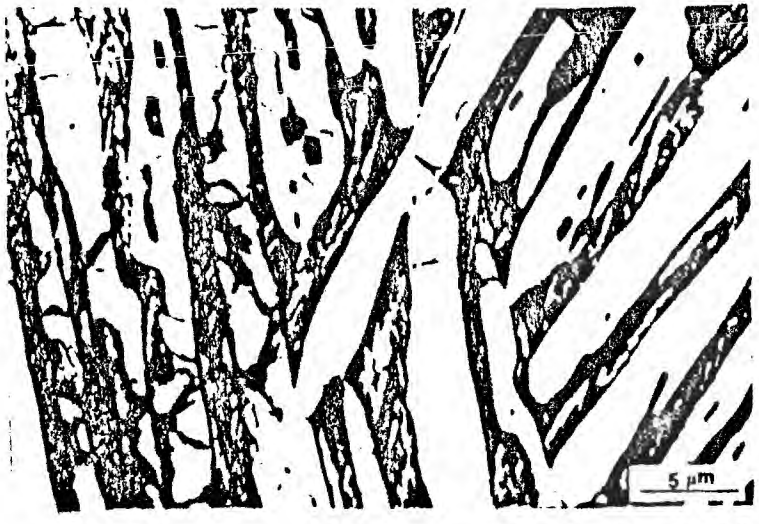

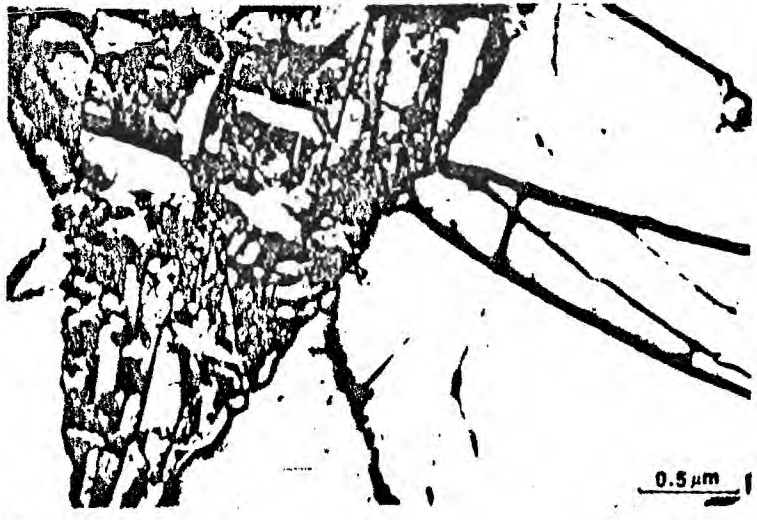

HT 950 °C 40 min. WQ Aged 500 °C 2h

SLIDE 8

This shows the deformation structure of the 800°C and 950°C HT samples. The 800°C sample shows fine planar slip which covers an entire colony. The beta phase is not a major barrier to slip and slip is continuous through the beta phase. The 950°C sample also shows relatively homogeneous slip, but the transformed beta is a major barrier to slip. The slip length for the 800°C HT is determined by the colony size, but for the 950°C it is determined by the spacing between the beta phase.

SLIDE 8

Ti-6Al-2Nb-1Ta-0.8Mo

DEFORMATION STRUCTURES

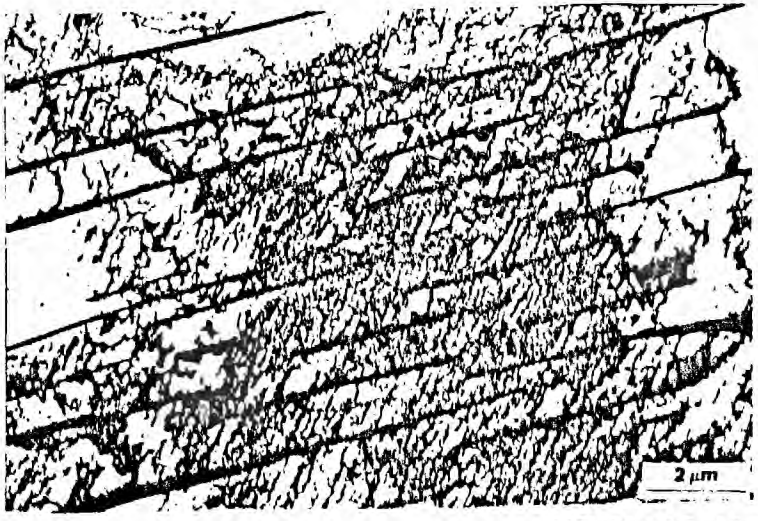

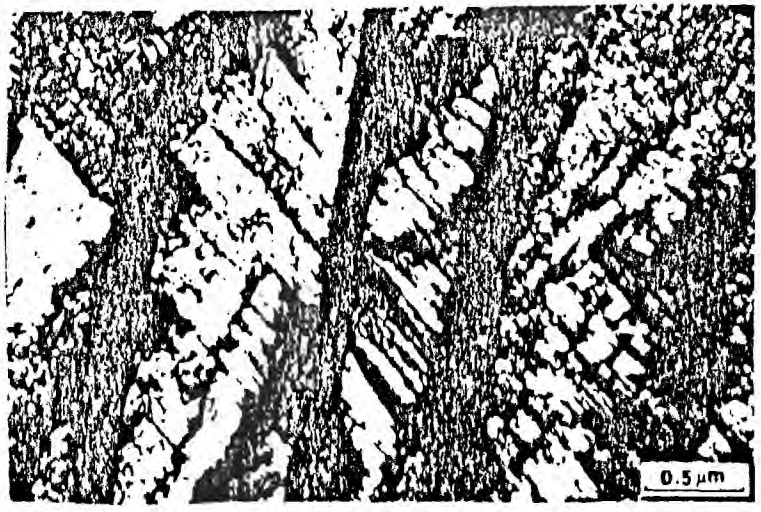

HT 800 °C 40 min. WQ Aged 500 °C 2h

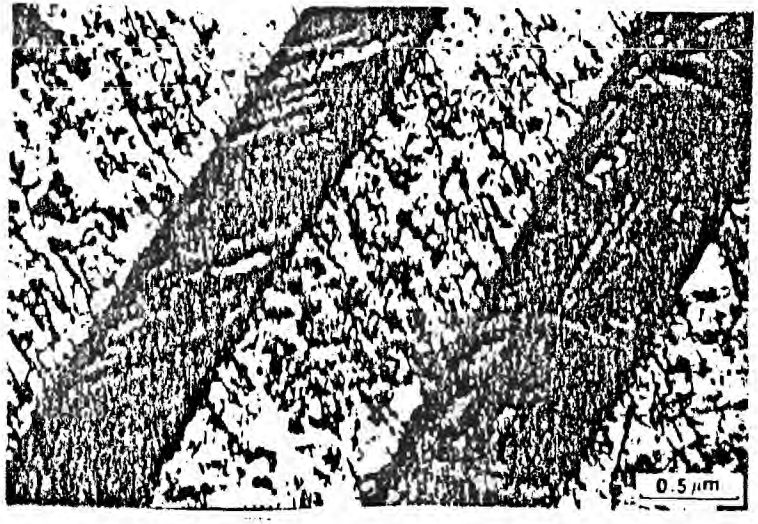

HT 950 °C 40 min. WQ Aged 500 °C 2h

SLIDE 9

This slide shows the yield strength as a function of slip length. The slip length is taken as the colony size for the 800°C HT and the beta spacing for the 950°C HT. The data are superimposed on a curve taken from a paper by C. R. Yoder, L. A. Cooley and T. W. Crooker, Trans. of the ASME, 101 (1979) pp. 86-90. The solid points are from other Ti-alloys.

SLIDE 9

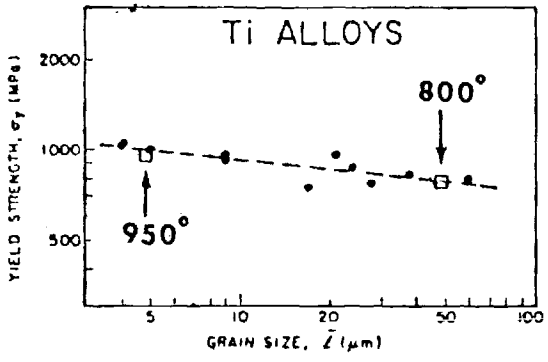
Ti ALLOYS
800°
950°
2000
1000
500
5
10
20
50
100
YIELD STRENGTH, σ_y (MPa)
GRAIN SIZE, $\bar{\ell}$ (μm)

SLIDE 10

Explanation of strength differences obtained by quenching from 800 °C and 950 °C and subsequent aging at 500 °C.

1. The volume fraction of β increases when going from 800 °C to 950 °C.

2. (a) the β from 800 °C is discontinuous and the slip length in α is greater than the average α plate thickness.
   (b) The β from 950 °C is continuous and the slip length in α is determined by the α plate thickness.

3. The β from 950 °C transforms to a stronger martensite during quenching while that from 800 °C does not. (however, some β transforms to martensite during deformation.)

4. The strength increase obtained by aging at 500 °C. is due to precipitation of Ti_3Al.

SLIDES 11 and 12

These slides illustrate the effect on the fracture behavior and ductility when samples are HT above and below the beta transus. Slide 11 shows the microstructure and fractographs of a sample HT below the beta transus (950°C) and is representative of the samples of this group. Deformation is relatively homogeneous and fracture occurs at α/β interfaces. Slide 12 shows the microstructure and fractographs of a sample HT above the beta transus (1050°C). Deformation is very localized in the alpha phase along prior beta grain boundaries and although the fracture surface shows ductile features, extensive strain localization has resulted in a low elongation to fracture and reduction in area.

SLIDE 11

Ti-6Al-2Nb-1Ta-0.8Mo

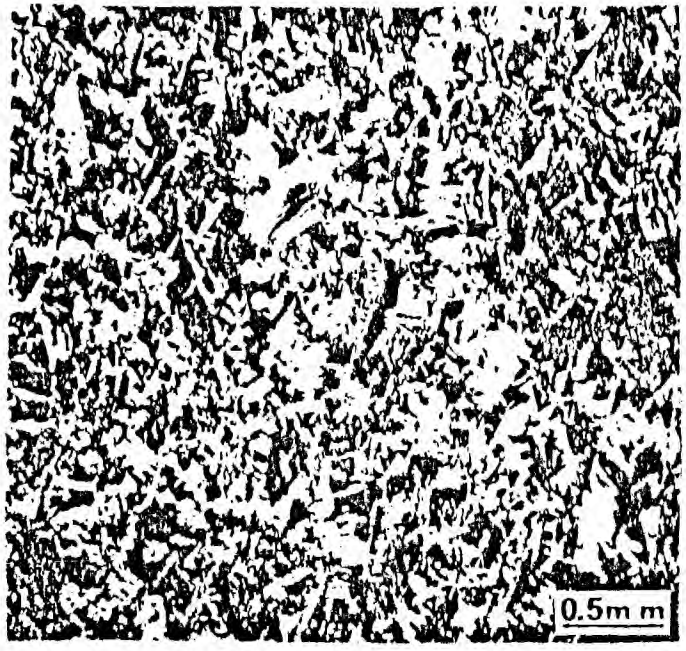

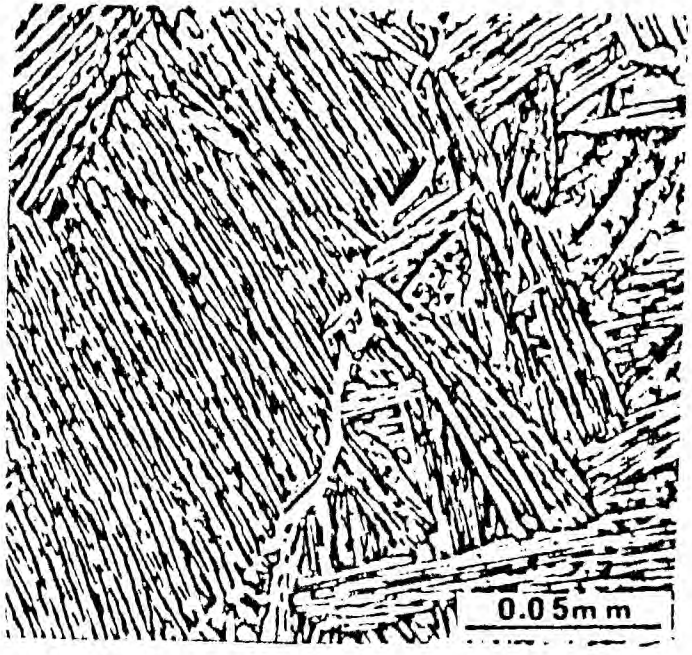

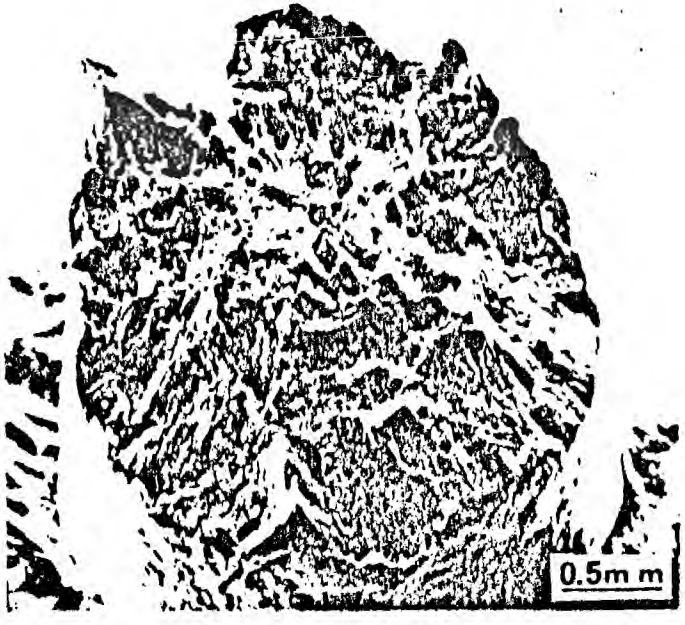

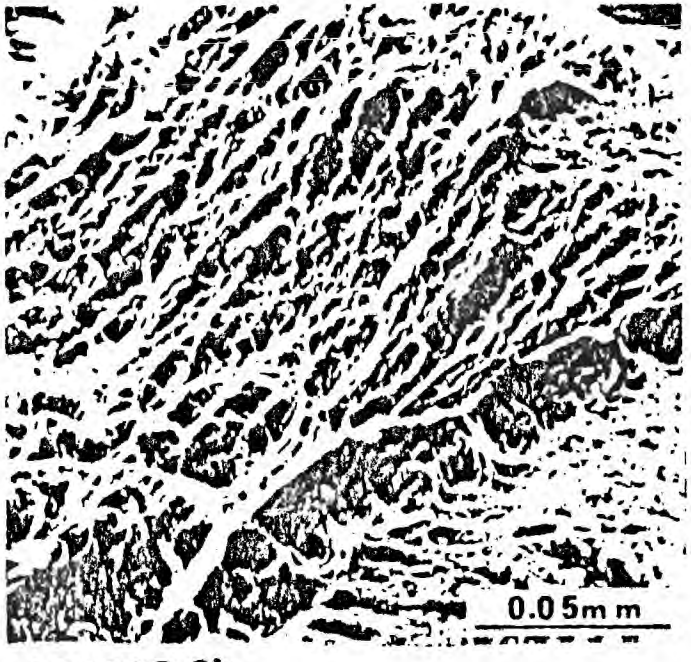

HT 950 °C 40 min. WQ Aged 500 °C 2h

Ti-6Al-2Nb-1Ta-0.8Mo

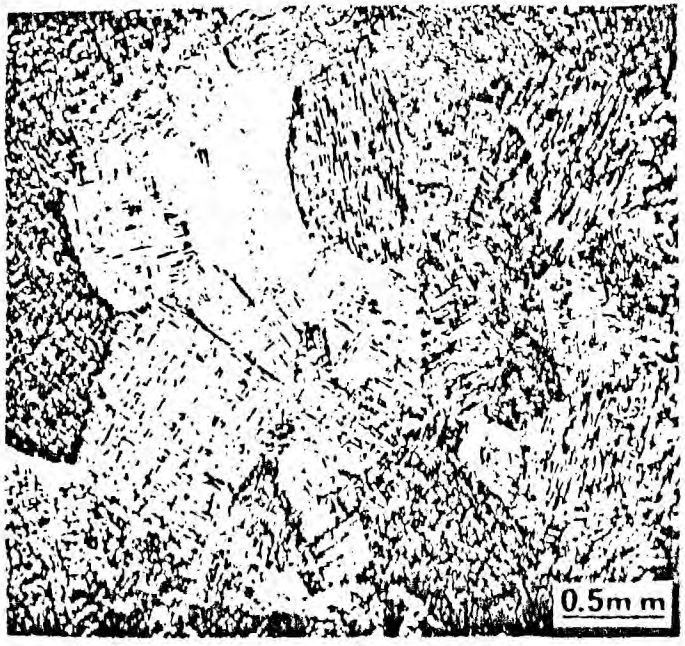

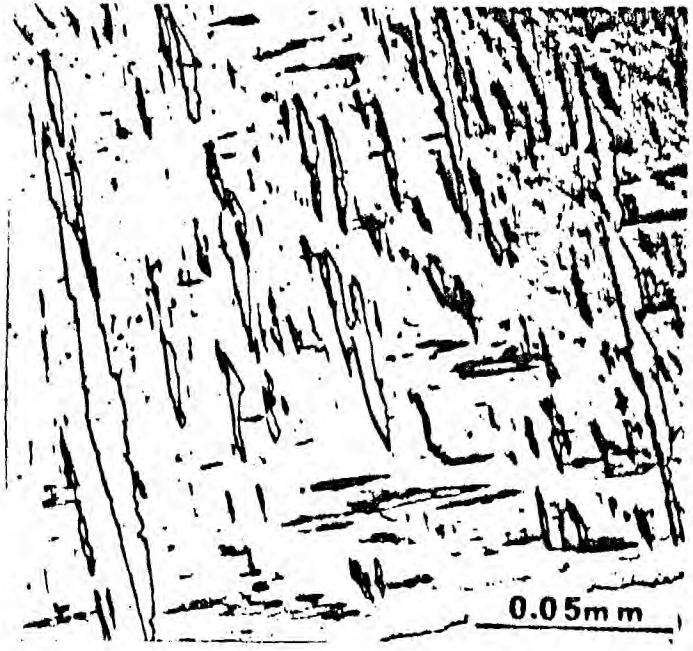

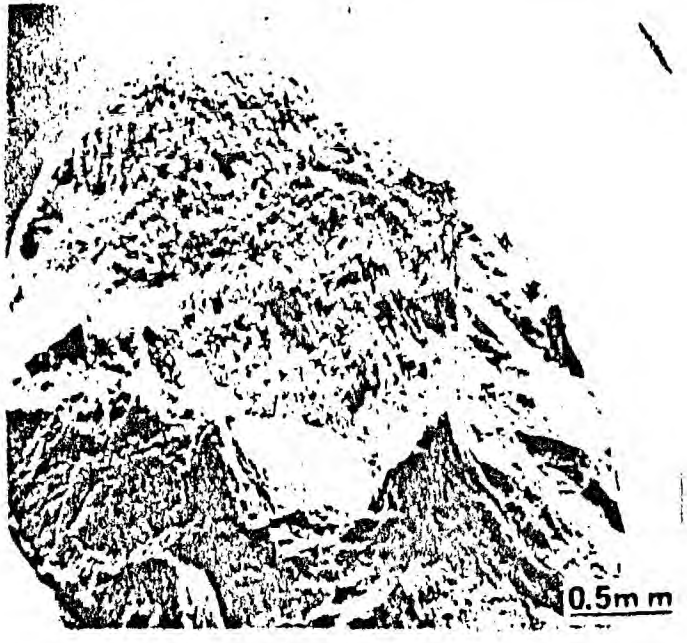

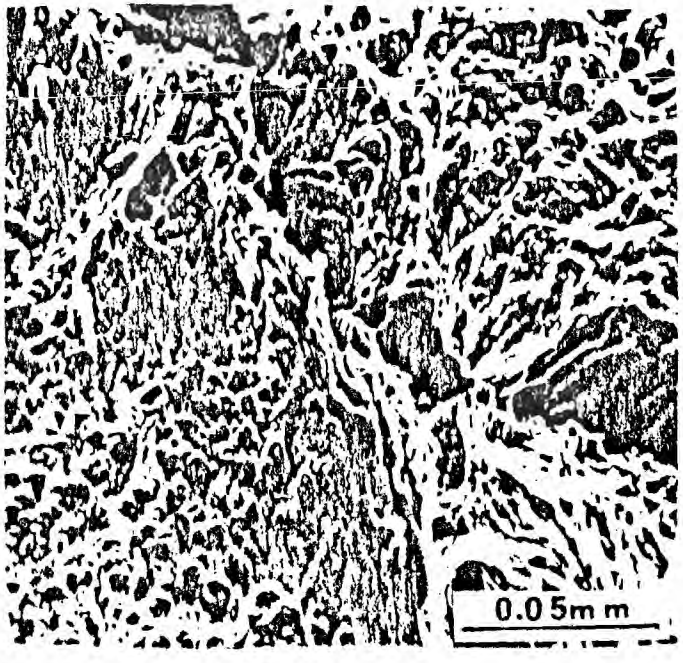

HT 1050 °C 40 min. WQ Aged 500 °C 2h

SLIDE 13

This slide shows the effect of oxygen on the mechanical properties of Ti-6211, HT at 800°C and 950°C. Oxygen produces an increment of solid solution strengthening which is essentially constant, irrespective of the HT used, i.e. $\sim$ 50 MPa for 0.1 weight percent oxygen.

EFFECT OF OXYGEN CONCENTRATION
TENSILE STRENGTH (MPa)
ELONGATION AND DUCTILITY
ANNEALING TEMPERATURE (°C)
AQ
AGED
0.07
0.17

SLIDE 14

SUMMARY OF RESULTS ON MODIFICATION OF WIDMANSTATTEN - ALPHA AND BETA

1. A significant improvement in strength with no loss in ductility can be obtained by quenching from 950 °C and aging at 500 °C.
   950 °C — continuous β transforms to martensite on quenching. Increase in strength over the AR-Ti-6211 of 80 MPa.
   500 °C age — precipitates Ti_3Al — increases strength 100MPa over as quenched alloy. Total improvement 180 MPa with no loss in ductility.

2. Excursions above $\alpha + \beta$ transus greatly reduces the ductility by changing the fracture path from α/β interface to prior β grain boundaries.

3. Increasing the oxygen content from 0.07% to 0.17% can account for an increase in strength of ~ 50 MPa with only a very minor loss in ductility.

SLIDE 15

MICROSTRUCTURE AND TEXTURE MODIFICATION

As-Received Widmanstätten $\alpha + \beta$ was β processed — Random Texture — Von Mises Treatment should predict yielding under combined stress.

$\alpha+\beta$ Processing — can obtain strong texture and equiaxed microstructure.

Strong texture may inhibit through thickness straining when used for a pressure vessel.

Equiaxed microstructure should have high ductility and good FCI Resistance.

SLIDE 16

The experimental determination of the yield locus for Ti-6211 as-received and TMT processed followed that described by D. Lee and W. A. Backofen, Trans. of the Metallurgical Society of AIME, 236 (1966) pp. 1077-1084. Slide 16 is taken from their paper. Path 5 represents through thickness compression and is essentially the stress for a spherical pressure vessel. Path 5 would be somewhat similar to the stress system for a cylindrical pressure vessel.

SLIDE 16

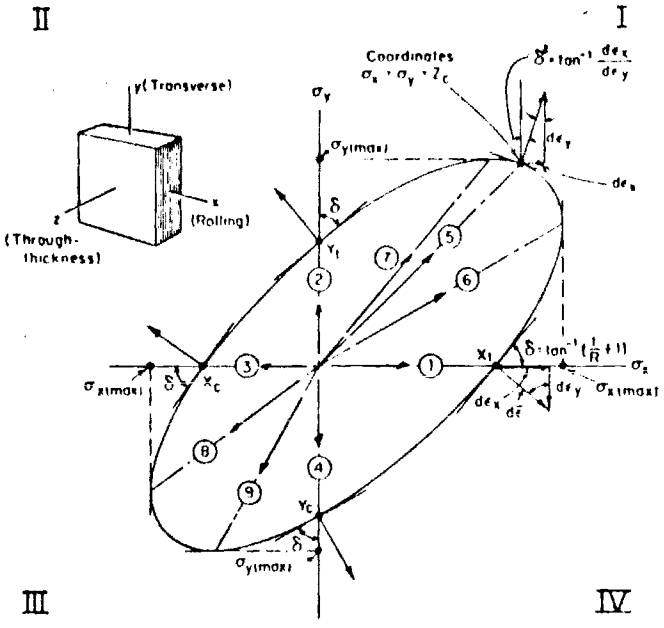

–Yield locus for plane-stress loading, representing a general case of plastic anisotropy (schematic). Loading paths 1 through 9, stress levels, and angles are discussed in the text

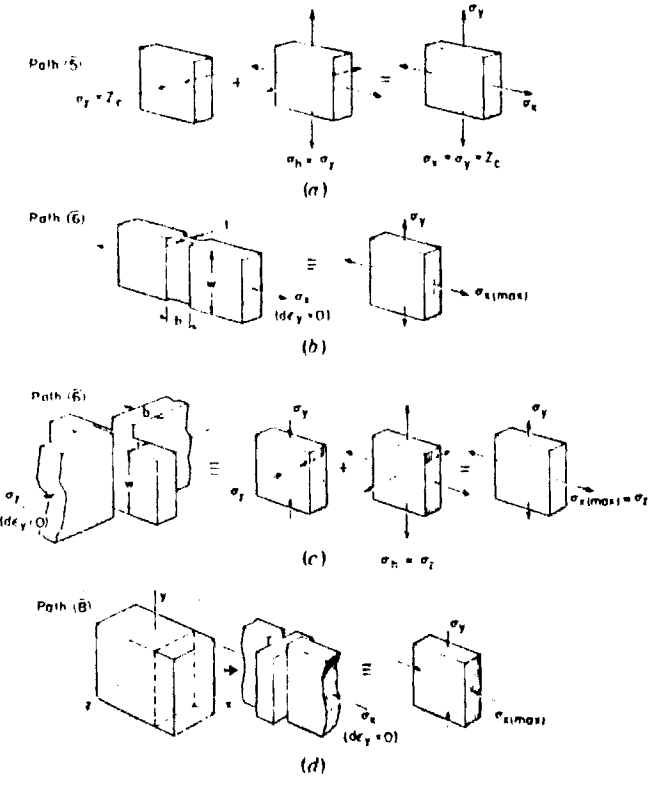

–Schematic representations of stress states on loading paths in Fig. 1: (*a*) path 5; (*b*) path 6, also applicable to path 7 if specimen is oriented for pulling along the *y* direction; (*c*) path 6 showing equivalence between plane-strain tension and compression; (*d*) path 8, also applicable to path 9 if specimen is oriented for compression along *y* direction.

SLIDE 17

The as-received alloy had been beta processed and had a random texture. The yield locus can be described by the Van Mises (or the Tresta) criterion.

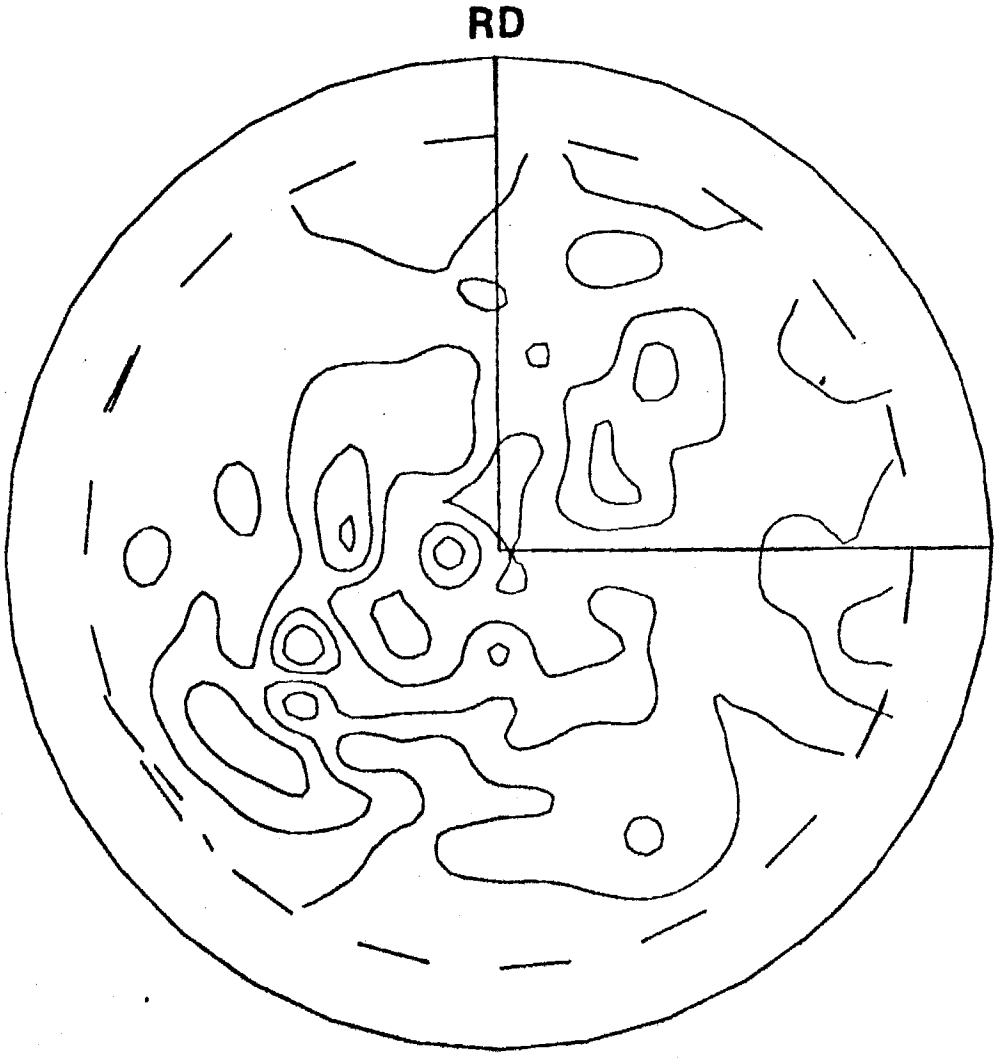

Ti-6211 A.R.

(0002) POLE FIGURE

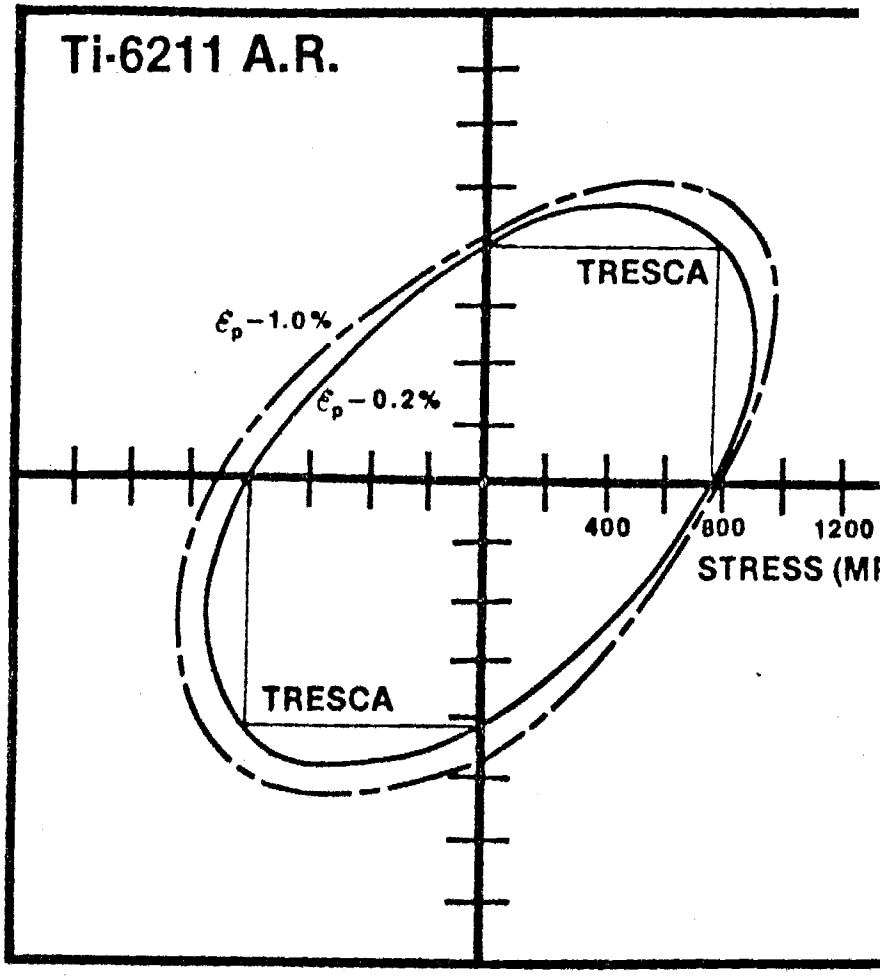

YIELD LOCUS DIAGRAM

SLIDE 18

This shows the microstructure developed by HT, the as-received alloy at 1050°C for 30 minutes, water quenching and cross rolling 75% reduction in thickness at 850°C. This was followed by heat treating at 850°C for 2 hours, water quenching and aging at 500°C. (a) shows the equiaxed microstructure and the TEM of (b) shows this at a higher magnification. (b) was representative of approximately 80% of the structure and (c) of approximately 20%. Further work needs to be done to establish the TMT for obtaining a homogeneous microstructure similar to (b).

SLIDE 18

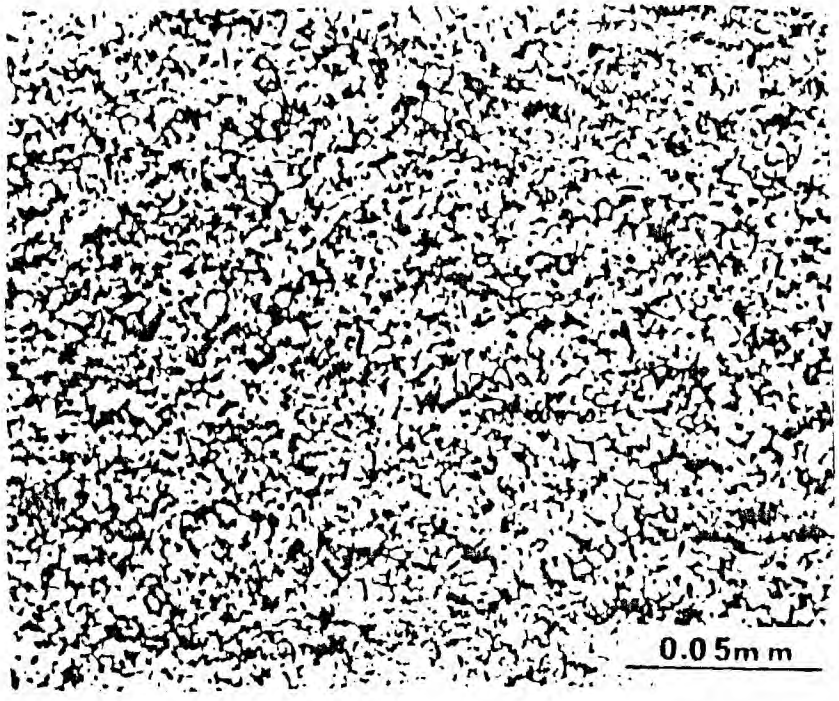

Ti-6Al-2Nb-1Ta-0.8Mo

HT 1050 °C 30 min. WQ
CR 850 °C
HT 850 °C 2h WQ
Age 500 °C 1h

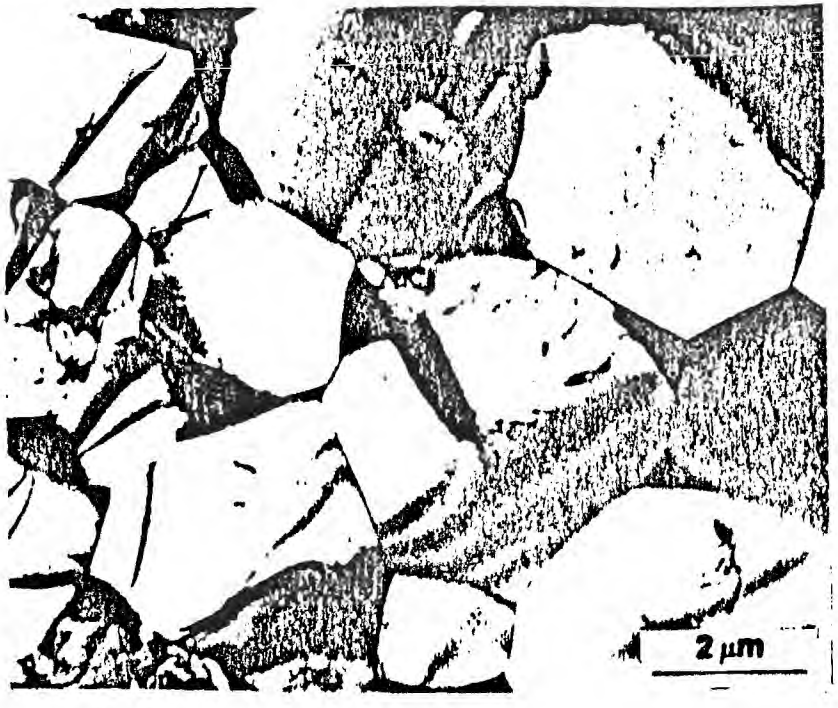

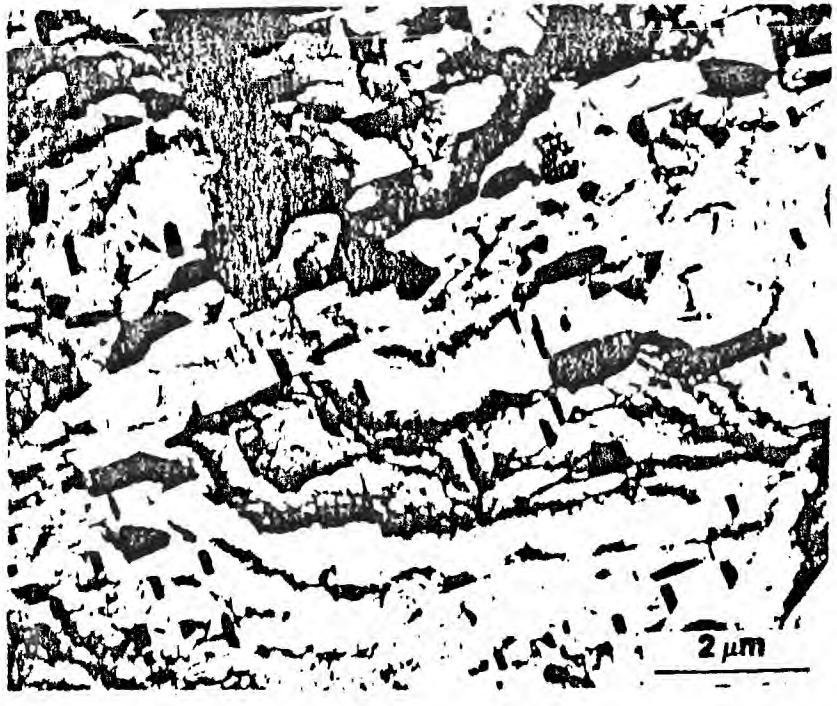

SLIDE 19

This slide shows that the equiaxed microstructure can be strengthened, with no significant loss in ductility, by aging at 500°C.

SLIDE 19

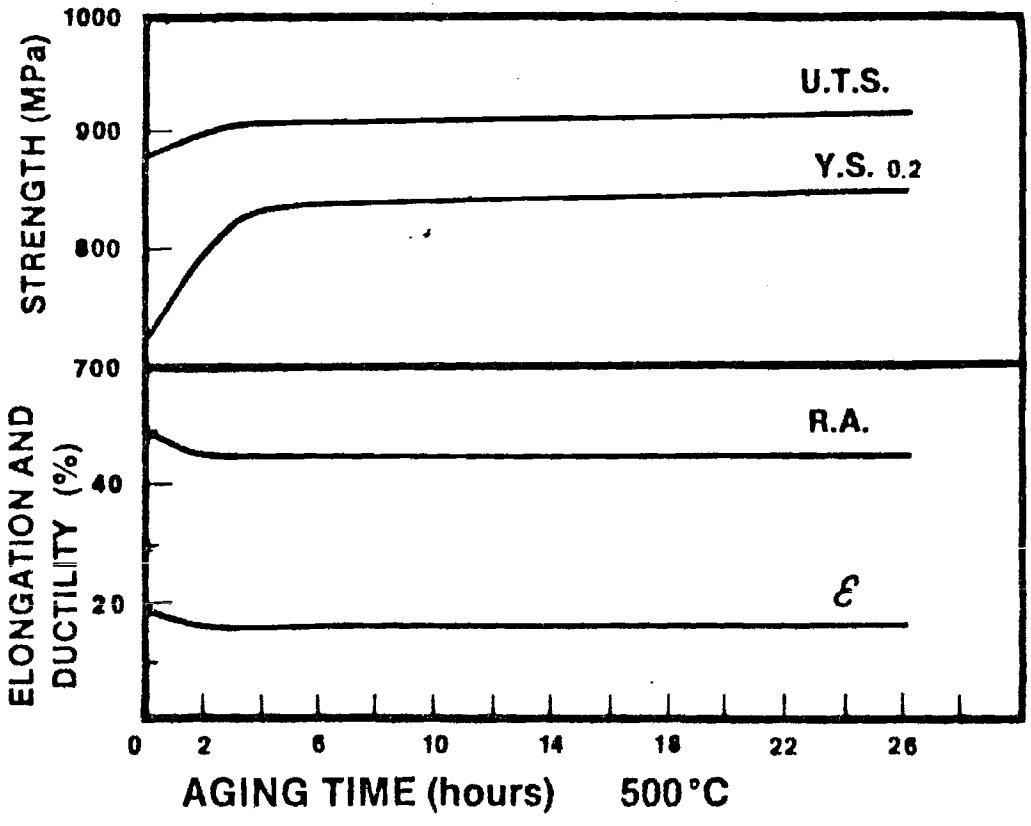

Ti-6211 HT 1050 °C 40 min. WQ R 850 °C HT 850 °C 1h WQ

SLIDE 20

This shows that the TMT produced a near-basal texture and significant texture strengthening in guadrant I However, quadrant III could be described by the Treasa or Van Mises criterion.

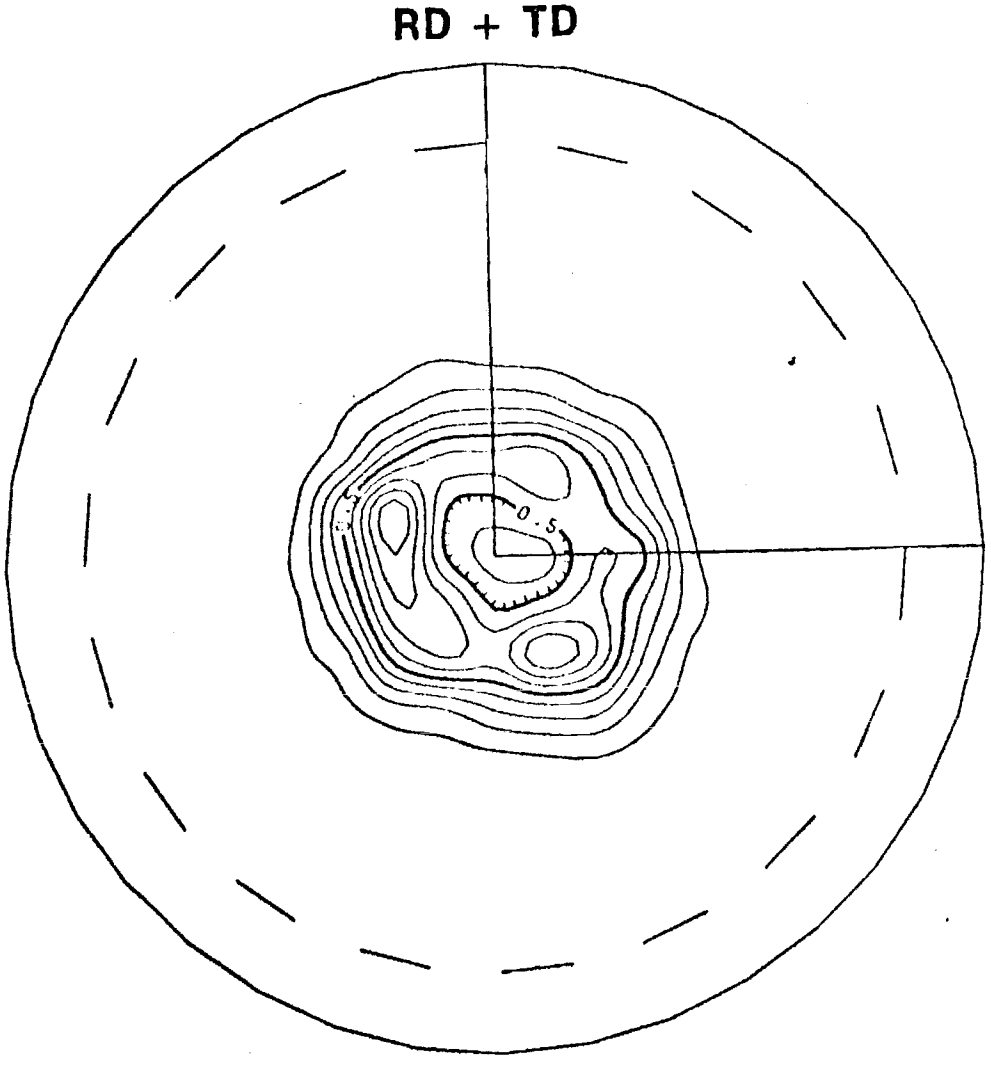

CR Ti-6211

(0002) POLE FIGURE

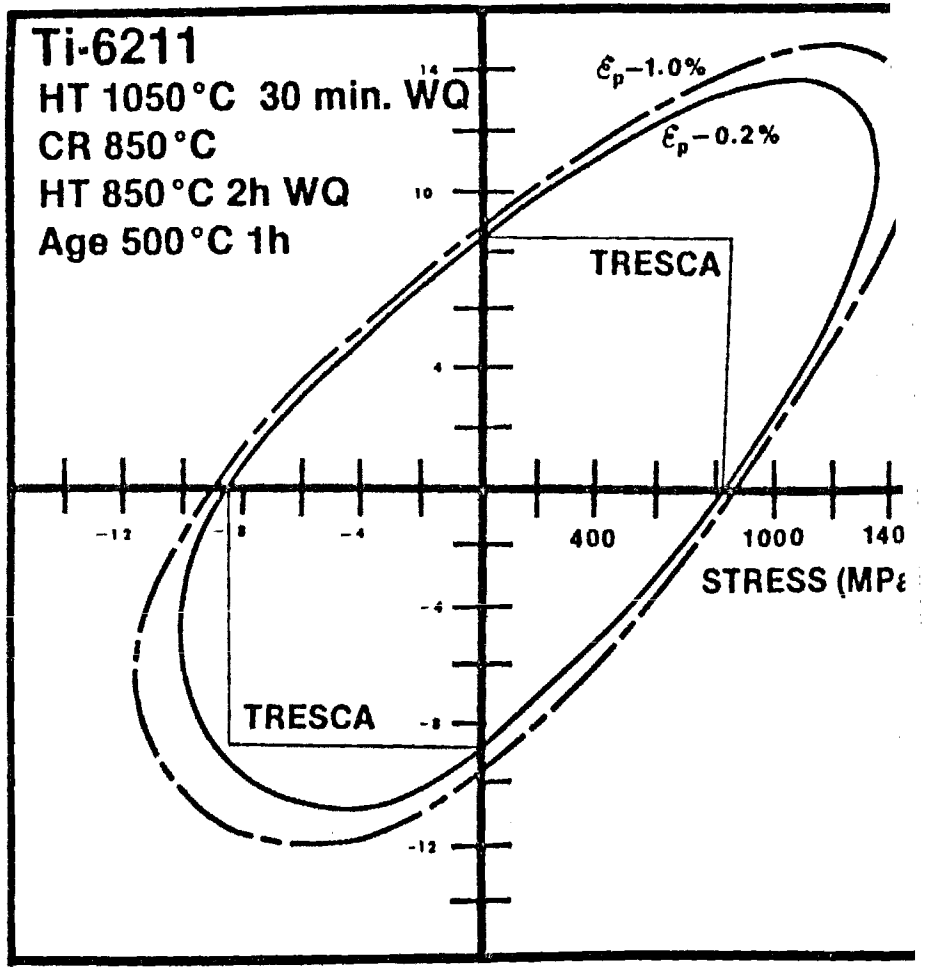

YIELD LOCUS DIAGRAM

SLIDE 21

This shows that the deformation mode of path 8 (in quadrant III) was primarily twinning. The microtwins of (c) are on $(10\bar{1}2)$. Large twins (a) and (b) were also observed. These twins were not observed in path 6 of quadrant I.

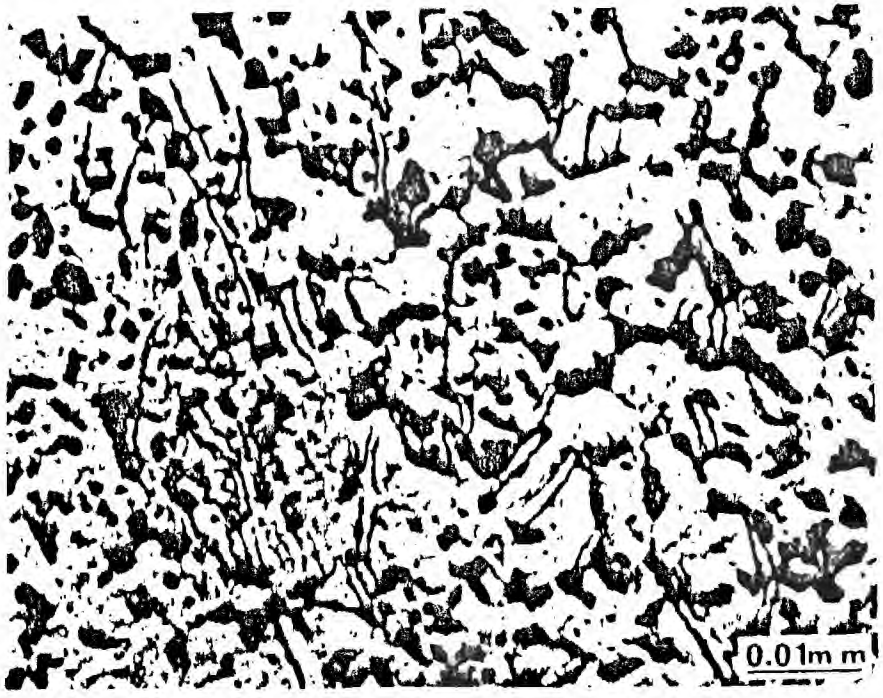

Ti-6Al-2Nb-1Ta-0.8Mo

DEFORMATION STRUCTURE PATH 8

HT 1050 °C 30 min. WQ
CR 850 °C
HT 850 °C 2h WQ
Age 500 °C 1h

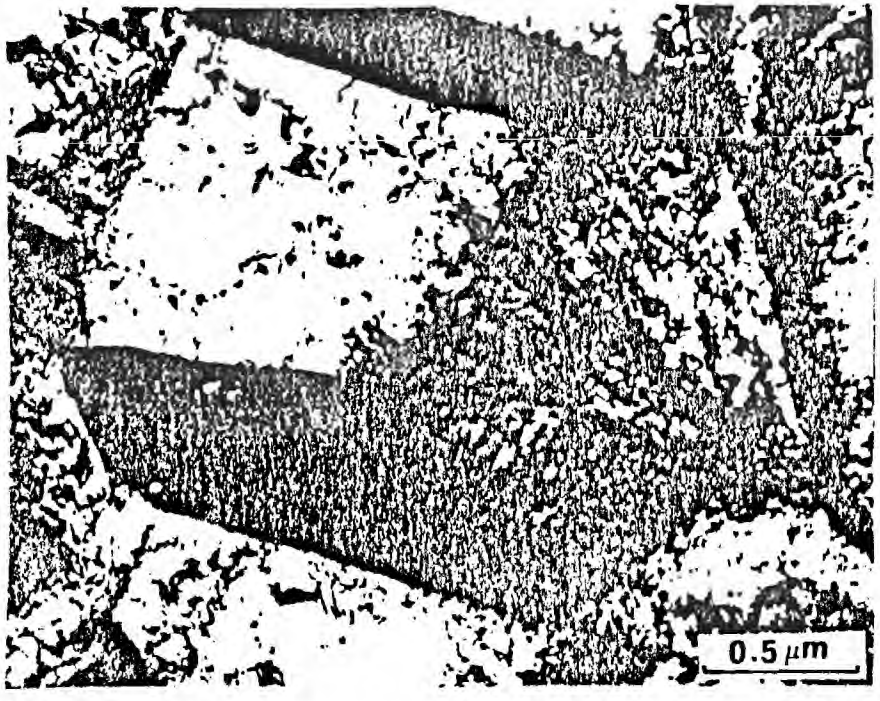

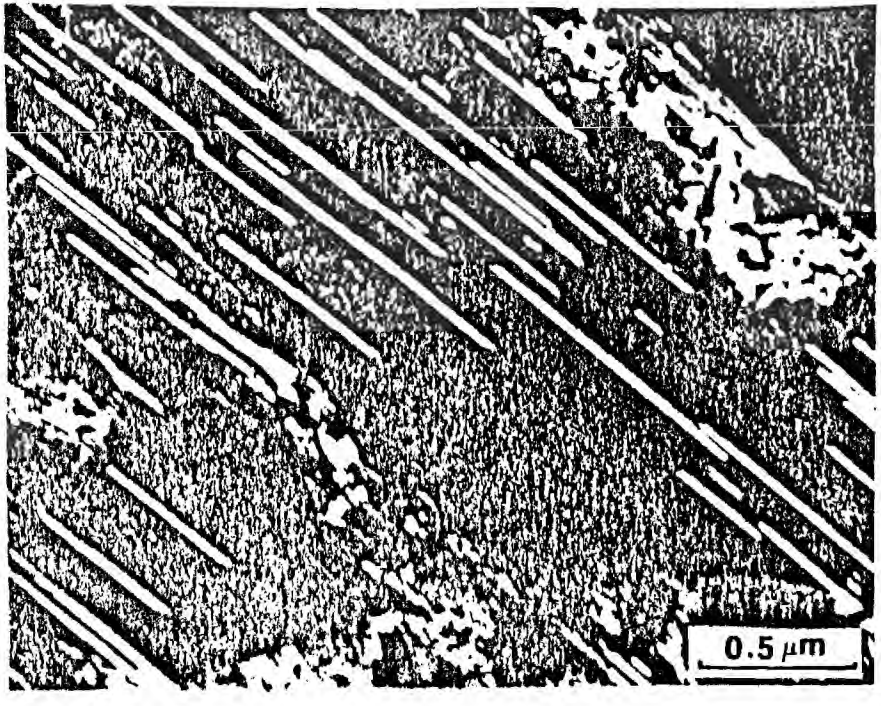

DEFORMATION BEHAVIOR OF Ti 6211

Heat Treatment	Loading Path	Observed Deformation Mode
800°C (40') WQ ± 500°C (2)	1	Basal Slip (0002)
950°C (40') WQ ± 500°C (2)	1	Basal Slip (0002)
HR + 850°C (1) WQ + 500°C (100)	1	Prism Slip {10T0}
HR + 850°C (1) WQ + 500°C (3)	5	Pyramidal Slip {10T1}
	6	Pyramidal Slip {10T1}
	8	{10T2} Twin and Microtwin Basal Slip (0001) Pyramidal Slip {10T2}

NOTE: Primarily a-type screw dislocations have been observed on the slip planes.

$\bar{b} = 1/3 \langle 11\bar{2}0 \rangle$

SLIDE 23

This shows the microstructure and fracture behavior of the TMT material. The equiaxed microstructures increased the ductility over a comparably strengthened Widemanstatten structure.

Ti-6Al-2Nb-1Ta-0.8Mo

HT 1050 °C 30 min. WQ
CR 850 °C
HT 850 °C 2h WQ
Age 500 °C 3h

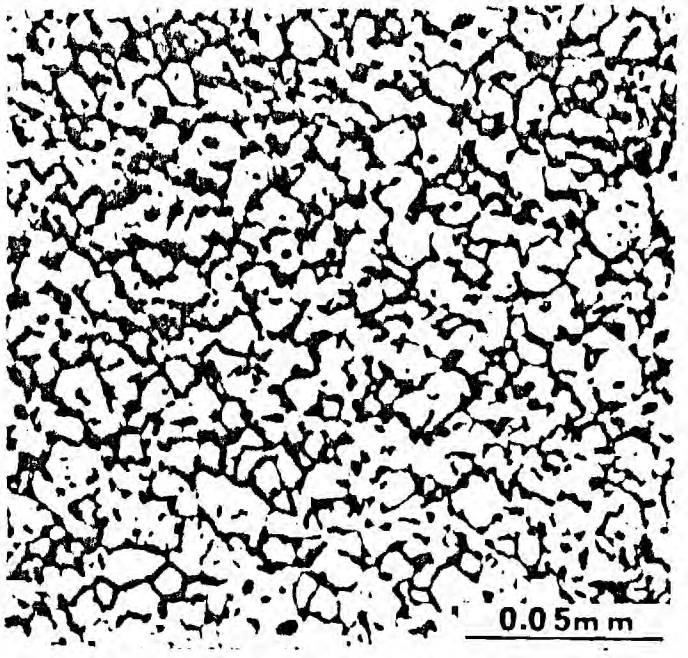

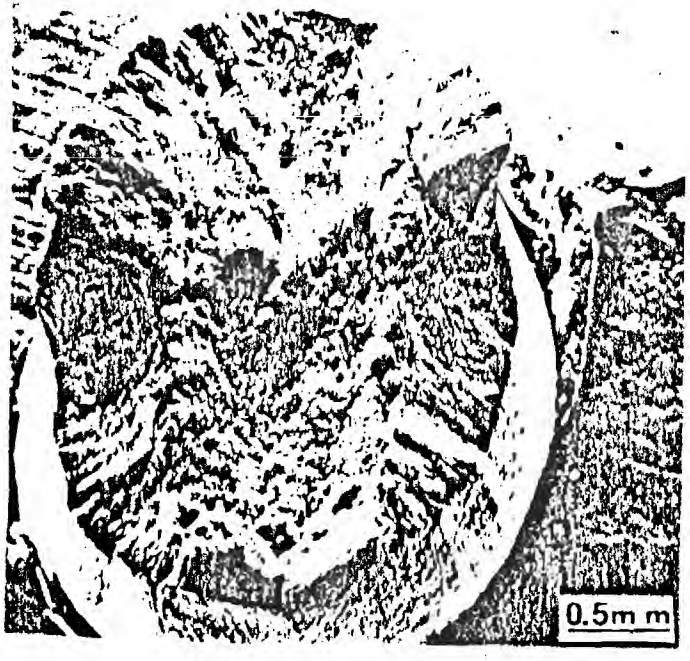

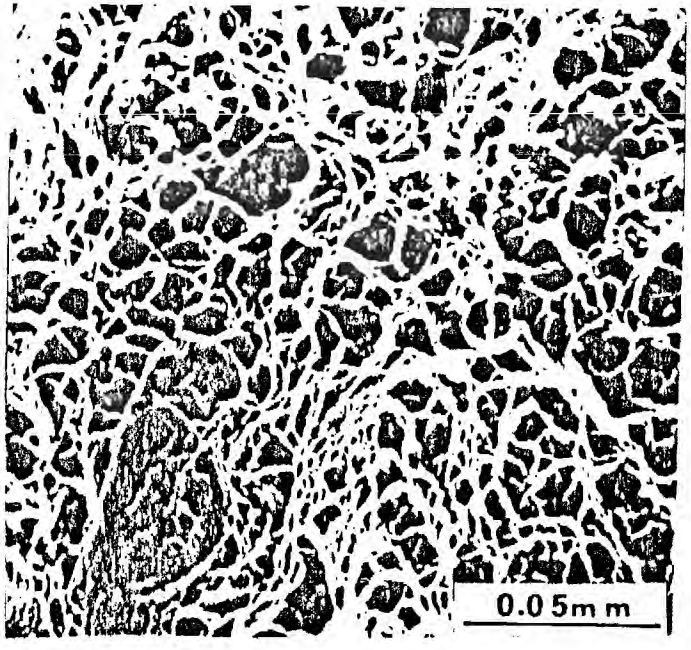

SUMMARY OF RESULTS ON EQUIAXED ALPHA AND BETA

1. Cross rolling of Ti-6211 in the $\alpha+\beta$ field produces an equiaxed microstructure with a basal-type texture.

2. The microstructure can be strengthened by ~125 MPa by precipitation of Ti_3Al.

3. Ductility of the equlaxed structure is higher than the Widmanstatten $\alpha+\beta$ structure at comparable strength levels.

4. The texture hardening effect was approximately 60% in the tension-tension quadrant. In the compression-compression quadrant deformation twinning prevented the locus from expanding much beyond the position predicted by isotropic material.

FUTURE WORK

1. Determine the best processing conditions for producing a homogeneous equiaxed structure.

2. Vary the texture, i.e., produce basal/transverse and transverse textures and measure texture strengthening effect.

3. Examine the effect of microstructure and texture on fracture toughness.

4. Examine the effect of cyclic loading on the yield locus of textured material.

5. Examine the effect of microstructure and properties on FCI and FCP.

6. Optimize the Widmanstatten structure by HT and TMT in the β field:
   (a) reduce prior β GS
   (b) reduce Widmanstatten colony size
   (c) control dimensions of $\alpha+\beta$ phases

End of the Year Report
ONR Task Order No. N00014-79-C-0207
September 30, 1981

A. Investigation of the Effect of Microstructure on the Deformation Modes and Mechanical Properties of Ti-6Al-2Cb-1Ta-0.8Mo

The objective of this research is to quantify the microstructure, determine the deformation modes and behavior of Ti-6211 and establish clear-cut functional relationships between these important interrelated factors. This will be accomplished on a variety of different microstructures which can be produced in Ti-6211. Alpha plus beta titanium alloys such as Ti-6211 can be processed to contain microstructures having equiaxed platelet or grain boundary alpha in retained beta matrix; both phases can be fine, medium or coarse and continuous or noncontinuous. The variations result from suitable adjustments to the working and annealing temperature with respect to the beta transus temperature. The primary processing parameters not only affect the microstructure, but also the crystallographic texture and for Ti alloys a strong preferred orientation can result in directional properties.

Metallurgical Investigation of Hot Ductility Loss in Ti-6211: The objective of this research is to understand the microstructural features which lead to the hot ductility dip observed in certain heat-treated conditions in this alloy. Metallurgical factors to be studied include the effects of beta grain size and shape, alpha phase morphology, and deformation behavior on elevated temperature ductility and fracture. Tests are being conducted on specimens produced both by the "Gleeble" apparatus and laboratory heat treatments designed to generate variations in beta grain size and shape and alpha phase morphologies.

Gleeble specimens which show extremely low ductility in the range 750-850C fail by a mixture of intergranular fracture and transgranular shear, both of which show ductile features. This result indicates that failure has occurred due to a grain boundary alpha phase morphology which localizes deformation and leads to strain concentration with subsequent low ductility. However, a grain boundary alpha phase morphology does not necessarily guarantee low ductility. Specimens air cooled from above the beta transus to produce Widmanstatten alpha plus beta with grain boundary alpha exhibit intergranular fracture with ductile features, but also have good ductility due to the structure within the grains. The difference in flow stress between the grain interior and the grain boundary alpha is not as great as in the case of the Gleeble specimens which

contain intragranular martensite with intergranular alpha, and thus the strain concentration is less. Specimens quenched from above the beta transus to form martensite exhibit good ductility within the temperature range of the ductility minimum. These specimens show no evidence of grain boundary alpha, either as a result of heat treatment or of testing at elevated temperature, and thus there is no possibility of strain localization in the grain boundary regions.

Future work will involve further testing of Gleeble specimens and laboratory specimens heat treated to produce intragranular martensite and grain boundary alpha. The influence of phase morphology on deformation and strain localization will be examined and correlated with the observed hot ductility dip.

Low Cycle Fatigue Studies on Ti-6211: The low cycle fatigue properties of as-received Ti-6211, with a microstructure of Widmanstatten alpha plus beta, and a heat treated (H1) Ti-6211, with a Widmanstatten alpha plus beta plus martensite microstructure, are being studied. The sequence of heat treatment for H1 is as follows: anneal 970C for 40 minutes, WQ age 500C for 2 hours, AC. The 40 volume percent beta present at 970C transforms to continuous martensite during quenching and increases the strength when compared to the as-received alloy. Moreover, the microstructure is further strengthened by aging to precipitate Ti_3Al. The martensite acts as a major barrier to slip and the slip distance of H1 Ti-6211 is shorter than that of the as-received Ti-6211. A 23% higher yield strength with no loss in ductility is obtained by the treatment.

Cyclic hardening occurs for both materials in the first few cycles followed by softening for high strain amplitude tests. Cyclic softening occurs from the very first cycle at lower strain amplitudes. Cyclic hardening in the early stages initially results from increased dislocation-dislocation interactions and an increased dislocation density. The cyclic softening might result from either microstructure modification or microcrack formation. However, surface observations after a few cycles suggest that the cyclic softening is associated with the formation of microcracks at both slip bands and at alpha/beta interfaces.

Cracks initiate in alpha phase slip bands in the as-received material and at alpha/beta interfaces in the H1 alloy. Microcrack link-up seems to be more difficult when crack nucleation is confined to the alpha phase. This results in a better fatigue performance, as indicated by strain-life plots, for the Widmanstatten alpha plus beta alloy.

B. Implication of ONR Contract Research in Terms of Applied Significance:

The knowledge obtained from accomplishing the objectives of this program are essential to the understanding of the mechanical properties and performance

capabilities of Ti-6211. The results should aid in determining ways to control desired properties through primary processing manipulations.

C. Publications, Reports and Talks

An oral presentation of this research was given at the Ti-6211 Review Meeting, U. S. Naval Research Laboratory, Annapolis, Maryland, March 18, 1981. A technical report with restricted distribution was issued in July, 1981, and a subsequent presentation was given September 28, 1981 at U. S. Naval Research Laboratory, Annapolis, Maryland.

D. Other Research Tasks

1. The Effect of Microstructures on the Properties of High Strength Aluminum, AFOSR-78-3471, $140,000 for a one year program.

2. The Effect of Ion Plating and Ion Implantation on the Cyclic Response and Fatigue Crack Initiation of Metals and Alloys, ONR Task Order No. N00014-78-C-0270, $179,371 for a three year program.

3. The Effects of Powder Metallurgical Processing and Intermediate Thermal Mechanical Treatment on the Fatigue Properties of High Strength Aluminum Alloys, USARO Contract No. DAAG 29-80-C-0100, $119,391 for a three year period.

4. Development of High Stiffness Aluminum Alloy from Rapidly Solidified Powders for Aerospace Structural Applications, Lockheed Missile & Space Co. Contract No. HJ80C2630R, $191,000 for a two year period.

Respectfully submitted,

Edgar A. Starke, Jr.
Principal Investigator

E-19-618

UNCLASSIFIED

SECURITY CLASSIFICATION OF THIS PAGE *(When Data Entered)*

REPORT DOCUMENTATION PAGE		READ INSTRUCTIONS BEFORE COMPLETING FORM
1. REPORT NUMBER	2. GOVT ACCESSION NO.	3. RECIPIENT'S CATALOG NUMBER
4. TITLE *(and Subtitle)* THE EFFECT OF MICROSTRUCTURE AND TEXTURE ON THE MECHANICAL PROPERTIES OF AN ALPHA-BETA TITANIUM ALLOY		5. TYPE OF REPORT & PERIOD COVERED Technical July 81 - Jan 82 6. PERFORMING ORG. REPORT NUMBER E-19- 678-82-1
7. AUTHOR(s) S. Shih, F. S. Lin, S. Spooner and E. A. Starke, Jr		8. CONTRACT OR GRANT NUMBER(s) N00014-79-C-0207
9. PERFORMING ORGANIZATION NAME AND ADDRESS Fracture & Fatigue Research Laboratory Georgia Institute of Technology Atlanta, Georgia 30332		10. PROGRAM ELEMENT, PROJECT, TASK AREA & WORK UNIT NUMBERS
11. CONTROLLING OFFICE NAME AND ADDRESS Office of Naval Research Director-Metallurgy Programs, Material Science Div. 800 N. Quincy St., Arlington, VA 22217		12. REPORT DATE April 1982 13. NUMBER OF PAGES 16
14. MONITORING AGENCY NAME & ADDRESS *(if different from Controlling Office)*		15. SECURITY CLASS. *(of this report)* UNCLASSIFIED 15a. DECLASSIFICATION/DOWNGRADING SCHEDULE

16. DISTRIBUTION STATEMENT *(of this Report)*

UNLIMITED

17. DISTRIBUTION STATEMENT *(of the abstract entered in Block 20, if different from Report)*

18. SUPPLEMENTARY NOTES

Presented at American Society for Metals Conference "Texture-Microstructure-Mechanical Properties Relationships of Materials, November 1981, West Palm Beach, FL

19. KEY WORDS *(Continue on reverse side if necessary and identify by block number)*

alpha-beta Ti alloy, microstructure of Ti, texture of Ti, mechanial properties of Ti, Ti-6211

20. ABSTRACT *(Continue on reverse side if necessary and identify by block number)*

The microstructure of alpha + beta titanium alloys, such as Ti-6Al-2Nb-1Ta-0.8Mo (Ti-6211) and Ti-6Al-4V (Ti-6-4), can be significantly varied by modifications in primary processing procedures and mechanical properties are sensitive to such microstructural variations. By suitable selection of the working and annealing temperatures, microstructures can be developed having equiaxed, platelet, or grain boundary alpha in a retained beta or martensite matrix; the phases can be fine, medium, or coarse, and continous or discontinuous. In addition to property variations associated with microstructural modifications,

DD FORM 1 JAN 73 1473 EDITION OF 1 NOV 65 IS OBSOLETE

UNCLASSIFIED

SECURITY CLASSIFICATION OF THIS PAGE *(When Data Entered)*

THE EFFECT OF MICROSTRUCTURE AND TEXTURE ON THE MECHANICAL PROPERTIES OF AN ALPHA-BETA TITANIUM ALLOY

S. Shih, F. S. Lin, S. Spooner and E. A. Starke, Jr.
Fracture and Fatigue Research Laboratory
Georgia Institute of Technology
Atlanta, Georgia 30332

INTRODUCTION

The microstructure of alpha + beta titanium alloys, such as Ti-6Al-2Nb-1Ta-0.8Mo (Ti-6211) and Ti-6Al-4V (Ti-6-4), can be significantly varied by modifications in primary processing procedures and mechanical properties are sensitive to such microstructural variations (1,2). By suitable selection of the working and annealing temperatures, microstructures can be developed having equiaxed, platelet, or grain boundary alpha in a retained beta or martensite matrix; the phases can be fine, medium, or coarse, and continuous or discontinuous (3,4). In addition to property variations associated with microstructural modifications, mechanical properties develop substantial directionality as a result of texture changes. The crystallographic texture of Ti-6211 can be greatly varied by an appropriate intermediate thermomechanical treatment (ITMT) below the beta-transus temperature. Basal texture with the basal planes parallel to the rolling plane can be obtained by cross-rolling at a low temperature in the alpha + beta phase field (5). Transverse texture with the basal planes perpendicular to the rolling plane and parallel to the rolling direction can be obtained by unidirectional-rolling at a higher temperature in the alpha + beta phase field (6-8).

Since texture and microstructure can be obtained nearly independently, their individual effects may be used in a beneficial manner. This study examines the interrelationships between processing, texture, microstructural modifications and mechanical properties of Ti-6211.

EXPERIMENTAL PROCEDURES

The Ti-6Al-2Nb-1Ta-0.8Mo alloy was supplied in plate form. The chemical composition is given in Table 1 (in weight percent). The as-received (AR) material had been beta-processed and air cooled.

Table 1. Chemical Composition of Ti-6211

Al	Nb	Ta	Mo	O	N	H	C	Y	Mn	Si	Ti
5.6	2.16	0.95	0.79	0.066	0.007	0.0046	0.02	<0.002	<0.01	<0.01	Balance

Widmanstätten and equiaxed alpha microstructures were chosen along with the random, basal and transverse textures for this study. The Widmanstätten alpha + beta structure typical of beta-processed and air-cooled alpha + beta titanium alloys is designated as the AR microstructure. The beta-transus temperature of Ti-6211 is 1283K (1). In order to obtain a martensitic Widmanstätten structure, the AR Ti-6211 was annealed at 1243K for 0.7 hours in an argon atmosphere, water quenched, aged at 773K for 2 hours, and air cooled. The equilibrium volume fraction of the beta phase increased during annealing at 1243K, and subsequently transformed to martensite during water quenching (1). In addition, Ti_3Al may precipitate in the alpha phase during aging at 773K (9). This treatment is designated as H1. In order to develop an equiaxed alpha structure and the desired textures, the AR Ti-6211 was solutionized at 1323K for 0.7 hours, water quenched, then cross-rolled at 1123K to obtain the basal texture; or unidirectional-rolled at 1233K to obtain the transverse texture. A complete recrystallization treatment was conducted after the ITMT processing. During this treatment, the deformed materials were annealed at 1213K for 1 hour (to develop the desired equiaxed alpha grain size and prior beta thickness at grain boundary triple junctions), water quenched, and aged at 773K for 2 hours and air cooled.

Metallography samples were taken from the longitudinal-short transverse plane, polished, etched in Kroll's reagent, and examined through the entire thickness of the plate. The pole figures of (0002), $(10\bar{1}0)$, $(10\bar{1}1)$ and $(11\bar{2}0)$ reflections were measured using a Siemens goniometer with filtered CuKα

radiation. Using the Schultz reflection method, measurements were made on the AR plates and the equiaxed materials. Data collected over a polar orientation range from 0 to 70 degrees were converted to pole figures. In some cases, a pole figure technique (10) which averages texture through the plate thickness was applied to obtain a pole figure completely within one quadrant from 0 to 90 degrees. A complete pole figure can be generated by mirror reflecting the texture information about the transverse and rolling direction lines.

Round tensile and low-cycle fatigue (LCF) samples were machined according to ASTM Standards E8-69 (11). The tensile specimens were 4 mm in gage diameter and 16 mm in gage length and the LCF samples were 4 mm in gage diameter and 10 mm in gage length. All of the samples were mechanically polished through 1 μm diamond paste prior to testing. Both tests were performed on an electrohydraulic closed-loop MTS testing machine equipped with an 8 mm clip-on extensometer. The tensile tests were conducted under stroke control at a strain rate of 10^{-3}/sec, and tension-compression LCF tests were conducted under total strain control at a strain rate of 0.33%/sec. The strain-life curves were constructed by plotting the plastic strain amplitude, $\Delta\varepsilon_p/2$, versus the reversals to failure, $2N_f$ according to the form (12): $\Delta\varepsilon_p/2 = \varepsilon_f'(2N_f)^c$, where ε_f' is the fatigue-ductility coefficient, and c is the fatigue-ductility exponent. All mechanical tests were performed at room temperature and in laboratory air (about 298K and 45% relative humidity).

Some tensile samples were pulled 3 to 5% for deformation characterization studies. A limited number of LCF specimens were electropolished using the method suggested by Blackburn and Williams (13), and lightly etched in Kroll's reagent before being tested to 30% of total life. They were then examined over the entire gage surface using a scanning electron microscope (SEM) in order to determine the fatigue crack nucleation sites. Thin foils for TEM examination were prepared with a Tenupol apparatus using a solution of 6% perchloric acid, 35% n-butyl alcohol, and 59% methanol at 15 volts and 248K.

The anisotropic properties of the alloy were evaluated from the yield loci diagram (14), which was determined using tension, compression, and plane-strain compression tests. The plane-strain compression samples were made so that the ratio of indentor thickness to sample thickness was 2:1 and the sample width was 10 times that of the sample thickness. Teflon films were used for lubrication. Some specimens were

electropolished before testing in order to observe variations in deformation with respect to loading paths. Duplicate samples were tested using a strain rate of 0.33%/sec in all cases.

RESULTS AND DISCUSSION

Microstructure

Fig. 1(a) shows the Widmanstätten alpha + beta microstructure of the AR Ti-6211. The TEM micrograph of Fig. 1(b) illustrates that the beta plates (dark areas) are discontinuous. During air cooling the volume fraction of beta decreases, and dislocation networks may be left behind. When the AR Ti-6211 is annealed at 1243K, the volume fraction of the beta phase increases, and transforms to martensite during water quenching, as shown in Fig. 1(c). It is obvious that the martensitic plates are thicker than the beta plates of the AR material (both in dark). The equiaxed alpha microstructures, produced by the ITMT processing and recrystallization treatment, are presented in Figs. 1(d) and 1(e). The dark areas, which are Widmanstätten alpha + martensite (as shown in Fig. 1(e)), are continuous around the alpha grains. The 4 μm alpha grains represent about 90 volume percent of the total and the Widmanstätten alpha + martensite regions are about 0.62 μm thick. Ti_3Al was not detected after aging at 773K for 2 hours for both types of microstructures, although Williams (9) has suggested that Ti_3Al can precipitate in the alpha phase and account for the increase in strength associated with aging.

Texture

The pole figures show that the preferred orientation at the center of the AR plate is different from that at the surface. Figs. 2(a) and 2(b) are the $(10\bar{1}1)$ pole figures of the plate surface and plate center, respectively. The surface texture is nearly random and is characteristic of that produced by beta processing. The texture averaged through the thickness exhibits a weak transverse texture $(11\bar{2}0)[10\bar{1}0]$, and may have resulted from the finishing operation being conducted slightly below the beta-transus temperature. Nevertheless, the preferred crystallographic texture is unchanged during the H1 thermal treatment. The (0002) and $(10\bar{1}1)$ pole figures of both the 1123K cross-rolled and the 1223K unidirectional-

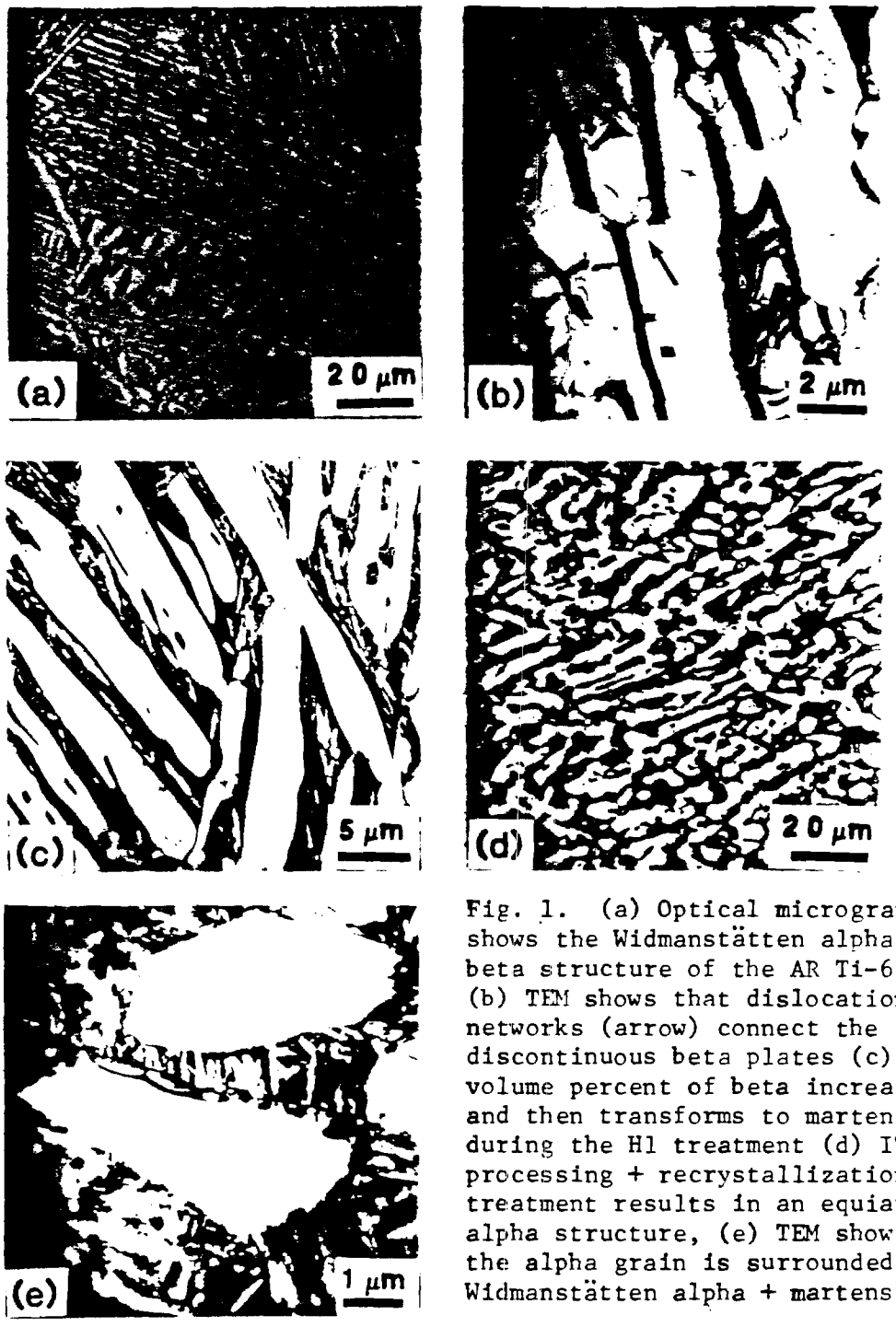

Fig. 1. (a) Optical micrograph shows the Widmanstätten alpha + beta structure of the AR Ti-6211 (b) TEM shows that dislocation networks (arrow) connect the discontinuous beta plates (c) volume percent of beta increases, and then transforms to martensite during the H1 treatment (d) ITMT processing + recrystallization treatment results in an equiaxed alpha structure, (e) TEM shows the alpha grain is surrounded by Widmanstätten alpha + martensite.

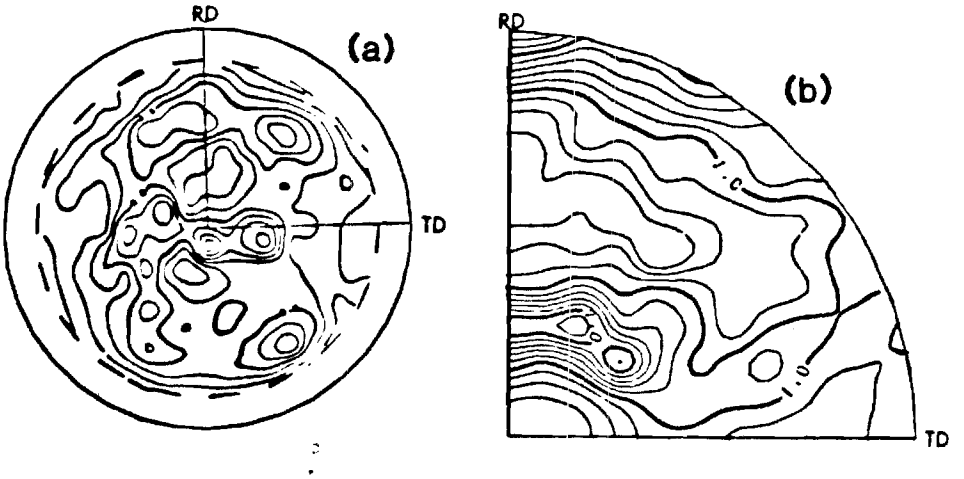

Fig. 2. (a) $(10\bar{1}1)$ pole figure displays the nearly random texture of the AR Ti-6211 at plate surface, (b) at plate center, a weak transverse texture $(11\bar{2}0)[10\bar{1}0]$.

rolled Ti-6211 are given in Fig. 3. The rolling direction was parallel to $[10\bar{1}0]$. These results confirm that the appropriate ITMT processing and recrystallization treatment develops the desired basal and transverse textures.

Monotonic Properties

The monotonic properties of Ti-6211 for the different conditions are tabulated in Table 2. The tensile properties of the AR Ti-6211 are the same in the RD and TD and the H1 treated material was only tested in the TD since both materials possess a random texture. The basal texture of the CR Ti-6211 also suggests isotropic tensile properties and measurements are only reported for the TD. However, the monotonic properties of the UR Ti-6211, which has a transverse texture, are anisotropic and results of tensile tests in both the RD and TD are given. The yield strength of the H1 Ti-6211 is approximately 22% greater than that of the AR Ti-6211 without significant loss in ductility. During deformation of the AR materials, the colony boundaries acted as major slip barriers, Fig. 4, and the slip length was determined by the colony size. However, the transformed beta acted as major slip barriers in the H1 material, Fig. 5, decreasing the slip length from the colony size, $\sim$ 45 μm, to the acicular alpha size, $\sim$ 1.2 μm. The 163

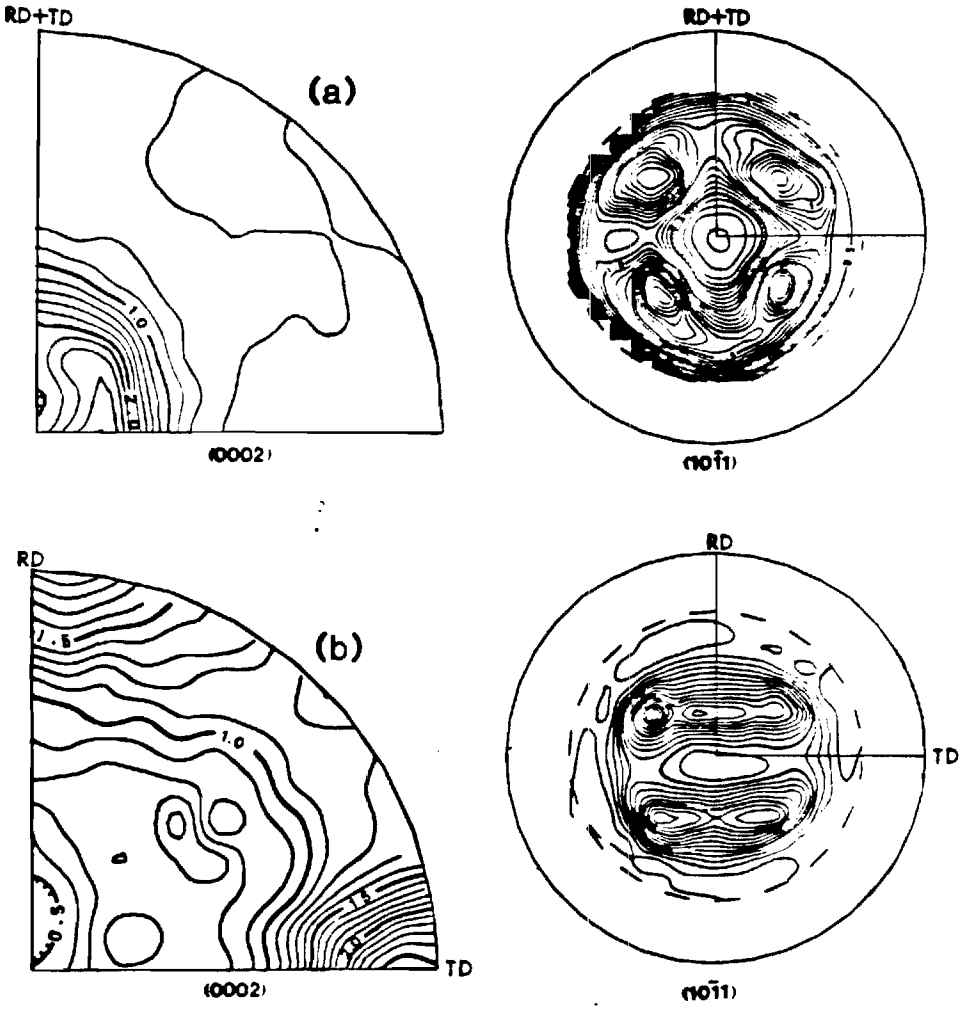

Fig. 3. (a) (0002) and (10$\bar{1}$1) pole figures of the CR Ti-6211 show the basal texture, (b) (0002) and (10$\bar{1}$1) pole figures of the UR Ti-6211 show the transverse texture.

MPa increase in yield strength associated with the decrease in the deformation barrier spacing can be ascribed to the Hall-Petch mechanism, represented by $\sigma_{ys} = \sigma_o + Kd^{-\frac{1}{2}}$, where σ_o is the frictional stress, d is the deformation barrier spacing and K is a constant. Assuming that σ_o and K are constant (15) for both conditions, the calculated change in σ_{ys}, 164 MPa, is essentially the same as the measured value.

The strength-ductility combinations of the equiaxed, CR, and UR materials are superior to those of the Widmanstätten

Table 2. Monotonic Properties of Ti-6211

Alloy Condition	Stress Axis (SA)	0.2% Yield Strength MPa	Ultimate Tensile Strength MPa	Elongation %	Reduction in Area %
AR	RD *	760	855	15.4	30.0
	TD *	799	874	14.1	28.1
H1	TD	937	1012	12.3	31.9
CR #	TD	1010	1093	16.3	55.7
UR #	RD	998	1082	15.4	54.0
	TD	1018	1106	15.6	55.3

* RD = The SA is parallel to the rolling direction.
TD = The SA is parallel to the transverse direction.
\# CR = The deformed Ti-6211 with the equiaxed alpha structure and the basal texture.
UR = The deformed Ti-6211 with the equiaxed alpha structure and the transverse texture.

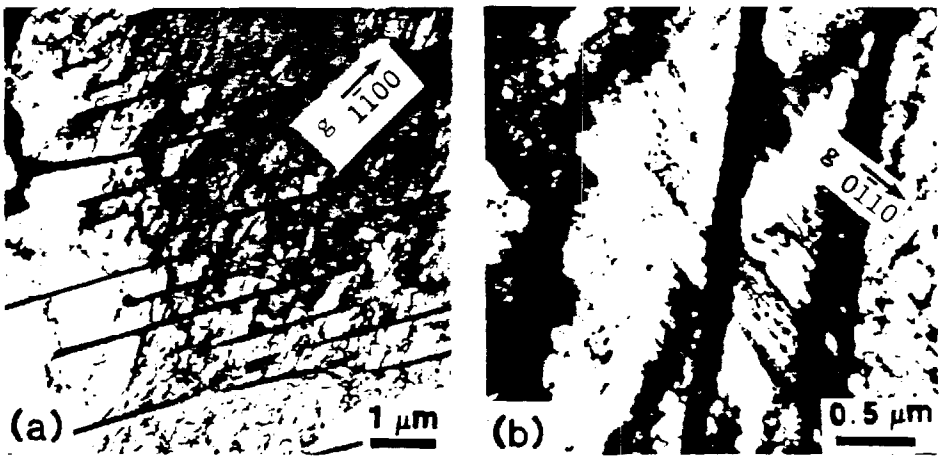

Fig. 4. Colony boundary is the major slip barrier during deformation of the AR Ti-6211, (a) foil plane is (0002), (b) foil plane is (10$\bar{1}$2).

structures. Yield strengths as high as 1018 MPa are obtained without loss in ductility by treatments which produced an alpha phase completely surrounded by a strong deformation barrier (alpha + martensite). The high ductility is associated with the absence of stain localization (1).

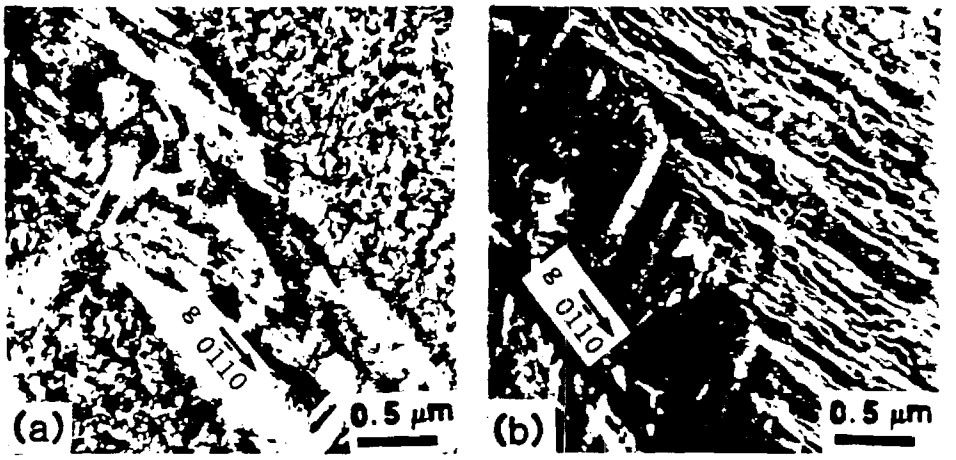

Fig. 5. Transformed beta is the major slip barrier during deformation of the H1 treated Ti-6211, foil plane is $(10\bar{1}2)$ for (a) and (b).

Yield Loci

The yield loci diagrams for the Ti-6211 alloy in the AR condition and for the equiaxed alpha structures with the basal and transverse textures were determined. The path description is given in Fig. 6(a). The texture strengthening effect, Fig. 6(b), is similar and insignificant for both the AR plate center and the plate surface. In Fig. 6(c), the yield loci diagram of the equiaxed alpha structure with a basal texture shows a 60% increase in strength in the tension-tension quadrant over the randomly-oriented AR Ti-6211. However, the texture strengthening effect for the compression-compression quadrant is not as pronounced due to the operation of $\{10\bar{1}2\}$ deformation twins in quadrant III, as shown in Fig. 7. In addition, the texture strengthening effect for pure tension and pure compression is negligible because of the ease of operation of $\{10\bar{1}0\}\langle 11\bar{2}0\rangle$ slip. The yield loci diagram for the equiaxed alpha structure with a transverse texture, Fig. 6(d), illustrates that the texture strengthening effect is about 6% in pure tension. For the simple compression tests, the yield strength for path 4 loading is about 16% greater (about 100 MPa) than that for path 2 loading because $\{10\bar{1}2\}$ deformation twinning occurs along path 2 loading, as shown in Fig. 8.

Low Cycle Fatigue Properties

The fatigue cracks initiated at alpha/beta interfaces and/or slip bands, as shown in Fig. 9. Nucleation of micro-

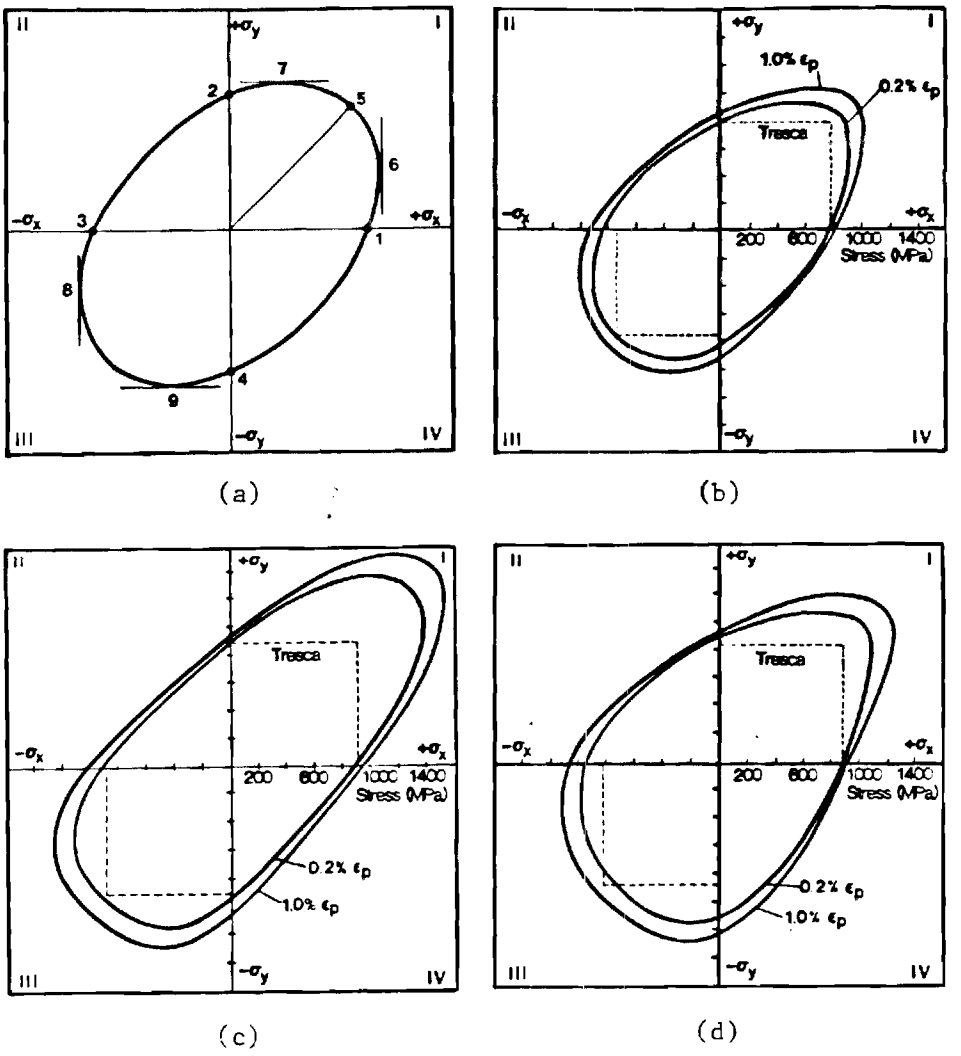

Fig. 6. (a) Path description of a yield loci diagram, (b) the yield loci diagram shows the insignificant texture strengthening effect for both the AR plate center and plate surface, (c) the yield loci diagram shows an extensive texture strengthening effect in quadrant I for the CR basal textured Ti-6211, (d) the yield loci diagram of the UR transverse textured Ti-6211 shows a 16% greater σ_{ys} along path 4 than along path 2.

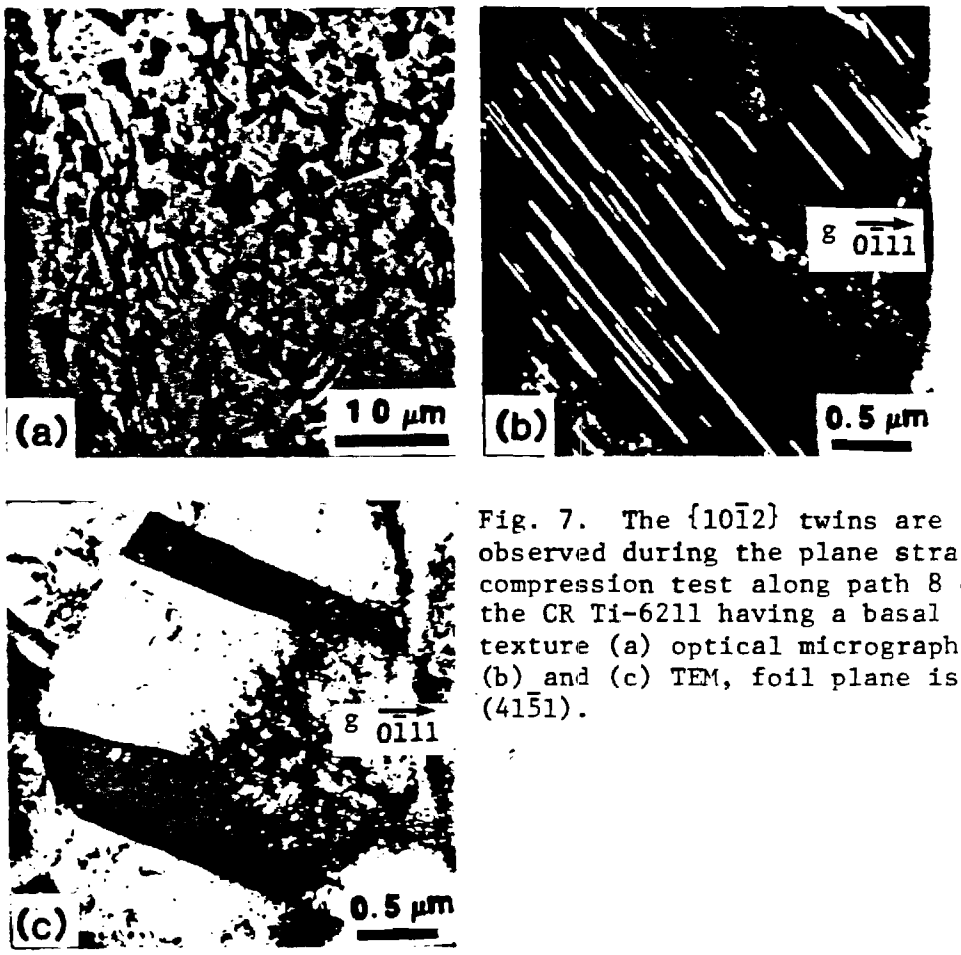

Fig. 7. The $\{10\bar{1}2\}$ twins are observed during the plane strain compression test along path 8 of the CR Ti-6211 having a basal texture (a) optical micrograph, (b) and (c) TEM, foil plane is $(41\bar{5}1)$.

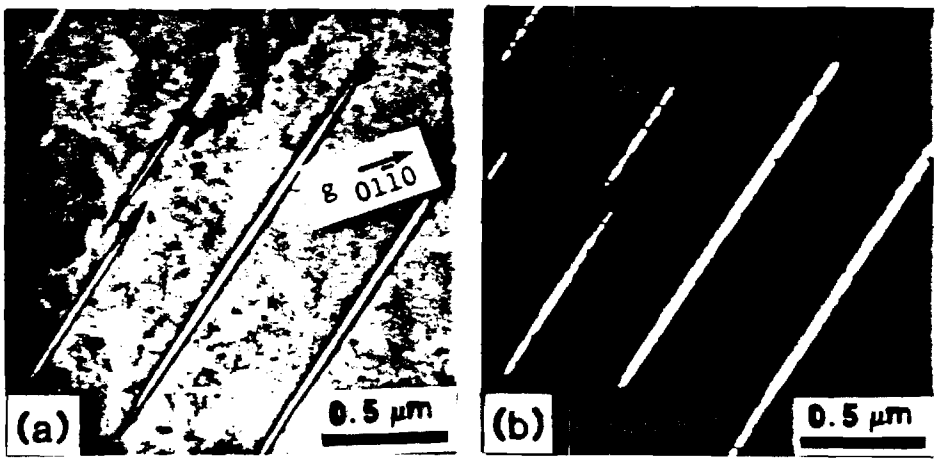

Fig. 8. (a) Bright field and (b) dark field TEM's show $\{10\bar{1}2\}$ deformation twins along path 2 loading of the UR Ti-6211 having a transverse texture. Foil plane is $(10\bar{1}1)$.

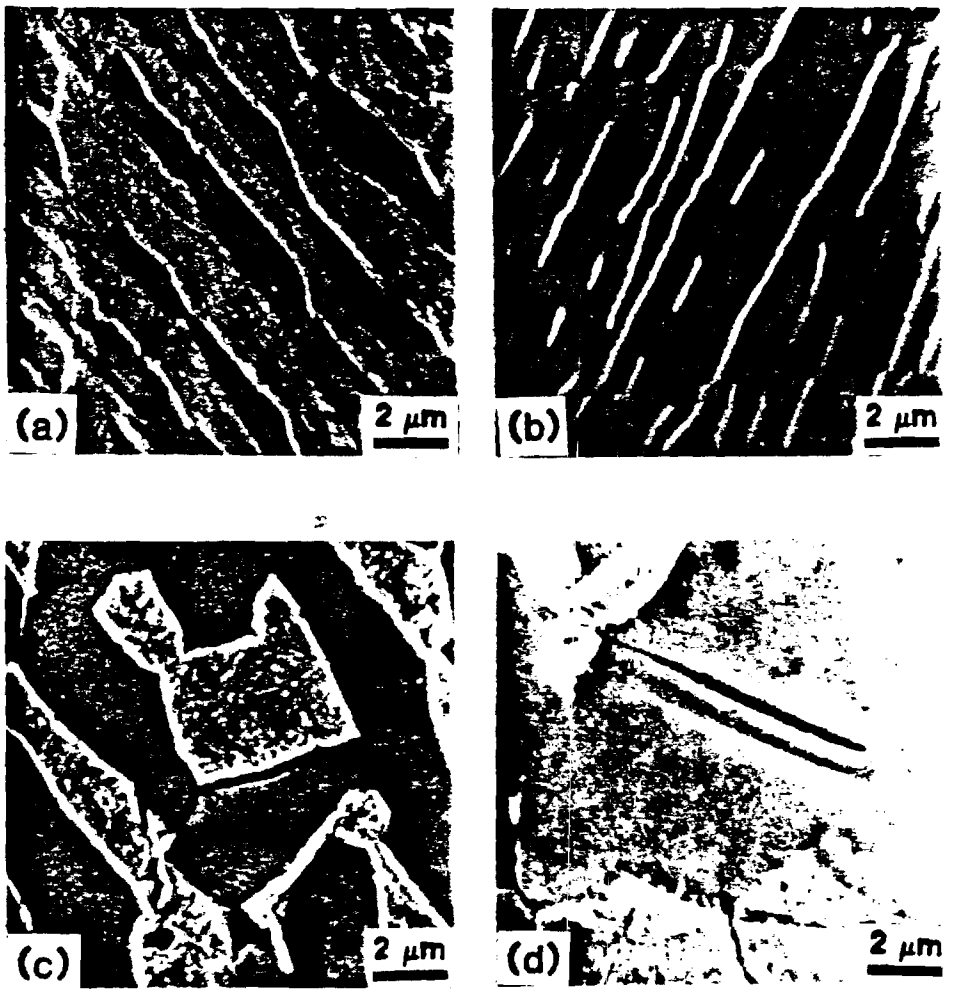

Fig. 9. (a) Fatigue cracks nucleate at alpha/beta interfaces for most of the Widmanstätten-type structures, except (b) cracks nucleate at slip bands when the AR Ti-6211 is tested at 1.5% total strain amplitude; (c) cracks nucleate at interfaces for most of the CR and UR Ti-6211, except in (d) the UR Ti-6211 when stressed parallel to the RD, the cracks nucleate at slip bands. The SA was along the vertical direction of this figure.

cracks at slip bands is only observed for the AR Ti-6211 tested at 1.5% total strain amplitude (cracks also nucleate at interfaces) or when the unidirectional-rolled material is stressed parallel to the RD. Cracks nucleate at alpha/beta interfaces for the other conditions examined. For both types of micro-

structures, the incompatability between alpha and beta (or transformed beta) phases enhances fatigue crack initiation at alpha/beta interfaces. This initiation mechanism may also be associated with an alpha/beta interface phase (1,16).

Fig. 10 shows representative cyclic stress response curves for the LCF tests. At high total strain amplitude (1.5%) the materials cyclically harden in the first few cycles as the dislocation density increases, and then soften until fracture occurs. Cyclic softening was observed during the first cycle at lower strain amplitudes. The cyclic softening may be associated with the formation of microcracks since its occurrence correlates well with the first observation of fatigue cracks.

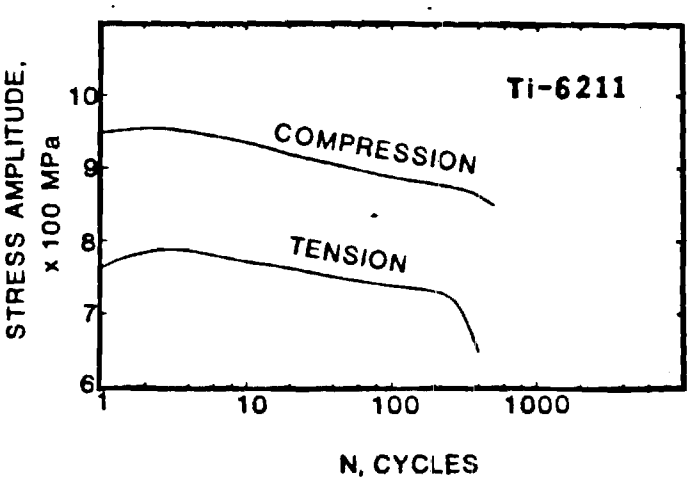

Fig. 10. A representative cyclic stress response curve during the LCF tests.

The strain-life curves along with the fatigue-ductility coefficient, ε_f', and the fatigue-ductility exponent, c, for all conditions studied are presented in Fig. 11. During the strain controlled LCF tests, the strain-life of the AR Ti-6211 is greater than that of the H1 material over a comparable strain range. This result is associated with the higher incompatability between alpha and beta (or martensite) for the H1 material since the beta has transformed to martensite during the thermal treatment. The break-points of these curves could be due to either strain localization or environmental effects.

The equiaxed alpha structures show a greater strain-life than the Widmanstätten-type structures. This may be due to the fine equiaxed structure producing a more homogeneous deformation mechanism (11). The LCF behavior for both the cross-rolled and the unidirectional-rolled (when the SA is parallel to the TD) material is identical. Moreover, the transverse textured Ti-6211 with the SA along the RD shows the best strain-life behavior. This may be a result of the cracks nucleating at slip bands instead of at interfaces.

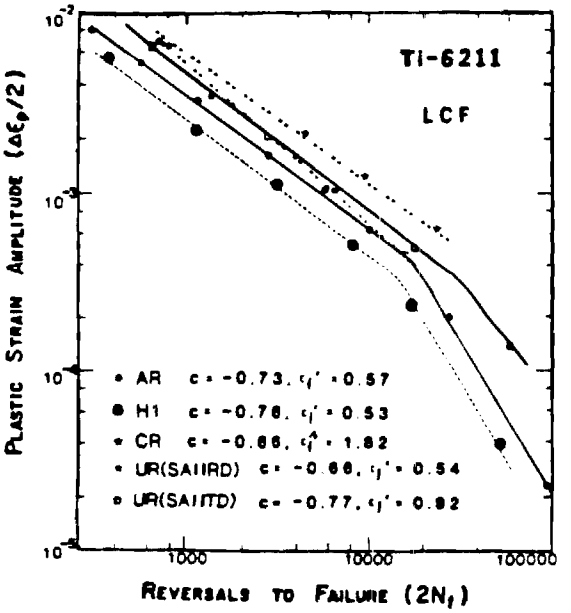

Fig. 11. The strain-life curves of Ti-6211 for all conditions tested.

SUMMARY

This study has investigated the influence of microstructure and texture on the monotonic and LCF properties of Ti-6211. A high-strength, high-ductility and high-strain-life combination is achieved by developing an equiaxed alpha microstructure completely surrounded by a strong alpha + martensite deformation barrier by appropriate ITMT processing and recrystallization treatment. The equiaxed alpha structure possesses a basal or transverse texture depending on the deformation process and the deformation temperature in the alpha + beta phase field. Microcracks were observed to nucleate at alpha/beta interfaces and/or slip bands during the LCF tests. The beta phase of the AR microstructure, Widmanstätten alpha + beta,

transforms to martensite and accounts for a 22% increase in strength without significant loss in ductility by the H1 treatment. The increase in strength is associated with a decrease in deformation barrier spacing. However, the associated decrease in incompatability between alpha and beta decreases the LCF life.

ACKNOWLEDGMENT

We gratefully acknowledge the support provided by the Office of Naval Research under Grant No. ONR C-N00014-79-C-0207 and the guidance of Dr. Bruce A. MacDonald, Program Manager. Discussions with Drs. A. Gysler and S. B. Chakrabortty were invaluable and very much appreciated.

REFERENCES

1. F. S. Lin, E. A. Starke, Jr., S. B. Chakrabortty, and A. Gysler, "Investigation of the Effect of Microstructure on the Deformation Modes and Mechanical Properties of Ti-6Al-2Nb-1Ta-0.8Mo," ONR C-N00014-79-C-0207, to be published.

2. N. E. Paton, J. C. Williams, J. C. Chesnutt, and A. W. Thompson, "The Effect of Microstructure on the Fatigue and Fracture of Commercial Titanium Alloys," AGARD-CP-185, 1975, p. 4-1.

3. R. A. Wood, and R. J. Favor, *Titanium Alloys Handbook*, MCIC-HB-02, Battelle, Columbus Laboratories, Ohio, 1972.

4. J. C. Chesnutt, A. W. Thompson, and J. C. Williams, "Influence of Metallurgical Factors on the Fatigue Crack Growth Rate in Alpha-Beta Titanium Alloys," AFML-TR-78-08, 1978.

5. S. F. Frederick, and G. A. Lenning, "The Influence of Prior Texture on the Cold Rolled Texture of Ti-6Al-4V," Met. Trans., Vol. 6A, 1975, p. 1467.

6. F. Larson and A. Zarkades, "Properties of Textured Titanium Alloys," MCIC-74-20, Battelle, Columbus Laboratories, Ohio, 1974.

7. M. J. Blackburn, J. A. Feeney, and T. R. Beck, "Stress-Corrosion Cracking of Titanium Alloys," *Advances in*

Corrosion Science and Technology, ed. by M. G. Fontana and R. W. Staehle, Vol. 3, Plenum Press, New York, 1973, p. 67.

8. M. Peters, and G. Lütjering, "Control of Microstructure and Texture in Ti-6Al-4V," *Titanium '80 Science and Technology*, ed. by H. Kimura and O. Izumi, Vol. 2, 1980, p. 925.

9. J. C. Williams, "Critical Review, Kinetics and Phase Transformation," *Titanium Science and Technology*, ed. by R. I. Jaffee and H. M. Burte, Vol. 3, Plenum Press, New York, 1973, p. 1433.

10. E. S. Meieran, "Use of the Reciprocal Lattice for the Development of a New Pole Figure Technique," Rev. Sci. Ins., Vol. 33, No. 3, 1962, p. 319.

11. ASTM Standards, "Standard Methods of Tension Testing of Metallic Materials," E8-69, Pt. 10, 1974, p. 90.

12. B. I. Sandor, *Fundamentals of Cyclic Stress and Strain*, University of Wisconsin Press, Madison, Wisconsin, 1972, p. 45.

13. M. J. Blackburn and J. C. Williams, "The Preparation of Thin Foils of Titanium Alloys," Trans. TMS-AIME, Vol. 239, 1967, p. 287.

14. D. Lee and W. A. Backofen, "An Experimental Determination of the Yield Locus for Titanium and Titanium Alloy Sheet," Trans. TMS-AIME, Vol. 236, 1966, p. 1096.

15. M. Peters, A. Gysler, and G. Lütjering, private communication, Ruhr-Universitat, Bochum, West Germany, 1980.

16. J. C. Chesnutt, C. G. Rhodes, and J. C. Williams, "Relationship between Mechanical Properties, Microstructure, and Fatigue Topography in Alpha + Beta Titanium Alloys," Fractography-Microscopic Cracking Processes, ASTM STP 600, 1976, p. 99.

17. E. A. Starke, Jr. and G. Lütjering, "Cyclic Plastic Deformation and Microstructure," *Fatigue and Microstructure*, ed. by M. Meshii, ASM, 1978, p. 205.

E-19-678

INVESTIGATION OF THE EFFECT OF MICROSTRUCTURE ON THE DEFORMATION MODES AND MECHANICAL PROPERTIES OF Ti-6Al-2Nb-1Ta-0.8Mo*

D. M. Bowden, R. T. Chen, F. S. Lin, S. Shih and E. A. Starke, Jr.
Fracture and Fatigue Research Laboratory
Georgia Institute of Technology
Atlanta, GA 30332
USA

Abstract

This report is concerned with the effect of microstructure and deformation mode on the monotonic, cyclic and creep properties of Ti-6211 from room temperature to the beta transus temperature. The microstructures examined include the Widmanstatten structure of the as-received beta processed material, those that develop in the heat affected zone of a weld, and those that were shown previously to have an excellent combination of strength and ductility. Specifically, the influence of microstructural parameters on the hot ductility dip observed in Ti-6211, room temperature creep, low cycle fatigue and fatigue crack propagation is discussed in this report.

*Office of Naval Research Contract No. N00014-79-C-0207.

Introduction

Materials for advanced hydrospace applications must provide an optimum weight displacement ratio and have structural reliability. The latter requires that the materials possess high strength, ductility, and fracture toughness, and have a high resistance to corrosion, stress corrosion, and creep in a salt water environment. A promising candidate for future hydrospace applications is the alpha + beta alloy Ti-6211 (Ti-6Al-2Nb-1Ta-0.8Mo).

The properties of alpha + beta titanium alloys such as Ti-6211 are very sensitive to both microstructure and crystallographic texture. These features can be controlled, to a large extent, by proper manipulation of primary processing variables, e.g., temperature and method of working, and subsequent heat treatment, etc. For any structural application, it is important to understand the relationship between microstructure, texture, and mechanical properties in order to distinguish desirable from undesirable features. It is also important to determine the processing procedures required to produce the desired microstructure and texture. These are the primary objectives of this research program. Specifically, the scope of our research includes five major tasks:

1. Determine the relationship between the microstructural features that can be controlled by processing and the monotonic properties.

2. Determine the role of deformation mode and degree of strain localization on the strength and ductility from room temperature to the beta transus. Various microstructures are being examined with the goal of understanding the hot ductility dip observed in certain heat treated conditions of this alloy.

3. Determine the individual effects of texture (using materials with the same microstructure) and of microstructure (using materials with the same texture) or mechanical properties.

4. Determine the relationship between microstructure and the creep behavior.

5. Determine the relationship between the microstructural features that can be controlled by processing and fatigue performance.

This report concerns our recent results on tasks 2, 4, and 5. Tasks 1 and 3 have been discussed extensively in previous reports. Task 2 involves the effects of welding on structure and properties in this alloy. A major requirement of materials for structural applications is good weldability. Weldability is essential if full advantage is to be taken of the improved properties of Ti-6211 in economical and efficient production of structural assemblies. Studies of this and similar alloys indicate that Ti-6211 is susceptible to severe hot ductility loss when it has experienced thermal cycles typically found in the heat affected zone (HAZ) of a weldment (1,2). This hot ductility loss is considered an indication of susceptibility to hot cracking during welding. The conditions which promote low (less than 20%) reduction in area involve thermal cycling to a peak temperature between 1100-1700°C followed by rapid cooling to 750-850°C and stressing in tension. Low hot ductility is also exhibited by specimens thermally cycled to a peak temperature between

1100-1700°C and rapidly cooled to room temperature upon heating directly to 750-850°C. The thermal cycle which promotes hot ductility loss is illustrated in Figure 1. These conditions are expected to exist in the near-HAZ adjacent to the fusion zone (FZ) of the weld. Hot ductility loss is exhibited by several titanium alloys as shown in Figure 2.

The objectives of research in this area are to investigate the mechanisms responsible for the observed hot ductility dip. A major question to be answered is whether the hot ductility dip is the result of rapid thermal cycling experienced during welding, or is controlled by metallurgical factors such as microstructure and deformation behavior. If the hot ductility loss is microstructure controlled, then this phenomenon is important not only in weld cracking, but in any forming operation where good elevated temperature ductility is required.

Since the alloy Ti-6211 will be used for structural applications requiring welding, it is also important to examine the effects of welding on monotonic properties. It has been well recognized that titanium and its alloys are subject to an appreciable amount of creep at ambient temperature (3-8). The different microstructures generated in the fusion and heat-affected zones of alloy weldments may exhibit different creep behavior from the base metal structure. The effects of microstructure on room temperature creep behavior are being examined in Task 5.

Finally, in Task 4, the relationships between processing, texture, microstructure, and fatigue properties in Ti-6211 are being examined. This study includes the effects of structure and texture on low cycle fatigue (LCF) and the fatigue crack propagation (FCP) behavior, as well as deformation and fracture modes.

Experimental Procedures

The Ti-6211 material used in this investigation was supplied in the form of 1.0 inch thick beta-processed plate by the David W. Taylor Naval Ship Research and Development Center, Annapolis, MD. The chemical composition is given in Table I.

The microstructure and texture developed during thermal and mechanical processing depend on the temperature used, as illustrated in the phase diagram of Figure 3. Processing at temperatures above the beta transus results in the formation of Widmanstatten-type microstructures. Air cooling from the beta phase field forms the Widmanstatten plus grain boundary alpha (W + GBα) phase morphology in the beta matrix. This structure will have a random texture, since recrystallization has occurred in the beta phase field. Rapid quenching from above the M_S temperature transforms the beta phase to martensite. For specimens quenched from above the beta transus, the structure will be all martensite. Quenching from a temperature high in the alpha plus beta phase field above the M_S temperature but below the beta transus results in a mixture of alpha and martensite. Equiaxed alpha phase morphologies are produced by working at temperatures below the beta transus followed by recrystallization annealing treatments within the alpha + beta phase field. As is the case for Widmanstatten type structures, the beta phase may be transformed to martensite by rapid quenching from annealing temperatures above the M_S temperature, producing a mixture of equiaxed alpha and martensite.

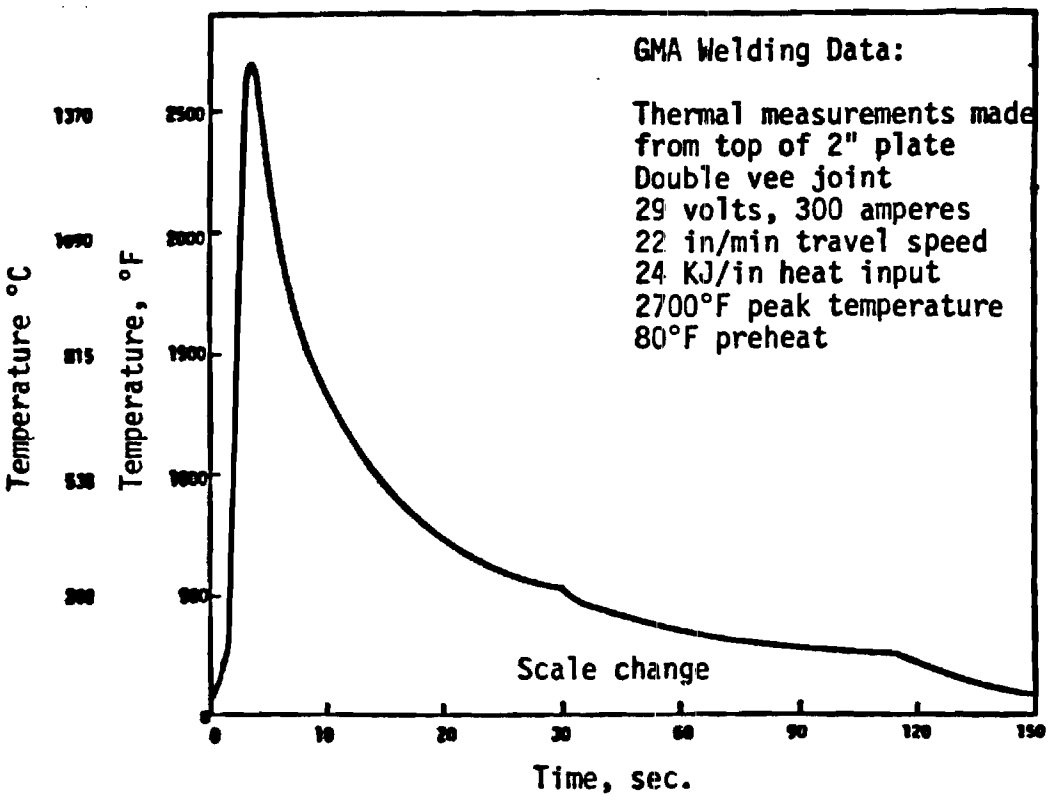

Figure 1. Synthetic "Gleeble" weld thermal cycle for hot ductility loss.

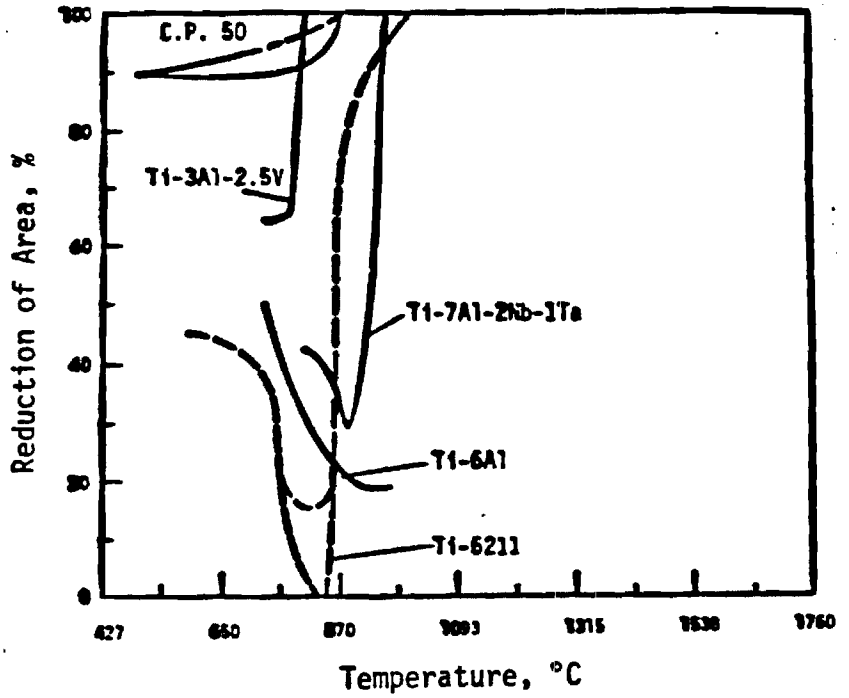

Figure 2. Hot ductility of selected titanium alloys. Reduction in area measured on cooling from 2800-3000°F peak temperature.

TABLE I. Chemical Composition*

Al	Nb	Ta	Mo	O	N	H	C	Y	Mn	Si	Ti
5.6	2.16	0.95	0.79	0.066	0.007	0.0046	0.02	0.002	0.01	0.01	Bal.

* weight percent

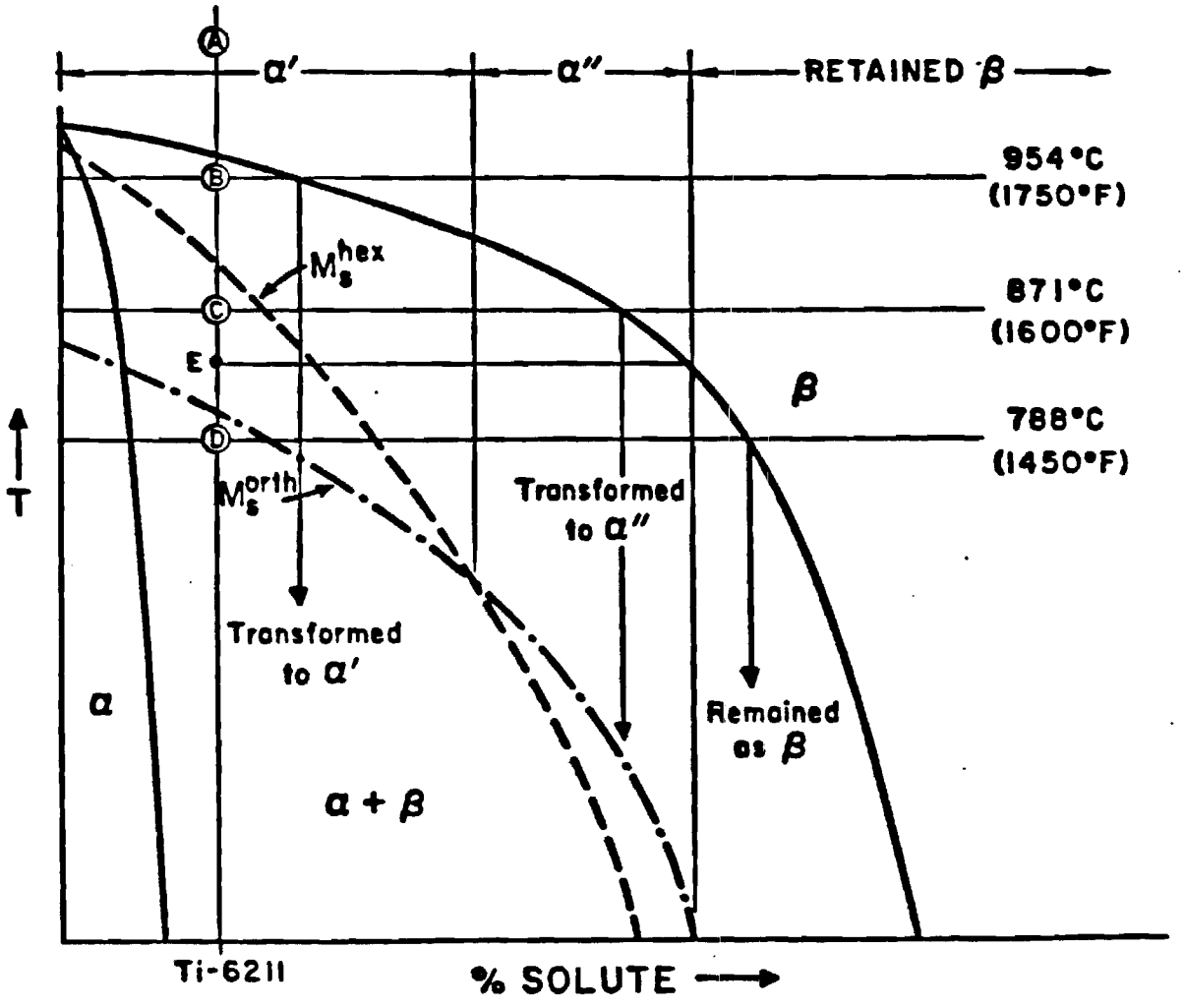

Figure 3. Phase diagram for beta-isomorphous alpha + beta alloys.

Hot Ductility Dip Studies

To investigate the role of microstructural variables in producing the observed hot ductility dip, a variety of microstructures were produced by laboratory heat treatments. These heat treatments were selected to produce microstructures with variable alpha phase morphology, beta grain size and shape, and different combination of phases in order to determine the effects of these variables on hot ductility behavior. These heat treatments and resultant microstructures are listed in Table II.

Tensile tests for Task 2 were conducted at room temperature, 500°C, and 800°C. Cylindrical tensile specimens with a gage section 1.0" in length and 0.160 inch in diameter were machined prior to heat treatment. All heat treatments were conducted in flowing high purity argon atmosphere. Tensile tests were performed on an Instron machine equipped with an Instron model A1017-301 three-zone furnace. Tests were carried out in flowing high purity argon atmosphere. After heat treatment, specimens were ground through 600 grit silicon carbide paper and polished with 1.0 micron Al_2O_3 prior to testing. Temperature was monitored by a chromel-alumel thermocouple attached to the specimen grip assembly. Specimens were loaded into the capsule assembly with flowing argon, and the capsule was lowered into the furnace. The test was begun when the specimen reached the desired test temperature as indicated by the thermocouple monitor. The time required to reach test temperature averaged about 10 minutes. Tests were conducted at a crosshead speed of 0.02 inch per minute with a strain rate of 2.0% strain per minute. Upon completion of the test, the specimen capsule was removed from the furnace and allowed to cool in flowing argon. To prevent oxidation of the specimen fracture surface, the specimen was removed from the capsule assembly only after the temperature had cooled to 200°C.

Optical metallography was used for basic microstructural observation. Specimens were ground through 600 grit silicon carbide paper, and electropolished using a solution of 5% H_2SO_4 by volume in methanol cooled to -20°C. The polishing operation was carried out in one minute at 14 volts DC using a platinum cathode in a slowly stirred solution. Immediately following polishing, the specimen was washed in methanol and dried. The specimen was then etched for 10 seconds using a solution of 10 ml HF, 30 ml HNO_3 and 50 ml H_2O (Kroll's reagent).

Microstructural and deformation studies were carried out by the use of transmission electron microscopy (TEM). TEM specimens were prepared from 0.015 inch thick wafers cut from bulk specimens by electropolishing using a Tenupol polishing apparatus. Electropolishing was carried out at -25°C using a solution of 300 ml methanol, 175 ml n-butanol, and 30 ml perchloric acid at a potential of 14 volts DC. Polished specimens were rinsed in chilled methanol as a final preparation step.

Fracture surfaces of tensile specimens were examined by scanning electron microscopy (SEM). For some specimens, a technique was used for simultaneous examination of the fracture surface and underlying microstructure (9). In this technique, a portion of the fracture surface is masked off with a lacquer applied with a fine brush. Once the lacquer has dried, the specimen is electropolished using the same conditions as in optical metallography. After etching the polished specimen, the lacquer is dissolved, and the specimen is cleaned in acetone in an ultrasonic cleaner. The fracture surface protected by the

TABLE II. Heat Treatments and Microstructures

Condition	Heat Treatment	Microstructure
*W-1**	As-received beta processed plate	Widmanstatten alpha + beta with grain boundary alpha. Prior beta grains are elongated in the working direction.
*W-2	1050°C/40 min/AC	Widmanstatten alpha + beta with grain boundary alpha. Beta grains are equiaxed due to recrystallization above the beta transus.
*W-3	1050°C/40 min/WQ	Martensite with equiaxed grains.
W-4	1050°C/2 hr/WQ	Martensite with large equiaxed beta grains.
W-5	800°C/40 min/WQ	Widmanstatten alpha + beta with grain boundary alpha and elongated prior beta grains.
W-6	950°C/40 min/WQ	Widmanstatten alpha + transformed beta with grain boundary alpha in elongated prior beta grains.
W-7	1050°C/40 min/AC + 950°C/40 min/WQ	Widmanstatten alpha + transformed beta with grain boundary alpha in elongated prior beta grains.
W-8	1050°C/40 min/AC + 950°C/4 hr/AC	Widmanstatten alpha + beta (basket weave type) + thick grain boundary alpha.
W-9	1050°C/40 min/WQ + 950°C/4 hr/AC	Tempered martensite with grain boundary alpha
W-10	970°C/40 min/WQ + 500°C/2 hr/AC	Widmanstatten alpha + aged martensite
G-1	Thermally cycled Gleeble specimens	Widmanstatten titnaium martensite with equiaxed prior beta grains
E-1	HR 850°C/WQ + 800°C/1 hr/WQ	Equiaxed alpha + beta
E-2	1050°C/40 min/WQ + CR/850°C/WQ + 940°C 1 hr/WQ + 500°C/2 hr/ AC	Equiaxed alpha + aged martensite (basal texture)
E-3	1050°C/40 min/WQ + UR/960°C/WQ + 940°C/1 hr/WQ + 500°C/2 hr/AC	Equiaxed alpha + aged martensite (transverse texture)

* Microstructure used for creep studies
** Microstructure used for fatigue studies

lacquer remains unaffected, and provides for the correlation of fracture path with microstructure revealed in the polished and etched portion of the fracture surface.

Creep Studies

In addition to examining the effects of welding on hot ductility, the room temperature creep behavior of typical weld zone microstructures has also been studied. This work includes investigation of creep behavior of the as-received beta-processed plate material as well as four microstructures produced by laboratory heat treatments which may typically be found in alpha + beta alloy weldments. These heat treatments and microstructures are designated with an asterisk in Table II. Tensile properties were determined using cylindrical specimens tested on an MTS machine at a strain rate of 10^{-3}/sec. Strains were measured with an 8 mm clip-on extensometer.

Cylindrical creep specimens with a gage section 20 mm in length and 5 mm in diameter were cut with the stress axis parallel to the rolling direction of the as-received plate. Creep tests were performed on four dead-weight-loaded, lever-arm type frames obtained from the Naval Air Development Center. High precision resistor-type foil gages were used for creep-strain measurements. A schematic of the strain measuring unit is shown in Figure 4. With this setup, four strain gages could be operated and recorded in sequence with only one strain indicator. All room temperature creep tests were conducted in the laboratory air environment.

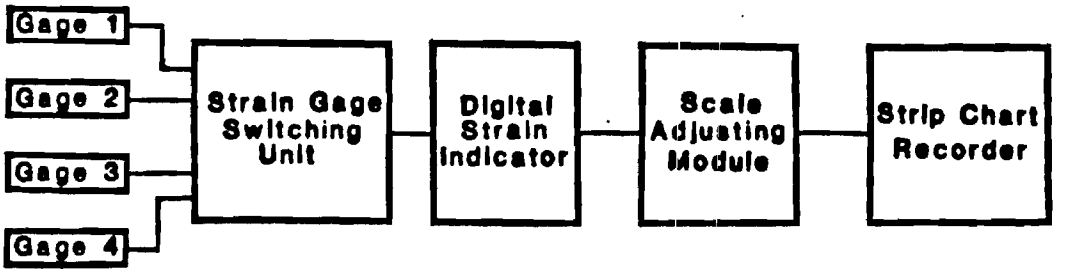

Figure 4. Schematic diagram of strain measuring unit

Cylindrical specimens with a gage section 14 mm in length and 4 mm in diameter were prepared for cyclic creep tests. These tests were conducted on an MTS machine using a clip-on extensometer for strain measurement, employing a square-wave loading spectrum. The extensometer was calibrated against the foil strain gage used for static creep tests, so that the results of cyclic creep may be compared directly with those of static creep tests.

Optical metallography was used for basic microstructural characterization. TEM was used to study dislocation substructures and strain distribution in creep specimens. Three parallel scratches were inscribed along the gage section to monitor grain boundary sliding during creep. Replicas taken from specimen surfaces were examined by SEM to determine the extent of grain boundary sliding. Since two stage replica TEM micrographs show much better con-

trast, this method was used to examine the specimen surface for voids and microcracks.

Fatigue Studies

To examine the relationships between processing, texture, microstructure, and fatigue properties, the low cycle fatigue (LCF) and fatigue crack propagation (FCP) behavior have been determined for three types of microstructures (Widmanstatten alpha + beta and alpha + martensite with random textures, and equiaxed alpha + martensite with basal or transverse textures). The structures used for the fatigue studies are designated by a double asterisk in Table II.

Metallography samples were taken from the longitudinal short transverse plane. Pole figures of (0002), $(10\bar{1}0)$, $(10\bar{1}1)$, and $(11\bar{2}0)$ reflections were measured using a Siemens goniometer with filtered CuK_α radiation, using the Schultz reflection method. Data collected over a polar orientation range from 0 to 70 degrees were converted to pole figures. In some cases, a pole figure technique (10) which averages texture through the plate thickness was applied to obtain a pole figure completely within one quadrant from 0 to 90 degrees. A complete pole figure can be generated by mirror reflecting the texture information about the transverse and rolling direction lines.

LCF and FCP specimens were machined according to ASTM Standard E8-69 (11) and E399-74 (12), respectively. Notches were machined after heat treatment to prevent residual stresses at the crack tip. All specimens were mechanically polished through 1.0 micron diamond paste prior to testing. Both LCF and FCP tests were conducted on an electrohydraulic closed-loop MTS test system. The LCF tests were conducted with an 8 mm clip-on extensometer under strain control at a strain rate of 0.33%/sec. The strain life curves were constructed by plotting the plastic strain amplitude,

$$\Delta\varepsilon_p/2 = \varepsilon'_f(2N_f)^c \quad \text{(ref. 13)} \qquad [1]$$

where ε'_f is the fatigue-ductility coefficient, and c is the fatigue-ductility exponent. The FCP tests were conducted under tension-tension loading with a 0.1 maximum/minimum load ratio at a frequency of 10 Hz. The stress intensity factor ranges (ΔK), calculated from the corresponding crack length, were plotted versus fatigue crack growth rate (FCGR, da/dN) in log-log scale.

A limited number of LCF specimens were electropolished using the method suggested by Blackburn and Williams (14), and lightly etched in Kroll's reagent before testing to 30% total life. They were then examined over the entire gage surface by SEM in order to observe the fatigue crack initiation sites. Fatigue crack closure of the condition was measured using clip-on COD gage. All mechanical tests were performed at room temperature in laboratory air (298K, 60% relative humidity).

Fracture surfaces of FCP samples were examined to determine the fracture modes by SEM. Again, the technique of simultaneous observation of fracture surface and underlying microstructure was used to correlate fracture mode with microstructure.

Results and Discussion

Hot Ductility

The microstructure of the beta processed plate used in this study is shown in Figure 5. The optical micrograph of Figure 5a shows the Widmanstatten + grain boundary alpha phase morphology with alpha platelets formed in groups of parallel plates, or colonies. This structure is typically formed upon air cooling from above the beta transus temperature. The prior beta grains are elongated due to working above the beta transus. The transmission electron micrograph shown in Figure 5b shows discontinuous beta phase between the alpha platelets.

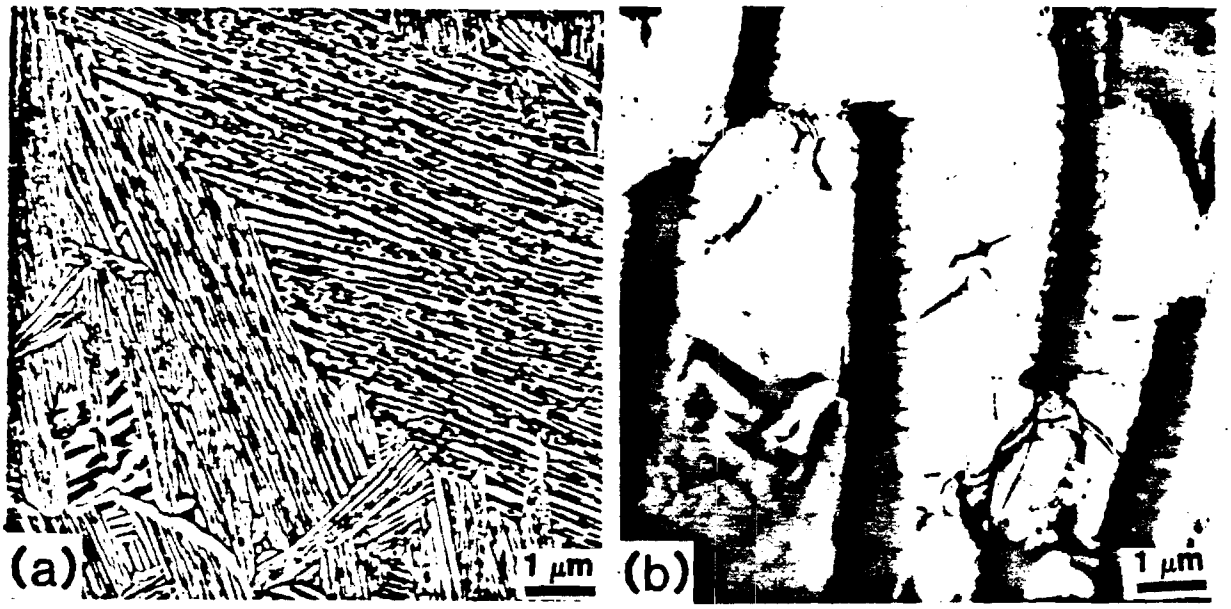

Figure 5. Microstructure of beta-processed plate: (a) optical micrograph, (b) transmission electron micrograph.

This structure shows no evidence of ductility loss, with the reduction in area increasing from 20% at room temperature to 62% at 800°C. Deformation behavior observed on the surface of a tensile specimen strained approximately 4% shows slip bands terminating at platelet colony boundaries, as shown in Figure 6a. The transmission electron micrograph of Figure 6b shows slip continuous through platelet colonies, with the beta phase between alpha platelets not acting as a barrier to slip. This is due to the precipitate orientation relationship between the alpha and beta phases in which the $(0001)\{11\bar{2}0\}_\alpha$ system in the alpha is parallel to the $(110)\langle 111\rangle_\beta$ system in the beta. Thus $(0001)\{11\bar{2}0\}_\alpha$ slip in the alpha is coplanar with $(110)\langle 111\rangle_\beta$ slip in the beta. Slip terminating at platelet colony boundaries results in void formation along those boundaries, as shown in Figure 7. Fracture in this condition occurs by void formation and coalescence resulting in ductile rupture along platelet colony boundaries. Fracture features illustrated in Figure 8 for specimens tested at room temperature, 500°C, and 800°C show ductile dimples of various sizes at all temperatures.

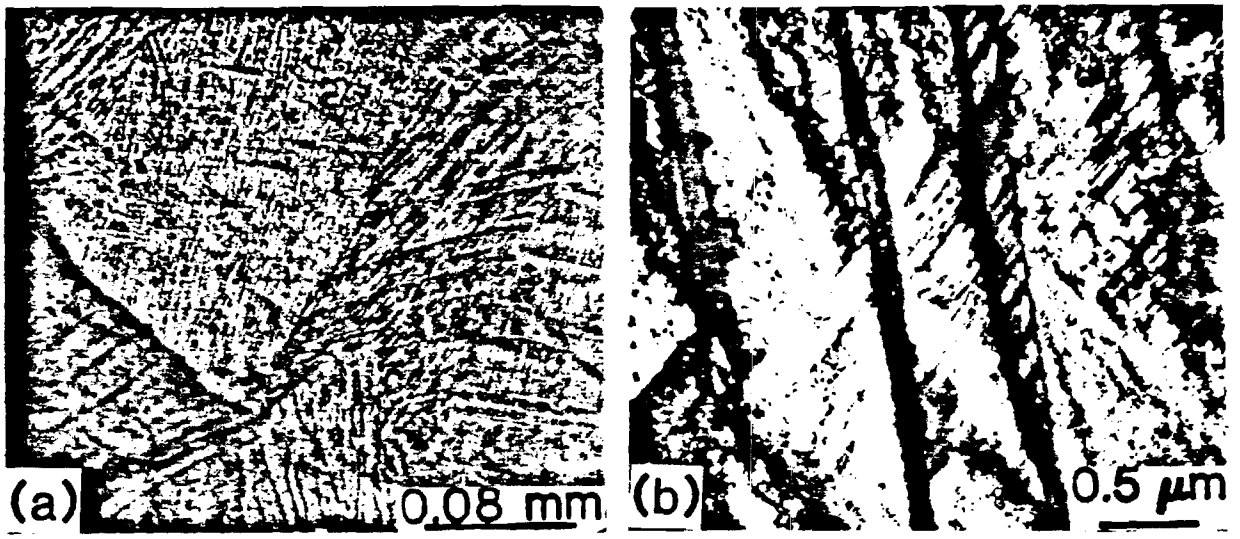

Figure 6. Deformation in condition W-1: (a) optical micrograph of slip on specimen surface, (b) TEM showing slip continuous in platelet colonies.

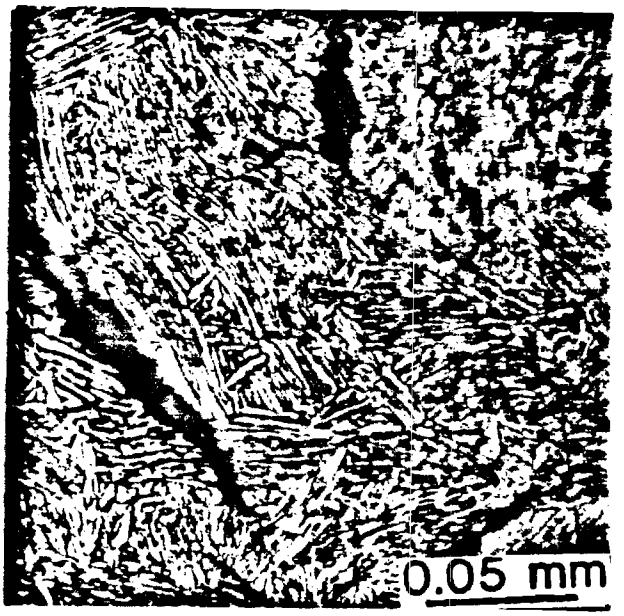

Figure 7. Optical micrograph illustrating void formation along platelet colony boundaries in condition W-1.

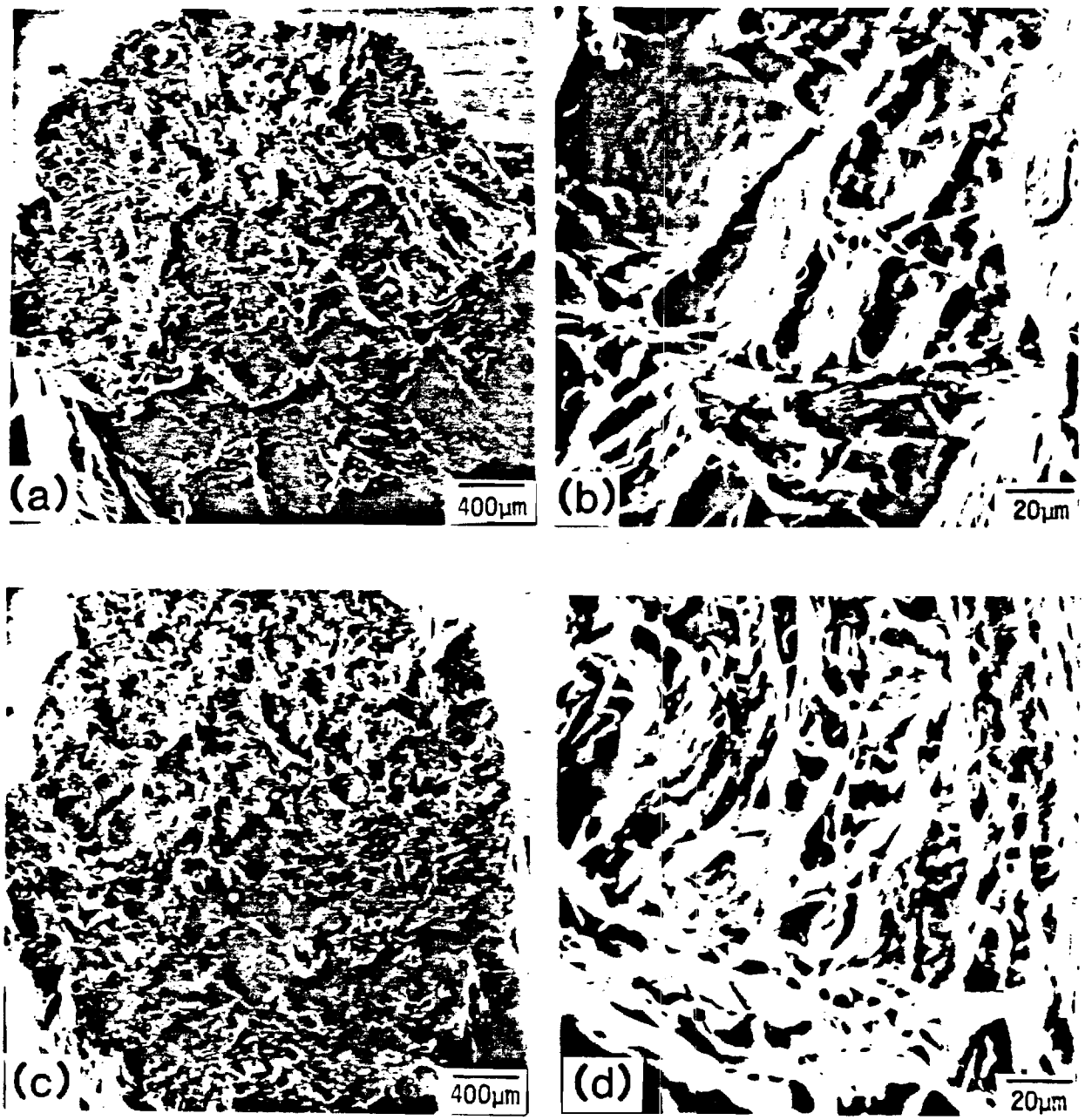

Figure 8. Scanning electron micrographs of beta-processed plate condition W-1: (a), (b) room temperature; (c), (d) 500°C; and (e), (f) 800°C.

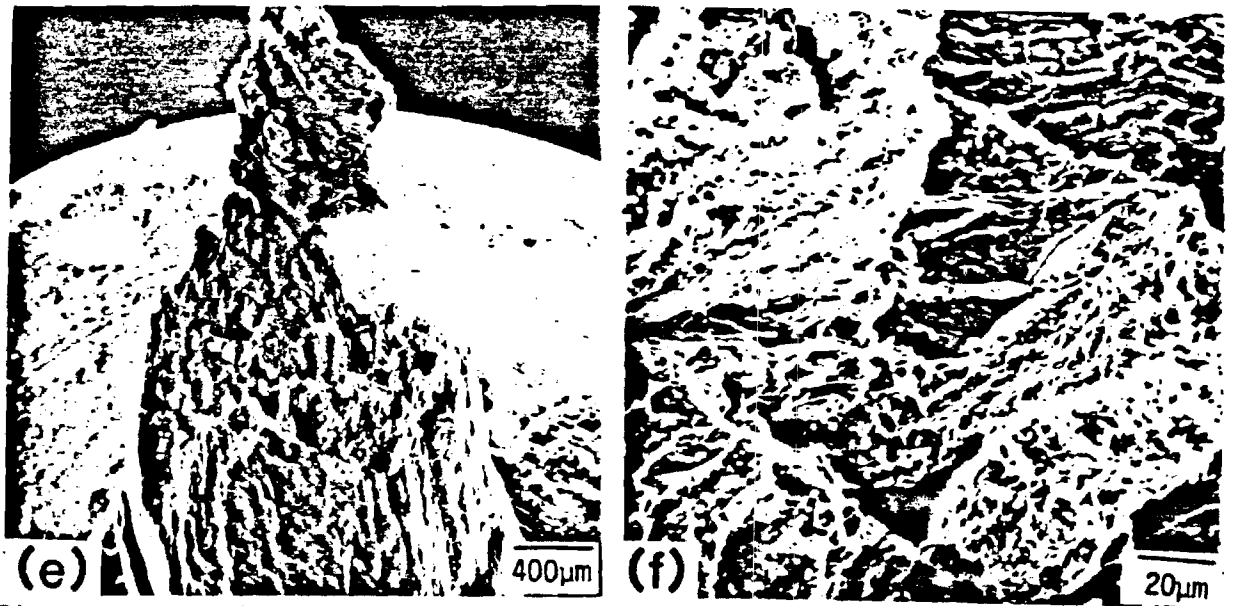

Figure 8. Continued.

Thermal cycling of the beta processed material in the Gleeble apparatus according to the time-temperature profile of Figure 1 produces the microstructure in Figure 9. This structure shows large equiaxed prior beta grains due to recrystallization above the beta transus. Subsequent rapid cooling transforms the beta to the martensitic structure containing large massive martensitic plates surrounded by smaller platelets. Scanning electron micrographs of Gleeble specimens tested at room temperature, 500°C, and 800°C are shown in Figure 10, and illustrate a drastic change in fracture appearance at 800°C. At the lower test temperatures, Gleeble specimens have ductility comparable to that of the base metal beta-processed plate, and the fracture appears very similar to that of the base metal, as shown in Figure 10a and 10b. However, at 800°C, fracture appears intergranular along the beta grain boundaries as shown in Figure 10c. Examination of the faceted regions at high magnification reveals shallow dimples indicative of a ductile rupture type failure. The abrupt change in fracture appearance at 800°C results from the fact that Gleeble specimens show a change in fracture path from base metal to weld zone with increasing temperature, as illustrated in the macrophoto of Figure 11. At lower temperatures, the weld zone is stronger than the base metal, and thus yielding and plastic strain occurs in the base metal regions of the gage section. This behavior is called overmatching and is commonly observed in the testing of weldments. However, at 800°C fracture occurs in the weld zone. The fact that high temperature exposure is required to produce low ductility intergranular fracture in the weld zone indicates that rapid structural changes occurring during high temperature exposure are responsible for ductility loss. These changes may include segregation of elemental species such as sulfur to grain boundaries, or rapid microstructural changes which could produce strain localization in the grain boundary regions. The possible effects of sulfur segregation and metallurgical variables such as alpha phase morphology, beta grain size and shape, and phases present will be discussed individually in the following sections.

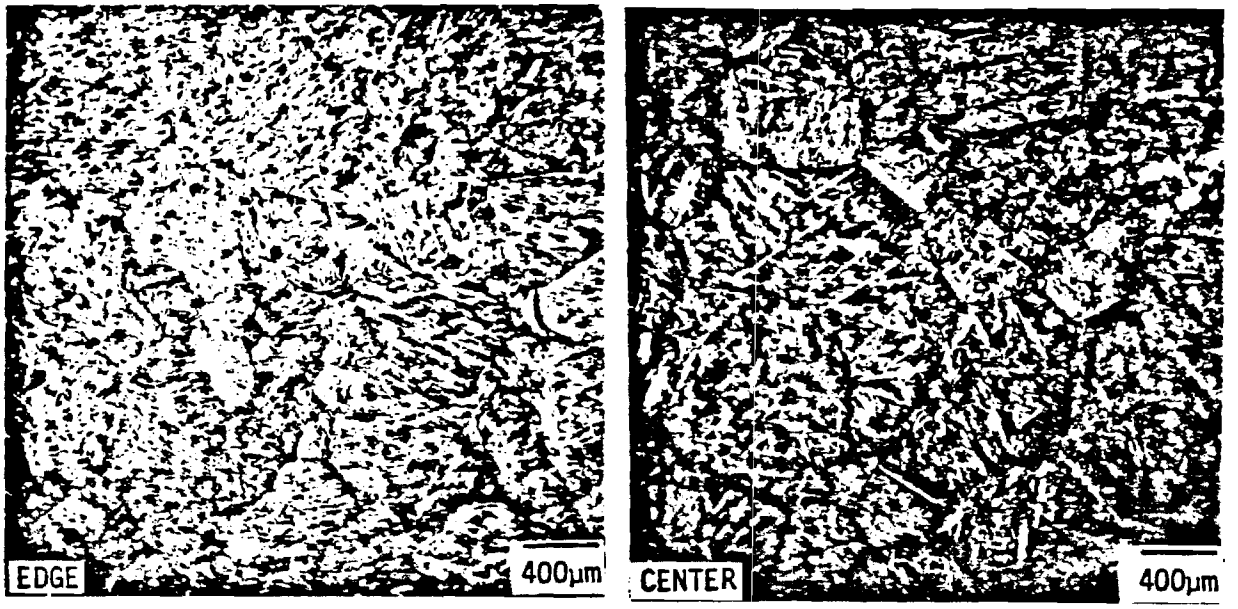

Figure 9. Optical micrograph of synthetic weld zone "Gleeble" microstructure.

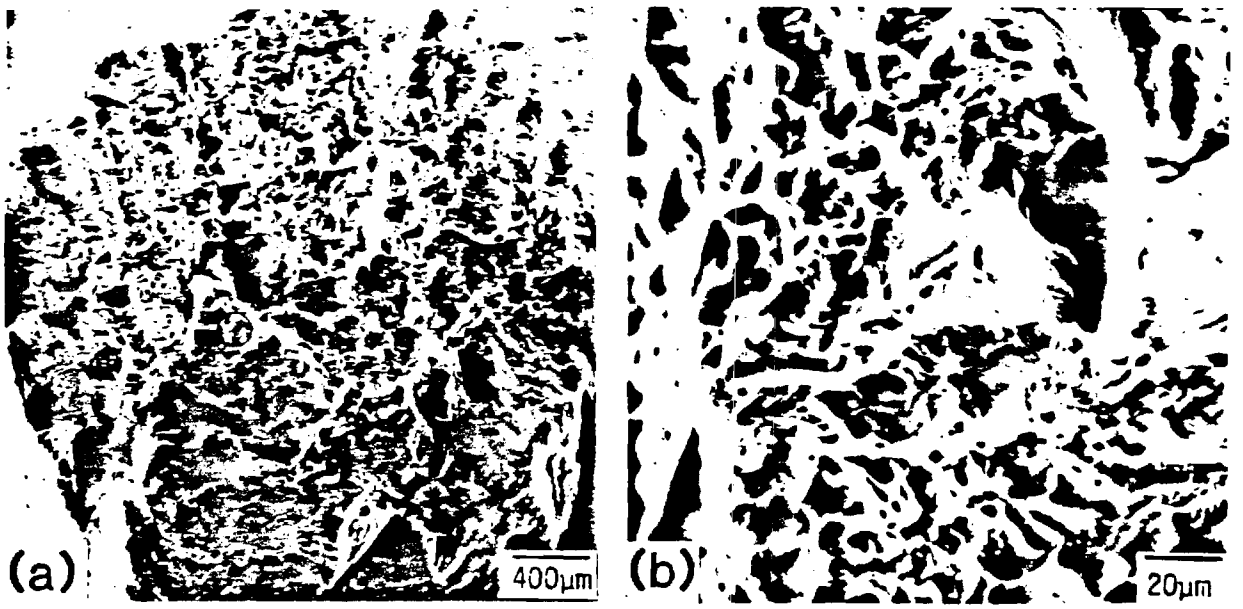

Figure 10. Scanning electron micrographs of Gleeble specimens tested at: (a), (b) room temperature; (c), (d) 500°C; and (e), (f) 800°C.

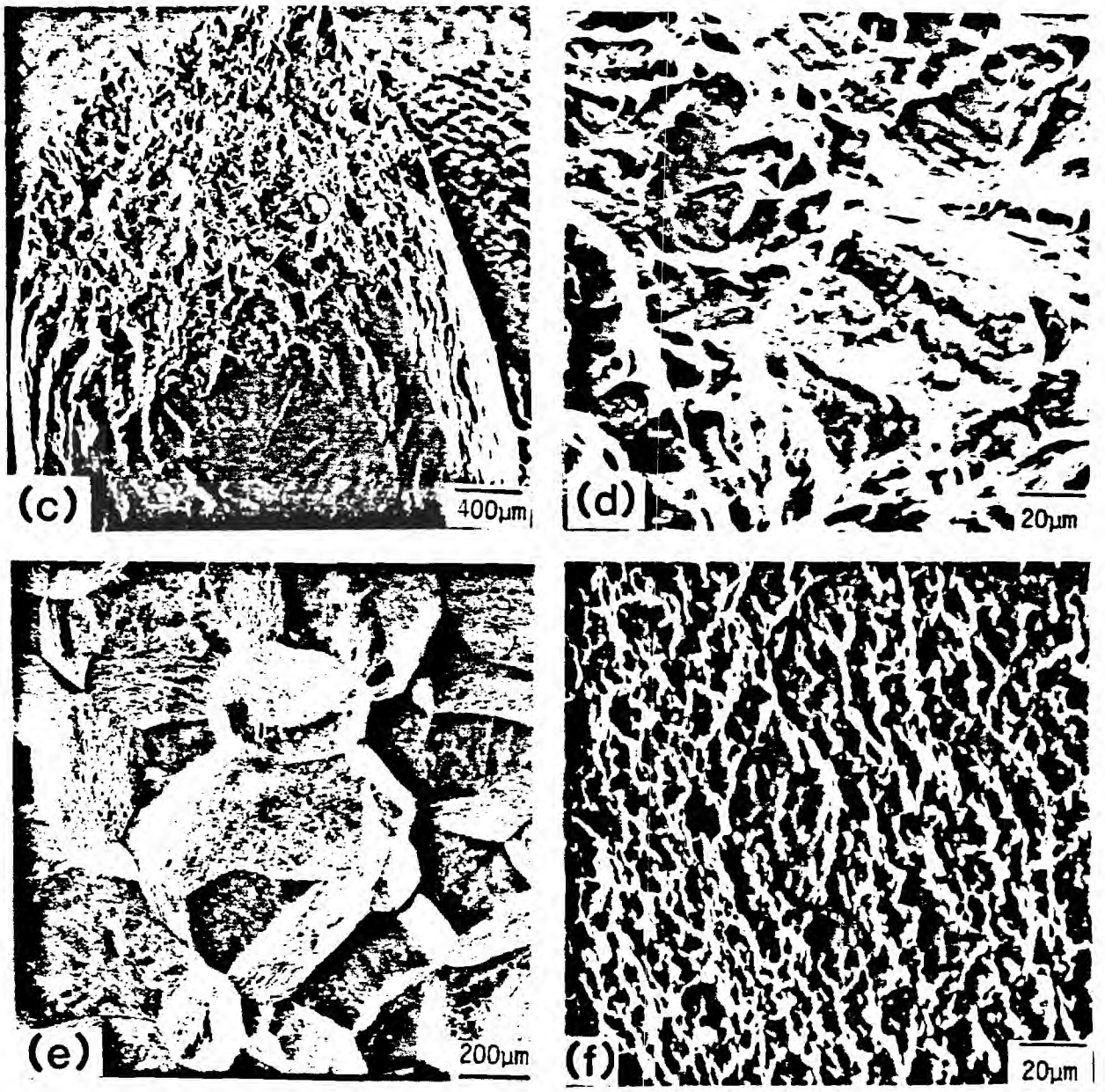

Figure 10. Continued.

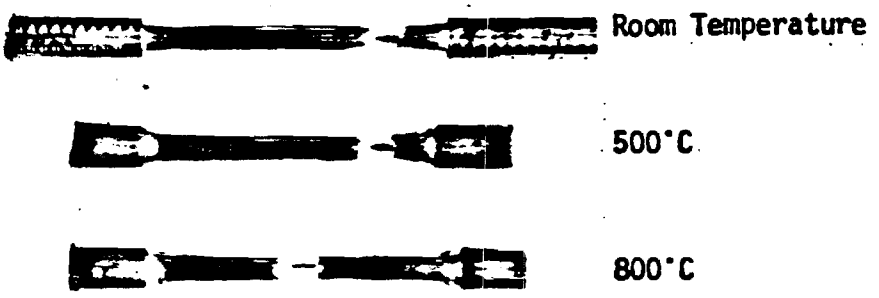

Figure 11. Macrophoto illustrating change in fracture path in Gleeble specimens as a function of test temperature.

Sulfur Segregation. As previously discussed, sulfur diffusing to the beta grain boundaries could produce an embrittling effect. High temperature exposure may be required to allow significant sulfur segregation to occur. Some segregation could occur during thermal cycling and result in the appearance of facets on the fracture surface. However, lack of time at high temperature does not produce sufficient segregation to give a completely intergranular fracture. In order to further investigate the possibility of sulfur segregation to grain boundaries, a Gleeble specimen was tested at 800°C after a hold time of 30 minutes at the test temperature. This hold time would allow sufficient time for segregation to occur and result in lower ductility. This specimen fails intergranularly as shown in Figure 12, but actually shows more ductility than Gleeble specimens tested with no hold time. This result indicates that sulfur is not responsible for producing the intergranular fracture. Also, the fact that the faceted regions show ductile dimples indicates that failure has occurred due to strain localization in the grain boundary regions rather than grain boundary embrittlement. Intergranular fracture resulting from segregation in grain boundaries generally produces smooth faceted regions due to decohesion of the grain boundaries, rather than dimples indicative of ductile rupture (15). Also, the results of Lewis (2) indicating high sulfur concentrations on grain boundary facets were found on a specimen tested at low temperature. Fracture occurred in the weld zone in this case since the specimen was notched to induce fracture. Since fracture at low temperatures occurs in the base metal rather than weld zone for unnotched specimens, it is doubtful that sulfur was the cause of the fracture.

The appearance of shallow ductile dimples on the faceted regions of Gleeble specimen fracture surfaces indicates the possibility of strain localization in the grain boundary regions. Strain localization could result from rapid microstructural changes which occur during high temperature exposure. These changes could include the formation of specific alpha phase morphologies together with the effects of grain size and shape and phases present. These metallurgical variables will be investigated individually in the following sections.

Alpha Phase Morphology. The effect of alpha phase morphology on high temperature ductility can clearly be shown by comparison of the Widmanstatten + grain boundary alpha microstructure with that of an equiaxed alpha structure

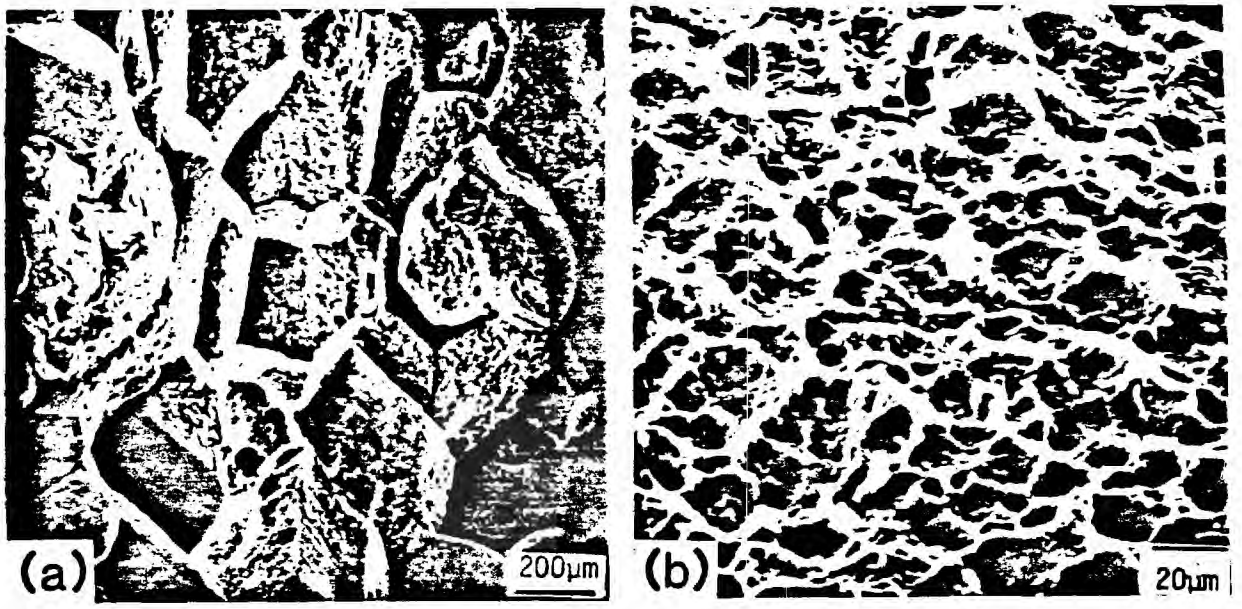

Figure 12. Scanning electron micrographs of Gleeble specimen fracture surface tested at 800°C after 30 minutes hold time.

formed by processing in the alpha + beta phase field. Hot rolling in the two phase field followed by annealing in the two phase field results in recrystallization of the alpha phase in the form of equiaxed grains. The beta phase is located at alpha grain triple junctions. The microstructure of this equiaxed alpha condition is illustrated in Figure 13a. The equiaxed alpha microstructure shows extremely high ductility at 800°C with almost 200% elongation. The absence of grain boundary alpha in this case eliminates a potential cause of strain localization in the grain boundary regions. Comparison of the equiaxed alpha structure behavior with that of the Gleeble specimens in Figure 13b shows that the drastic effect of alpha phase morphology on elevated temperature ductility. Thus it appears that temperature excursions above the beta transus which result in the formation of Widmanstatten type microstructures is critical to producing low ductility behavior. Subsequent investigation will examine the effects of structural variables such as beta grain size and shape, and the effect of transforming the beta phase to introduce new phases into the structure on low ductility behavior in Widmanstatten structures. Heat treatments and tensile properties are summarized in Table III. The goal of these tests is to reproduce the fracture behavior of the Gleeble specimens as evidenced by intergranular fracture with low ductility within the temperature range of the ductility dip. Reproduction of this low ductility behavior by laboratory heat treatment would show that the mechanisms responsible for low hot ductility are microstructure controlled rather than the result of rapid thermal cycling.

Prior Beta Grain Shape. Heat treatment W-2 produces the Widmanstatten + grain boundary alpha microstructure typical of specimens air cooled from above the beta transus. This structure has equiaxed prior beta grains due to recrystallization above the beta transus. The microstructure is identical to that

Table III. Summary of Tensile Properties

Condition	Test Temperature	Y.S.(MPa)	U.T.S.(MPa)	%Elong.	%R.A.
W-1.....	Room Temperature	690	786	15.4	20
	500°C	396	400	8.9	24
	800°C	94	104	16.0	62
W-2.....	Room Temperature	750	844	12.8	28
	500°C	372	463	6.7	23
	800°C	121	135	19.8	22
W-3.....	Room Temperature	-	-	-	-
	500°C	-	-	-	-
	800°C	-	-	-	-
W-4.....	Room Temperature	666	841	12.7	28
	500°C	403	528	12.0	27
	800°C	103	120	51.5	45
W-5.....	Room Temperature	810	903	14.0	22
	500°C	335	517	7.0	23
	800°C	105	132	18.0	22
W-6.....	Room Temperature	-	-	-	-
	500°C	-	-	-	-
	800°C	134	154	2.5	21
G-1.....	Room Temperature	700	795	14.0	18
	500°C	393	428	5.0	24
	800°C	95	105	15.0	17
E-1.....	Room Temperature	-	-	-	-
	600°C	-	-	42.0	40
	800°C	-	-	195.0	-

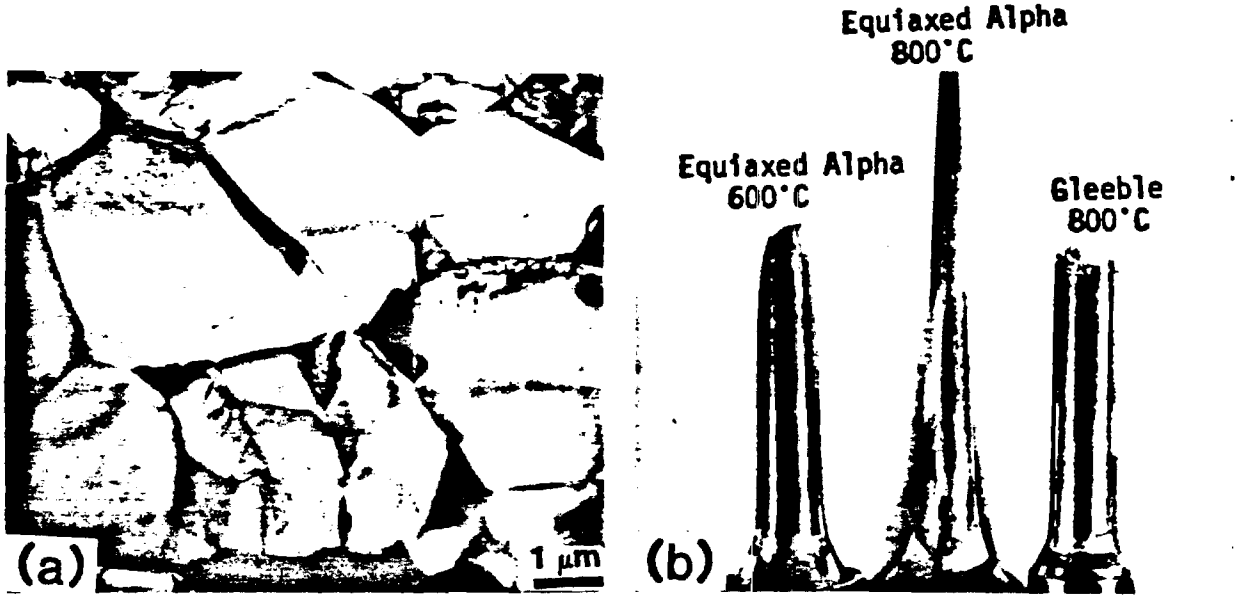

Figure 13. The effect of alpha phase morphology on hot ductility: (a) TEM illustrating equiaxed alpha microstructure; (b) macrophoto illustrating effect of microstructure on ductility.

of the beta processed plate (condition W-1) with respect to the phases present and phase morphologies. However, the beta processed plate has elongated beta grains due to working above the beta transus, while the beta annealed condition W-2 has equiaxed beta grains. By comparison of the hot ductility behavior of these two conditions, the effects of beta grain shape can be determined.

Although the microstructures of conditions W-1 and W-2 are similar, recrystallization changes the nature of deformation. The optical micrograph of Figure 14a shows slip features on the surface of a tensile specimen of condition W-2 strained 4% at room temperature. In this case slip is continuous across several platelet colonies terminating at the beta grain boundaries. This results in crack initiation by void formation along the beta grain boundaries, as shown in Figure 14b. Starke and co-workers (16) have suggested that this continuous deformation through the entire beta grain could be a platelet colony size effect. However, platelet colonies in condition W-2 are roughly half the size of those in the beta processed plate. If colony size were the critical factor, it might be expected that the structure with the largest colonies would show continuous deformation from colony to colony due to the increased slip length. The longer slip length in the large colonies would result in greater slip concentration at the colony boundaries which could activate slip in the adjacent colony. It is possible that this result is due to a texture effect produced by working in the beta phase region. The larger platelet colonies in condition W-1 may be explained by the effect of cooling rate on nucleation of the alpha phase. While both conditions W-1 and W-2 were produced by air cooling from above the beta transus, the cooling rate of the one-inch thick plate

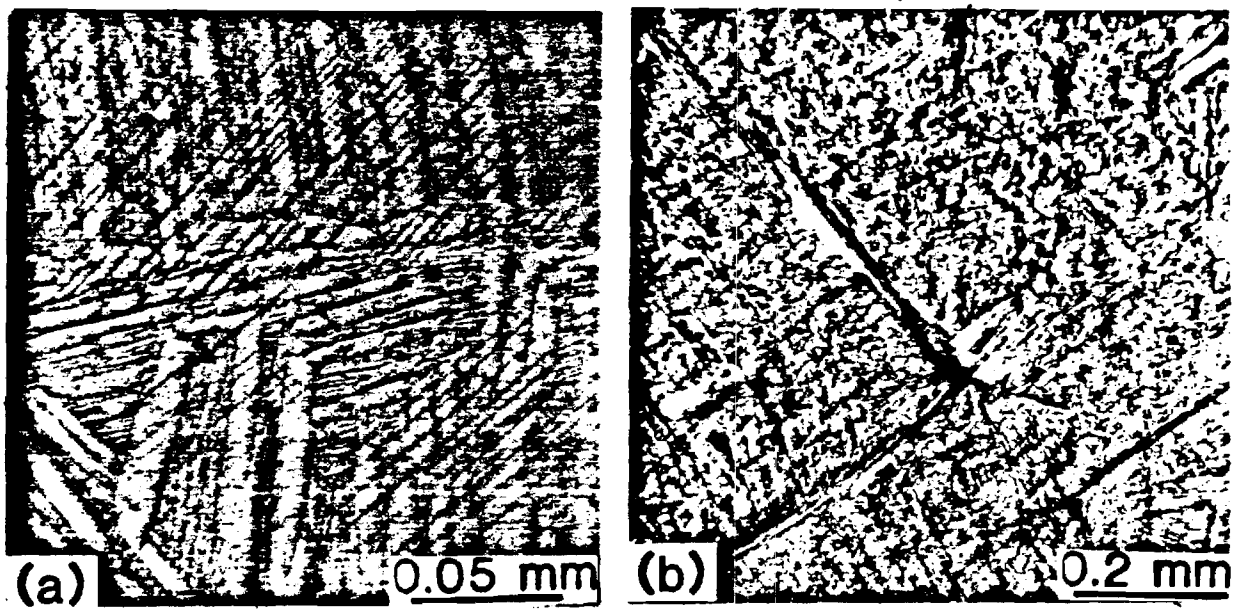

Figure 14. Optical micrographs showing deformation on the surface of a tensile specimen for condition W-2: (a) continuous slip across colony boundaries; (b) crack initiation along prior-beta grain boundary.

would be slower than that of a laboratory specimen used to produce condition W-2. This slower cooling rate lowers the nucleation rate of the alpha phase, resulting in larger platelets and thus larger platelet colonies.

While the microstructures are similar, condition W-2 shows quite different tensile properties and fracture behavior from that of condition W-1. Figure 15 shows the fracture features of condition W-2 specimens tested at room temperature, 500°C and 800°C. Fracture in the equiaxed structure is characterized by the appearance of facets on the fracture surface. These facets correspond to the beta grains in size, and result from stress concentration along the beta grain boundaries. Intergranular crack initiation followed by transgranular propagation produces the fracture appearance of room temperature specimens shown in Figure 15a. With increasing temperature, a transition in fracture mode from predominantly transgranular to completely intergranular is observed. At the 800°C test temperature, condition W-2 fails intergranularly along beta grain boundaries, as illustrated in figure 15c. High magnification shows shallow ductile dimples on the grain facets similar to those found on Gleeble specimen fracture surfaces.

Since condition W-2 shows intergranular fracture at 800°C while W-1 does not, it is important at this point to determine the role of the continuous intragranular deformation within the beta grains in producing the intergranular fracture. Slip continuous through the beta grains terminating at the grain boundaries could result in severe stress concentration along those boundaries and play a key role in producing the observed intergranular fracture. The importance of this intragranular component of deformation may be determined by use of a duplex heat treatment designed to first produce the W-2 microstructure, and then a second step to transform the beta phase between alpha

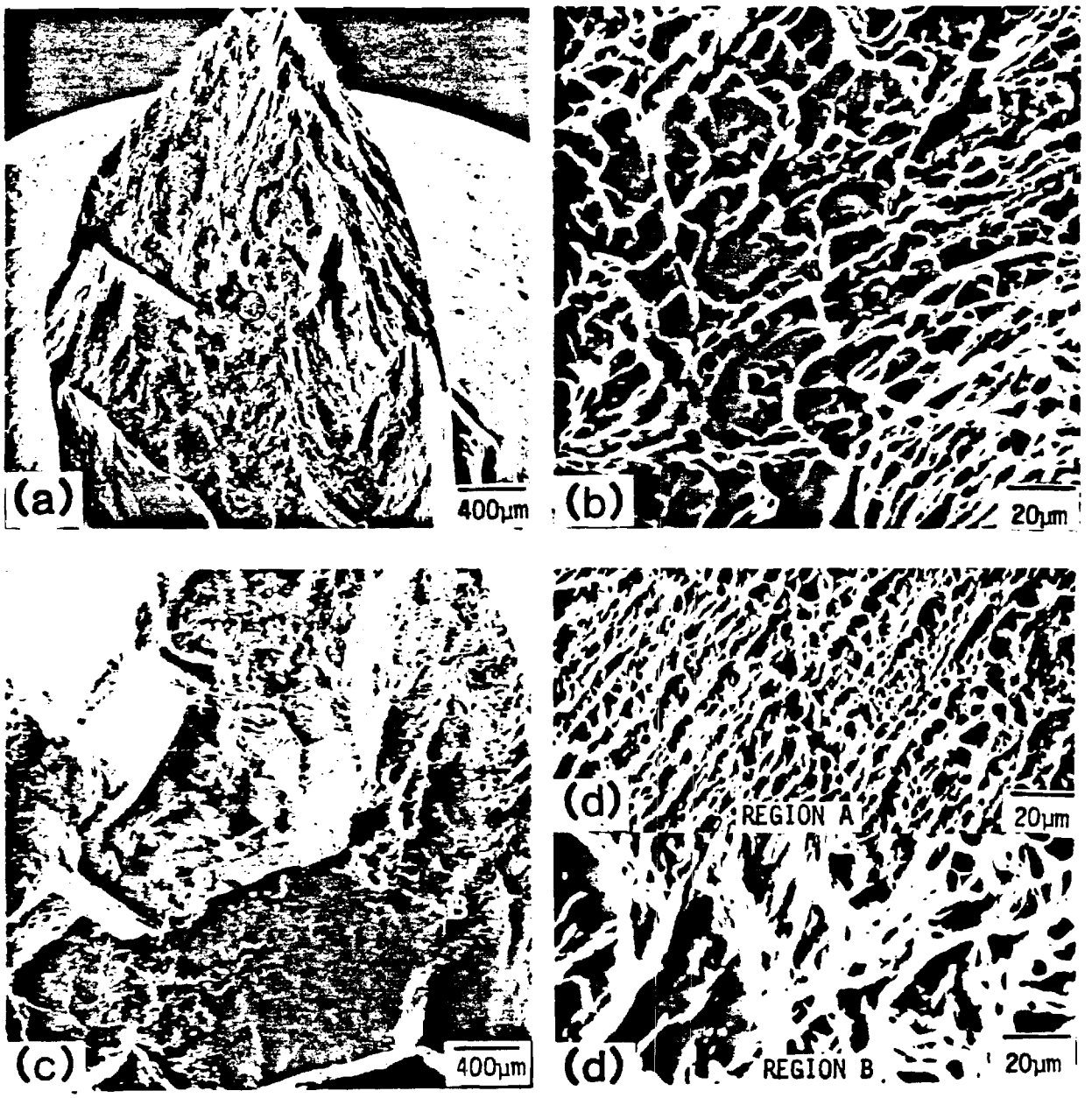

Figure 15. Scanning electron micrographs of tensile specimen fracture surfaces for condition W-2: (a), (b) room temperature; (c), (d) 500°C; and (e), (f) 800°C.

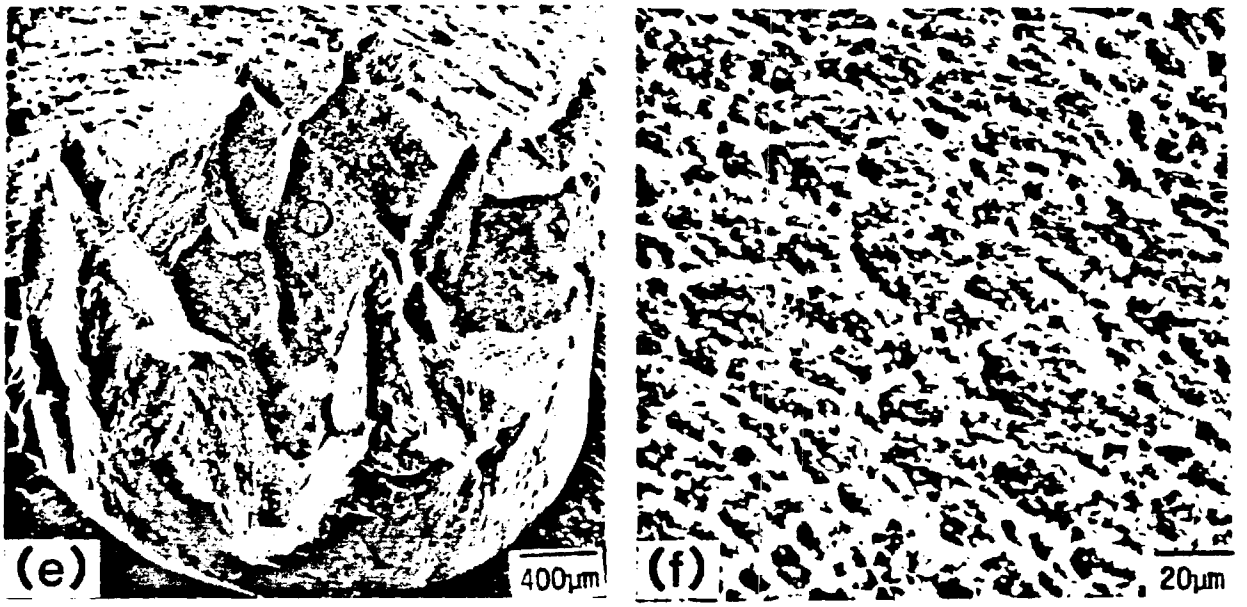

Figure 15. Continued.

platelets to martensite by heating to a temperature high in the alpha + beta phase field and quenching. This heat treatment does not change beta grain size or shape, or the alpha phase morphology. The martensite phase acts as a barrier to slip, as shown in the transmission electron micrographs of Figure 16. This reduces the slip length from the diameter of a beta grain to the width of a single alpha platelet and prevents stress concentration along the beta grain boundaires due to intragranular deformation. Thus, if intragranular deformation is critical to themechanism of intergranular fracture, this condition would not exhibit this type of fracture. This heat treatment was used to produce condition W-3. Specimens in this condition show intergranular fracture at 800°C virtually identical to that of condition W-2, as shown in Figure 17. This result indicates that stress concentration along the beta grain boundaries due to slip continuous within the beta grains is not critical to the intergranular fracture mechanism, and that the grain shape is more important in producing strain localization in the grain boundary regions.

Deformation within the grain boundary alpha phase for condition W-2 tested at 800°C is shown in the transmission electron micrographs of Figure 18. Planar slip within the grain boundary alpha is seen to be coplanar with slip in the alpha platelets in the grain to the right side of the grain boundary, but not in the grain to the left. This indicates that the grain boundary alpha obeys the Burgers precipitate orientation relationship with the grain on the right, but not on the left. Grain boundary alpha generally forms only in one grain on one side of the grain boundary, and thus obeys the orientation relation with that grain. Thus, $(0001)\{11\bar{2}0\}_\alpha$ slip originating in the grain boundary alpha results in no stress concentration at the grain boundary alpha interface on the right side since the deformation can continue into the interior of the grain by coplanar $(0001)\{11\bar{2}0\}_\alpha$ and $(110)\langle 111\rangle_\beta$ slip. However, slip terminating at the left side of the grain boundary alpha at the prior beta grain boundary can result in void formation and produce intergranular fracture.

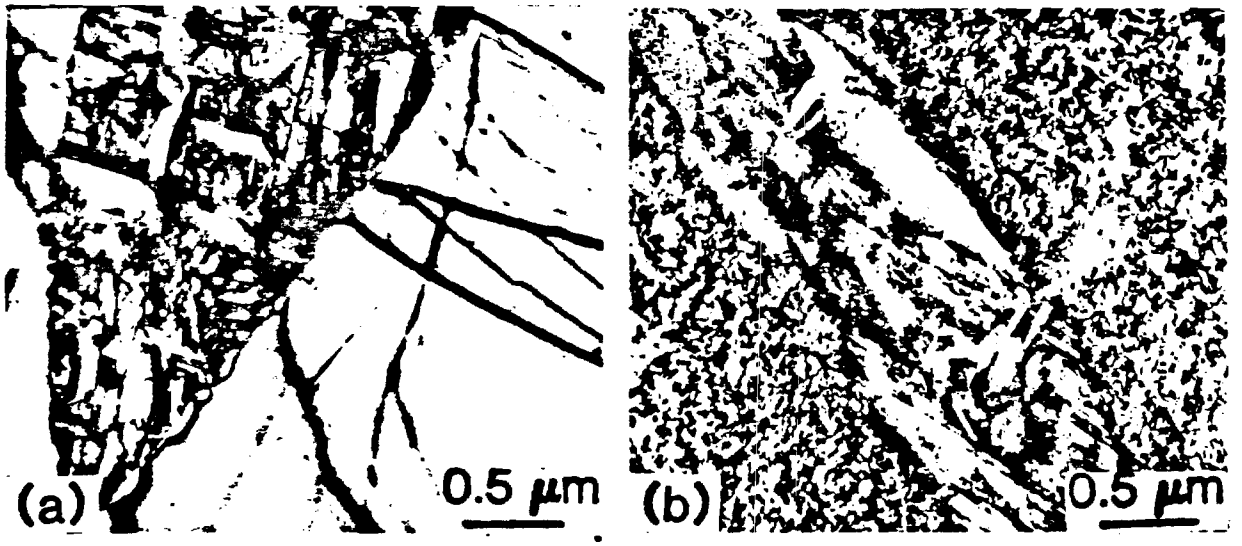

Figure 16. Effect of transformed beta on deformation: (a) TEM of transformed beta microstructure; (b) transformed beta acting as a barrier to slip.

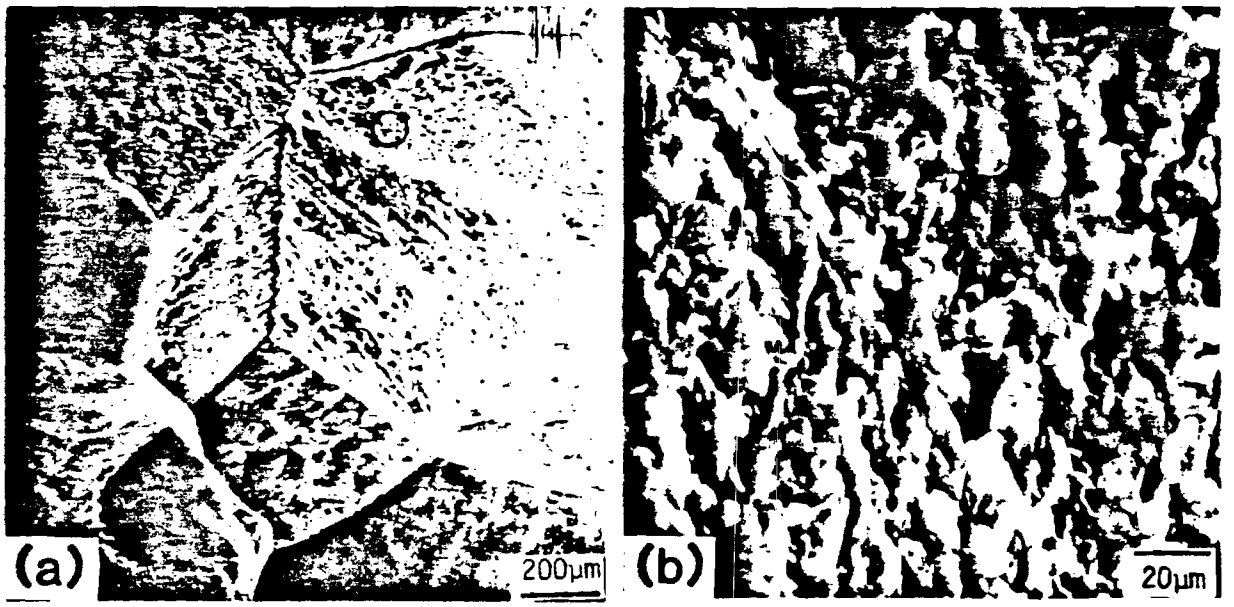

Figure 17. Scanning electron micrographs for condition W-3 specimen tested at 800°C.

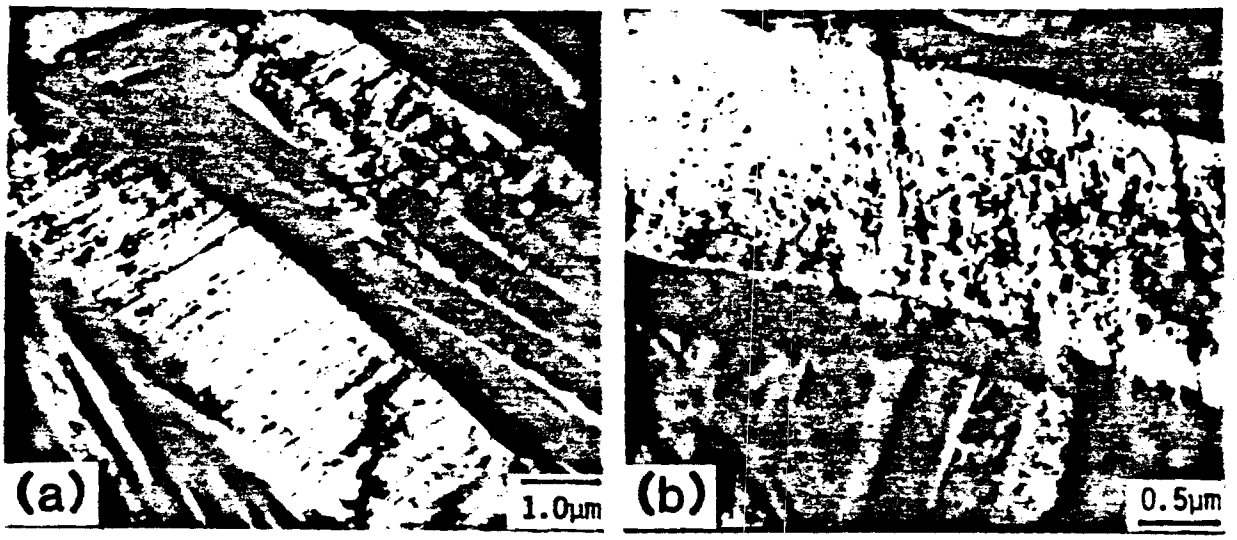

Figure 18. Transmission electron micrographs showing deformation within the grain boundary alpha phase for condition W-2 specimen tested at 800°C.

The grain boundary facets would reveal shallow dimples indicative of the void formation mechanism. The model for this intergranular fracture mechanism is illustrated schematically in Figure 19. The fact that completely intergranular fracture does not occur until the higher test temperature is reached may be explained by the effect of temperature on deformation. Strain localization is very sensitive to differences in flow stress. At low temperatures, the difference in flow stress between grain boundary alpha and the Widmanstatten alpha + beta structure within the grains may not be large enough to produce significant strain localization for completely intergranular fracture. Also, dislocation pileups at the beta grain boundary due to slip in the grain boundary alpha may create a back stress which cannot be overcome until the higher temperature is reached. Thus the back stress would act to harden the grain boundary alpha phase and reduce the difference in flow stress. These factors would combine to produce the mixed fracture mode shown by condition W-2 at the lower test temperatures. In the absence of significant grain boundary alpha deformation, fracture would be controlled by deformation within the grains. This effect of strain localization is similar to that found in age hardened aluminum alloys due to heterogeneous precipitation at grain boundaries (17). In many cases, this results in the formation of solute-depleted precipitate free zones (PFZ) adjacent to the grain boundaries. This zone is weaker than the matrix and can be the site of preferential deformation. The localized strain leads to stress concentration at grain boundary triple junctions and early crack initiation with lower ductility. This mechanism of void formation along the grain boundary alpha-beta grain boundary interface is similar to that found by Greenfield and Margolin (18-20) in the Ti-5.25Al-5.5V-0.9Fe-0.5Cu alloy, although this alloy showed intergranular fracture at room temperature.

It is interesting at this point to consider why condition W-1 which also has grain boundary alpha, does not show intergranular fracture similar to that of condition W-2. With the beta grains being elongated due to previous working

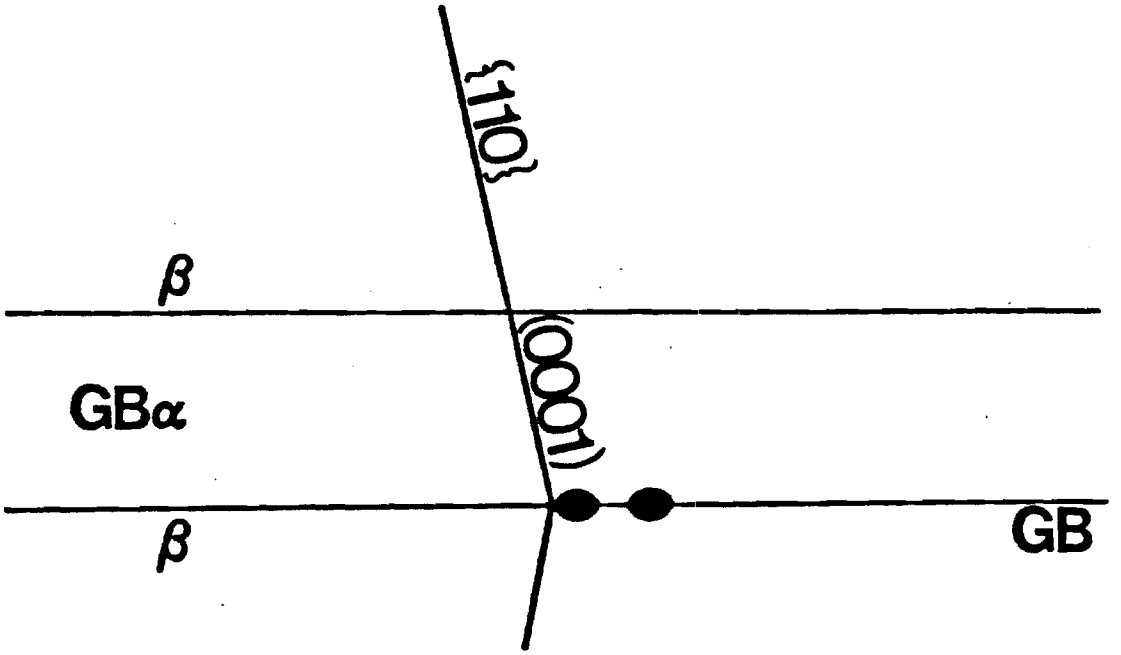

Figure 19. Model of void formation and fracture for condition W-2.

in the beta phase field, most of the grain boundary alpha will be oriented in only one way with respect to the tensile axis. With slip occurring on only a single slip system, the resolved shear stress will be very small for specimens tested with the working direction parallel to the stress axis. This is illustrated schematically in Figure 20. Thus, slip within the grain boundary alpha will be limited for condition W-1, and the deformation within the grains will control the fracture process. In this case, slip terminating at platelet colony boundaries results in void formation at those boundaries, and thus fracture occurs along platelet colony boundaries rather than beta grain boundaries. However, there are some areas on the fracture surface of condition W-1 specimens tested at 800°C which appear to represent fracture around the ends of the elongated grains where the grain boundary alpha phase would be more favorably oriented for slip. This gives the appearance of "fingers" sticking up on the fracture surface, as shown in Figure 8c. This behavior is contrasted with that of condition W-2 with equiaxed beta grains. In this case most of the grain boundary alpha will be oriented favorably for slip, and sufficient intergranular deformation will occur to produce intergranular fracture at 800°C. Thus, the shape of the prior beta grains is a critical factor in producing intergranular fracture with resultant low ductility for Widmanstatten + grain boundary alpha phase morphologies. Temperature excursions above the beta transus will be required to produce the equiaxed beta grains.

Phases. The effects of phases present in the microstructure on hot ductility can be examined by utilizing heat treatments designed to transform the beta phase to martensite. These heat treatments may be used to produce transformed beta phase in Widmanstatten + grain boundary alpha microstructures or to produce fully martensitic structures.

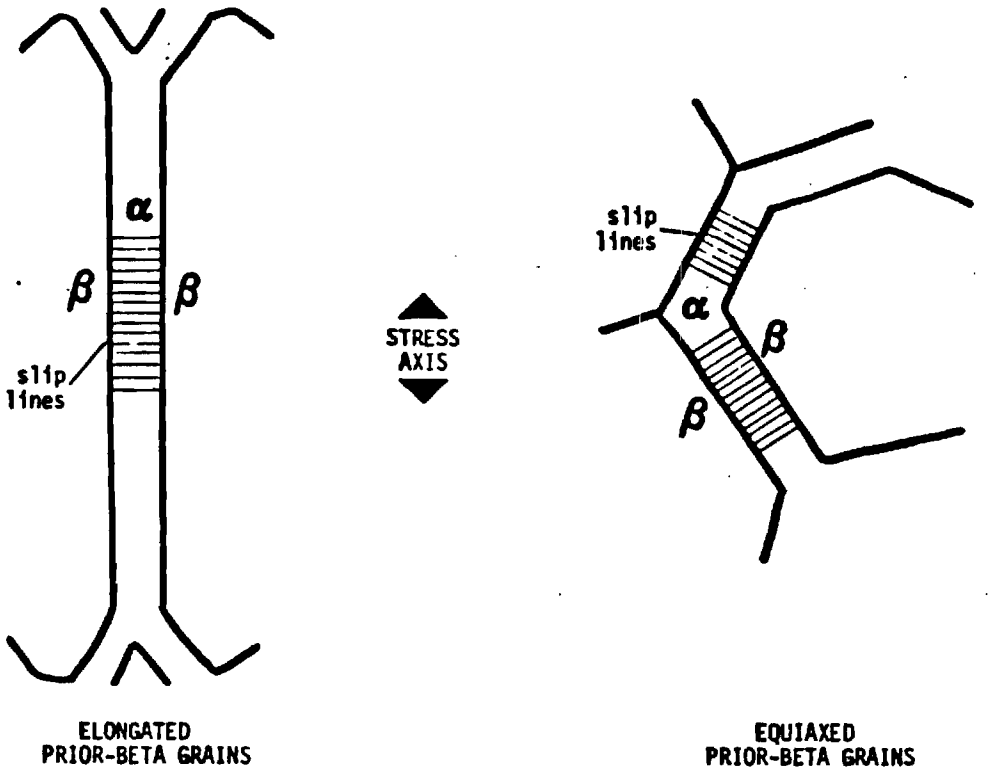

Figure 20. Effect of beta grain shape on orientation of grain boundary alpha phase and deformation within the grain boundary alpha layer.

By annealing Widmanstatten + grain boundary alpha structures at a temperature high in the alpha + beta phase field above the M_s temperature and quenching, the beta phase will be transformed to martensite without altering either the alpha phase morphology or the beta grain size and shape. Thus any differences in hot ductility behavior may be attributed to the presence of the transformed beta phase. Heat treatment W-3, which has been previously discussed, and W-4 are designed to produce transformed beta microstructures in equiaxed and elongated beta grain structures, respectively. In both cases, the alpha phase is present in the Widmanstatten + grain boundary alpha phase morphology. It has already been shown that for the equiaxed case the transformed beta phase has no effect on fracture behavior. Condition W-3 shows intergranular fracture similar to that of condition W-2, as shown in Figure 17. Thus, it appears that for the equiaxed case, the presence of transformed beta phase has no effect on fracture behavior.

Fracture behavior for condition W-4 tensile specimens tested at room temperature, 500°C, and 800°C is illustrated in the scanning electron micrographs of Figure 21. The transformed beta phase is seen to have no adverse effect on ductility, with reduction in area increasing from 28% at room temperature to 45% at 800°C. There is some increase in strength over condition W-1 due to the effect of interplatelet martensite to act as a barrier to slip, but this increased strength does not result in a significant loss of ductility. As was the case for Widmanstatten + grain boundary alpha + beta microstructures in

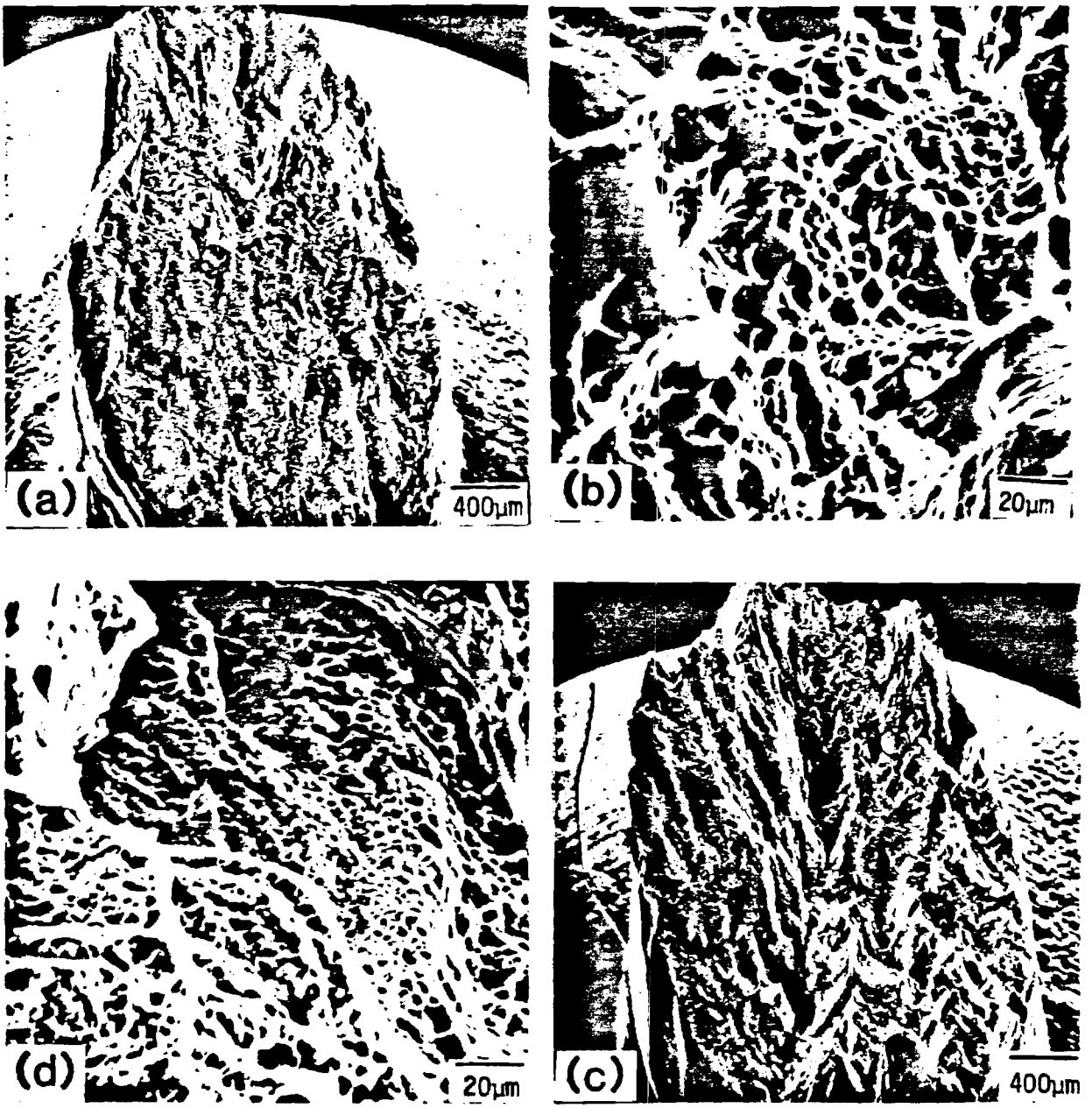

Figure 21. Scanning electron micrographs showing fracture features of condition W-4 specimens tested at: (a), (b) room temperature; (c), (d) 500°C; and (e), (f) 800°C.

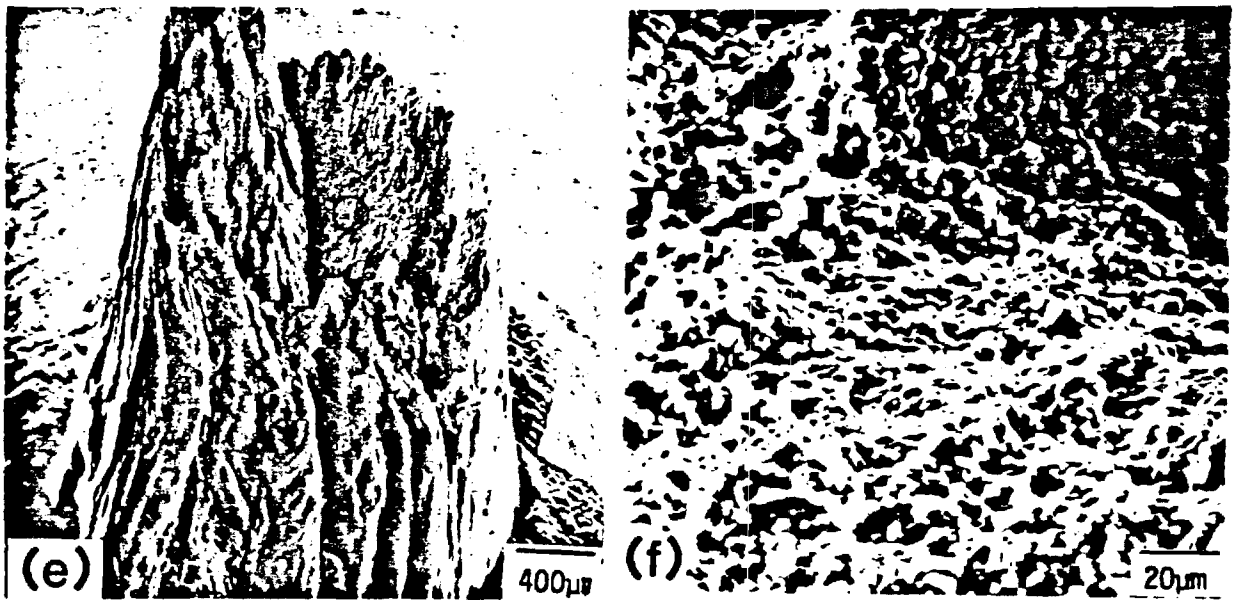

Figure 21. Continued.

conditions W-1 and W-2, the prior beta grain shape is the controlling factor in fracture behavior. Transforming the beta phase in condition W-1 does not induce intergranular fracture where it has not previously been found, and the transformed beta phase does not prevent intergranular fracture found in condition W-2. Thus, the microstructural features controlling the fracture behavior in Widmanstatten + grain goundary alpha structures are unchanged by altering the phases present in the microstructure.

Specimens which have been quenched from above the beta transus form fully martensitic microstructures with equiaxed beta grains as shown in the optical micrographs of Figure 22. Tensile specimens which have fully martensitic structures (condition W-5) exhibit similar fracture behavior to that of condition W-2, producing completely intergranular fracture at 800°C, as shown in Figure 23. In this condition, the deformation within the grains is somewhat different from the air cooled conditions due to the random plate orientations of the martensite phase. The transmission electron micrograph of Figure 24 shows planar slip within martensite plates. In order for deformation to continue from one plate to the next, it must change directions. While there is not a large difference in flow stress between the Widmanstatten + grain boundary alpha structure and the martensitic structure, the martensite has a higher strength due to the more tortuous slip path. Failure in the martensite specimens tested at 800°C occurs by void formation along the prior beta grain boundaries, as illustrated in the optical micrographs of Figure 25. This mechanism produces the intergranular fracture which reveals shallow dimples on the grain facets as shown in Figure 23c. Since no grain boundary alpha phase is expected to be present in the as-quenched martensite, the fracture model shown in Figure 19 for the Widmanstatten + grain boundary alpha structure does not apply. However, at the higher test temperature, sections taken through failed specimens indicate that grain boundary allotriomorphs have formed as a result of the high temperature exposure of the

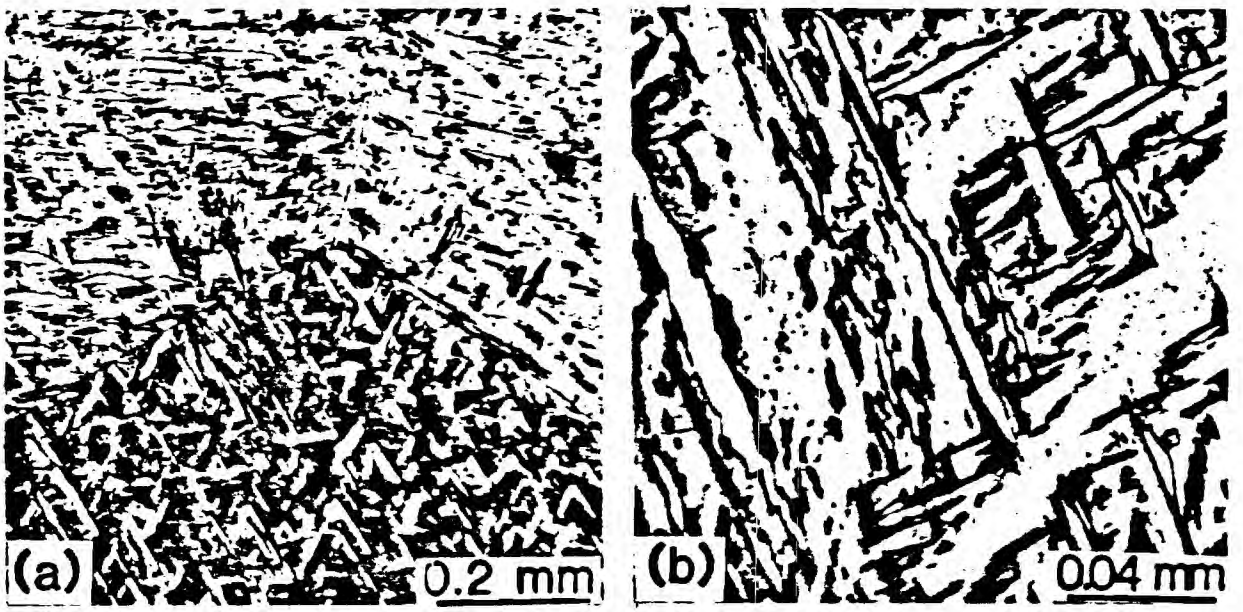

Figure 22. Optical micrographs of martensitic microstructure of condition W-5.

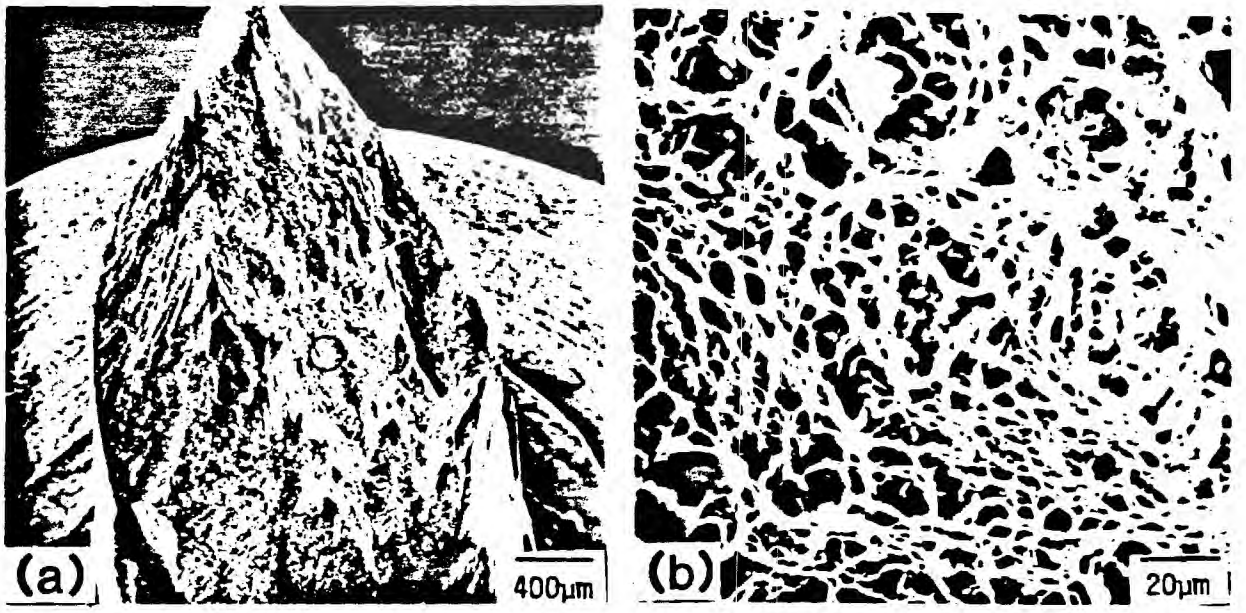

Figure 23. Scanning electron micrographs showing fracture features of condition W-5 specimens tested at : (a), (b) room temperature; (c), (d) 500°C; and (e), (f) 800°c.

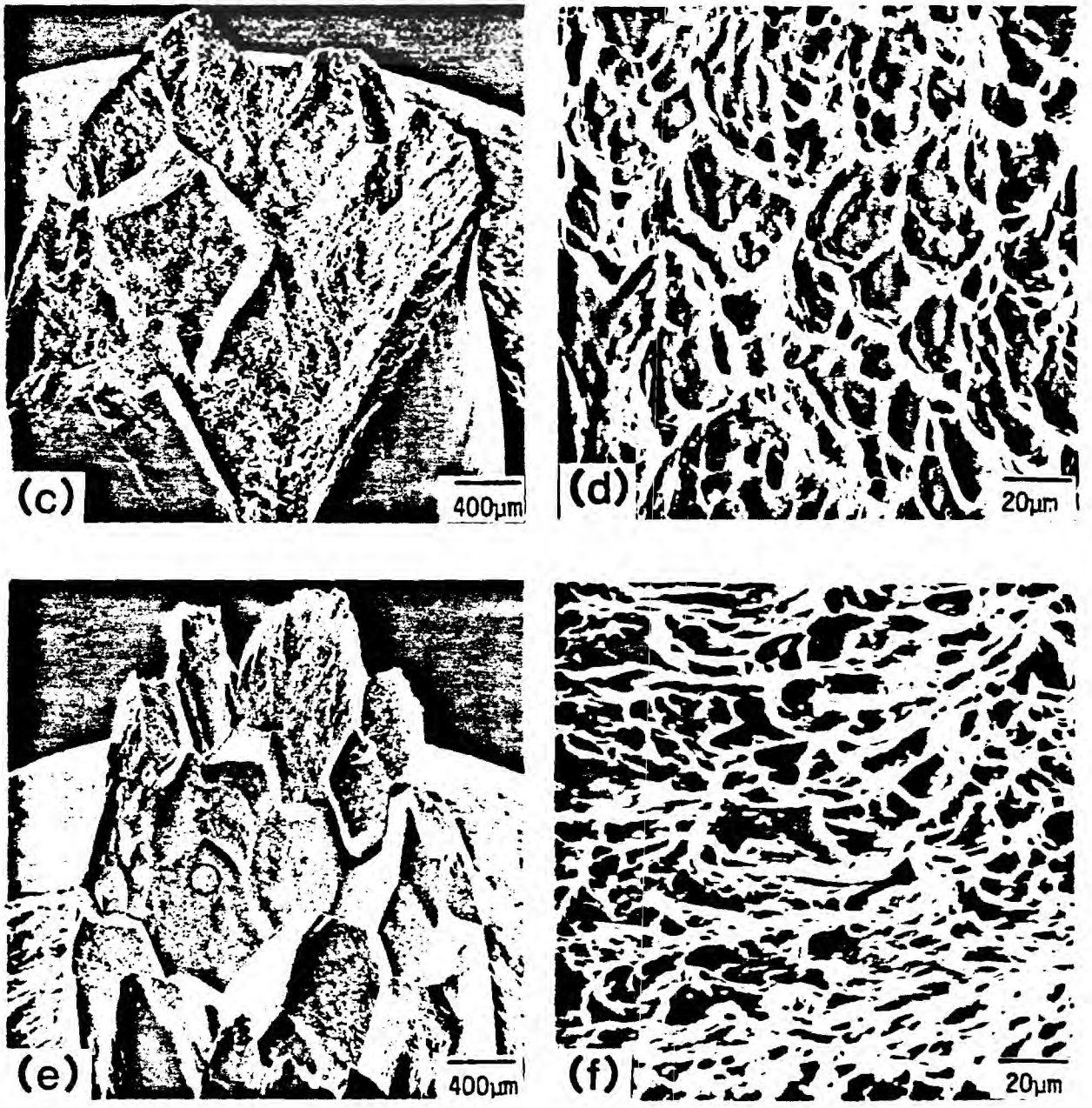

Figure 23. Continued.

Figure 24. Transmission electron micrograph illustrating deformation in condition W-5.

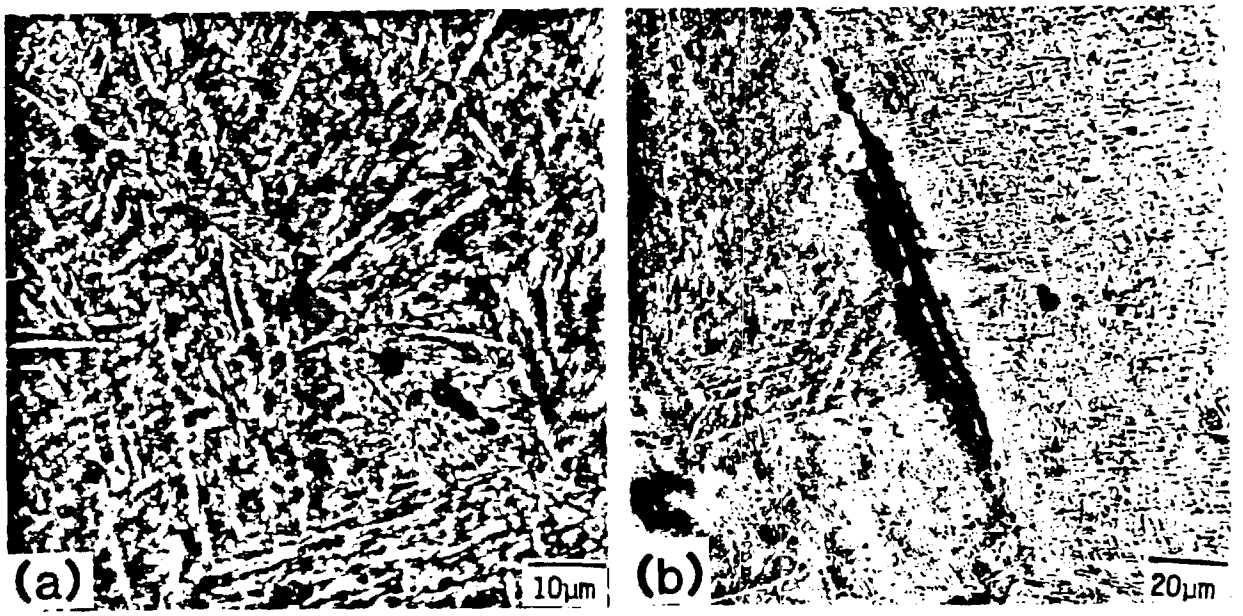

Figure 25. Optical micrographs illustrating void formation along prior-beta grain boundaries: (a) voids along beta grain boundary, (b) crack formation due to void coalescence.

test. At the 800°C test temperature, the driving force for decomposition of the metastable martensite phase will be great. However, at temperatures high in the alpha + beta phase field, the driving force for alpha phase formation will be low, and thus any alpha which forms will do so heterogeneously along the beta grain boundaries. Figure 26 illustrates formation of grain boundary alpha particles, the intergranular fracture model would apply with one modification. In this case, the grain boundary alpha phase would have no orientation relationship with the matrix on either side of the particles since they formed from martensite rather than beta. Thus voids could form anywhere along the alpha/martensite interface due to deformation within the grain boundary alpha particles. Strain localization in the grain boundary alpha particles would be more intense than for the case of condition W-2, since the difference in strength between the intergranular alpha and the intragranular martensite would be greater than the difference between grain boundary alpha and intragranular alpha + beta in condition W-2. Thus martensite specimens will fail intergranularly at 800°C with even less ductility than that shown for air cooled specimens.

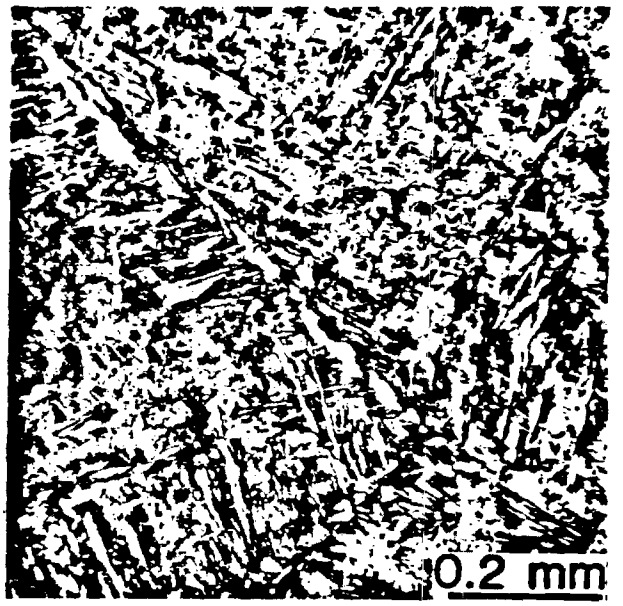

Figure 26. Optical micrograph of condition W-5 tensile specimen tested at 800°C illustrating grain boundary alpha formation.

In addition to the formation of grain boundary alpha at 800°C, the martensite phase also ages by formation of beta precipitates heterogeneously along margensite plate boundaries. This is illustrated in the transmission electron micrographs of Figure 27. This aging response is normally found in hexagonal titanium martensite, and results in little age hardening since the average solute content of the matrix decreases resulting in softening of the matrix.

Thus for specimens quenched from above the beta transus to form martensititic structures rapid grain boundary alpha formation within the temperature range of the ductility dip is responsible for producing the intergranular type fracture with resultant low ductility at 800°C. The fact that this structure has equiaxed beta grains due to heating above the beta transus is also important,

Figure 27. Transmission electron micrographs illustrating the aging response of hexagonal titanium martensite.

since the equiaxed grains result in a grain boundary alpha orientation with respect to the stress axis which produces significant deformation in the grain boundary alpha phase. Thus, for condition W-5, the combined effects of rapid formation of equiaxed beta grains followed by rapid precipitation of alpha phase along beta grain boundaries results in the observed fracture behavior.

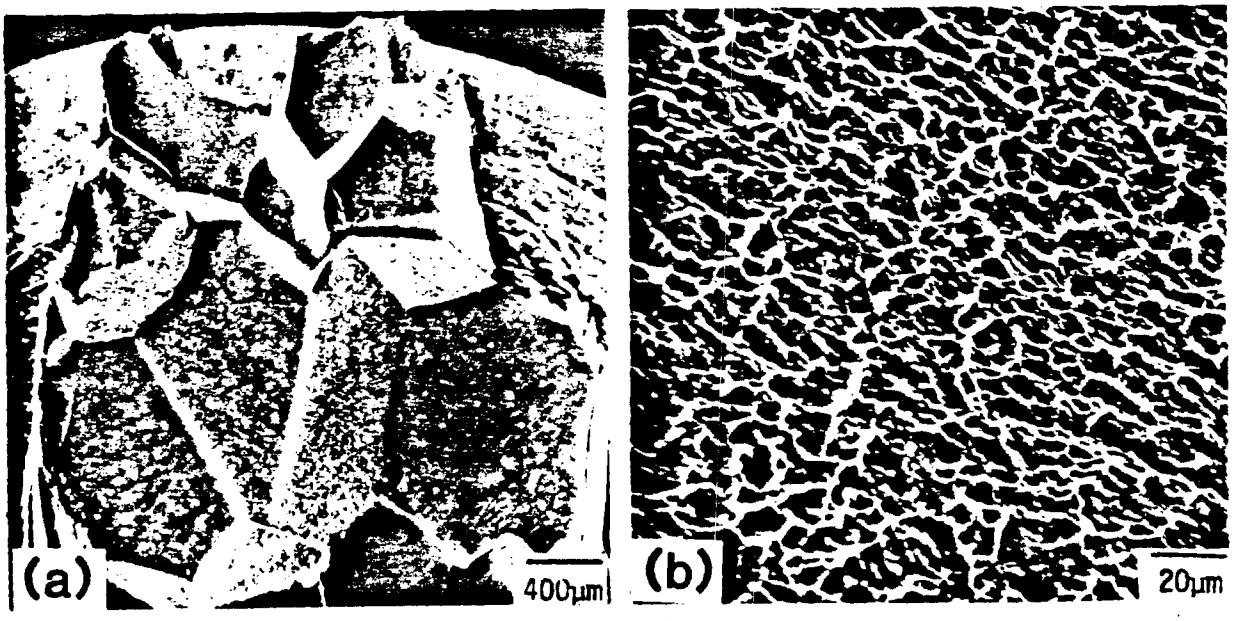

Figure 28. Scanning electron micrographs of condition W-6 tensile specimen tested at 800°C.

Increasing the beta grain size by longer annealing times above the beta transus has the effect of slightly decreasing the ductility at 800°C. This specimen shows intergranular fracture identical to that of condition W-5, as shown in Figure 28. The larger grain size may result in thicker grain boundary alpha, since the relative amount of alpha phase which may be expected to form at a given temperature will be constant. The less grain boundary area available for precipitation in the large grain size structure would require that the grain boundary alpha which formed would be thicker. Thicker grain boundary alpha would act to increase the slip length in the alpha and result in more intense stress concentration at the beta grain boundaries, producing fracture more rapidly than that found in smaller grain size specimens.

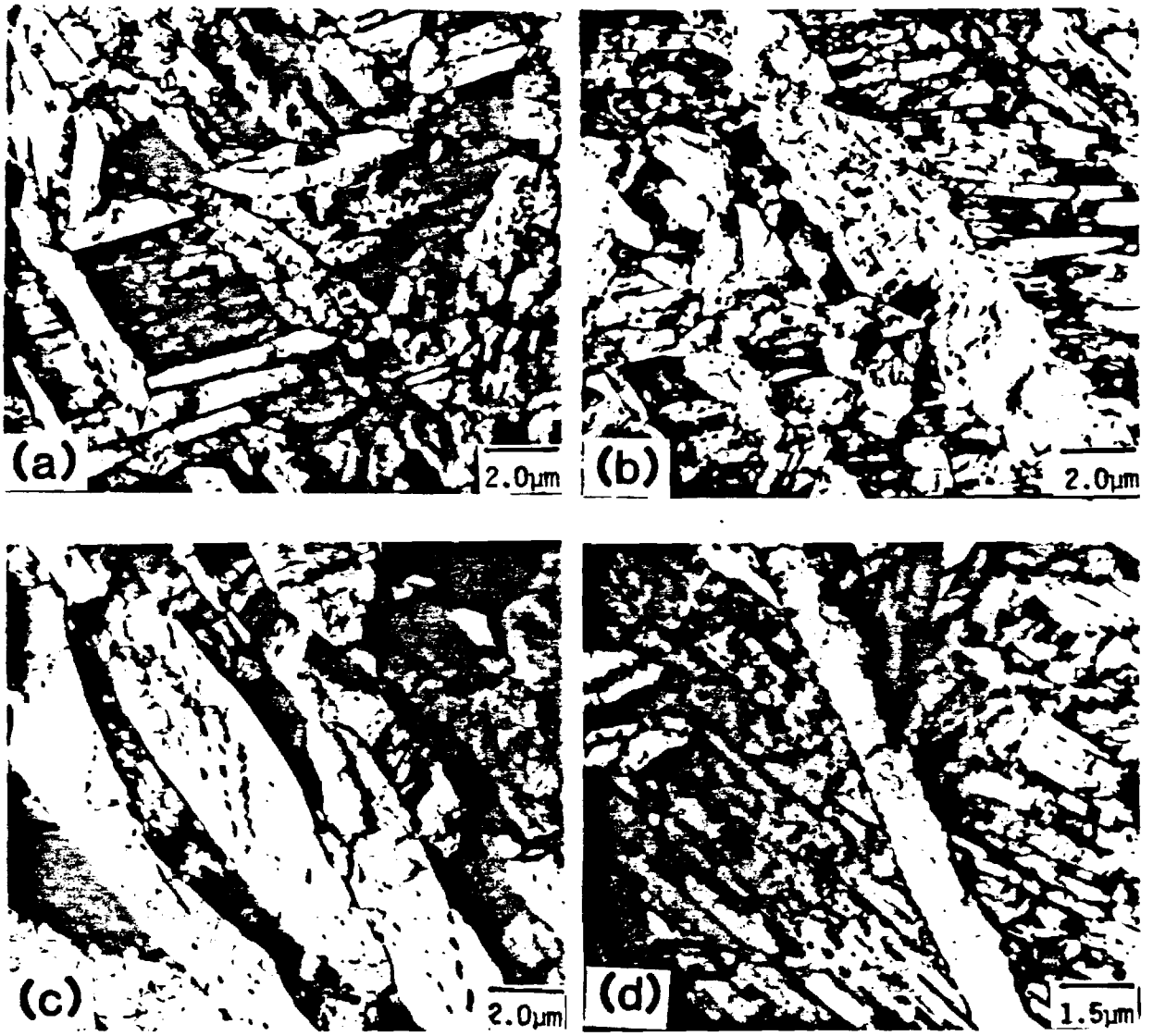

Figure 29. Transmission electron micrographs of Gleeble specimen tested at 800°C.

Finally, since Gleeble specimens which fail intergranularly at 800°C have microstructure similar to that of the quenched conditions W-5 and W-6, it is important to determine if rapid grain boundary alpha formation may also be involved in producing low ductility fracture in this condition. Since high temperature exposure is required to produce fracture in the weld zone of Gleeble specimens as previously discussed, it is suspected that rapid grain boundary alpha formation does occur. The transmission electron micrographs of Figure 29 show martensite plates similar to those found in quenched specimens. However, the plates are not as sharply formed, and have a lower dislocation density within the plates. There are basically two types of plates. Large massive martensite plates are surrounded by groups of smaller platelets. The micrographs also show evidence of beta precipitation similar to that found for quenched specimens tested at 800°C. This aging response is more clearly illustrated in the bright field/dark field transmission electron micrograph pair of Figure 30. Gleeble specimens also show evidence of grain boundary alpha formation. In some areas it appears to be a continuous film, while in others it appears as grain boundary allotriomorphs. The transmission electron micrograph of Figure 31 shows deformation within the grain boundary alpha particles in a specimen which was strained approximately 4% at 800°C. Thus, it appears that the mechanisms responsible for intergranular fracture in the Gleeble specimen at 800°C are similar to those of quenched specimens. Again, formation of equiaxed beta grains due to temperature excursion above the beta transus followed by the rapid formation of grain boundary alpha within the temperature range of the ductility dip produce strain localization within the grain boundary regions resulting in intergranular fracture and low ductility.

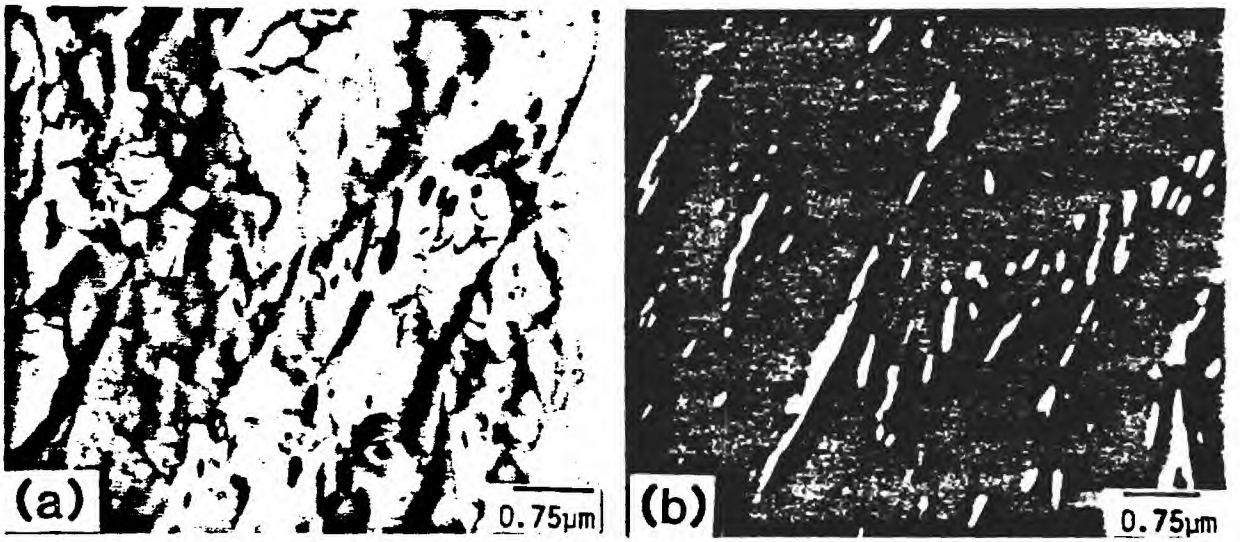

Figure 30. Transmission electron micrographs illustrating beta precipitation along martensite plate boundaries: (a) bright field; (b) dark field.

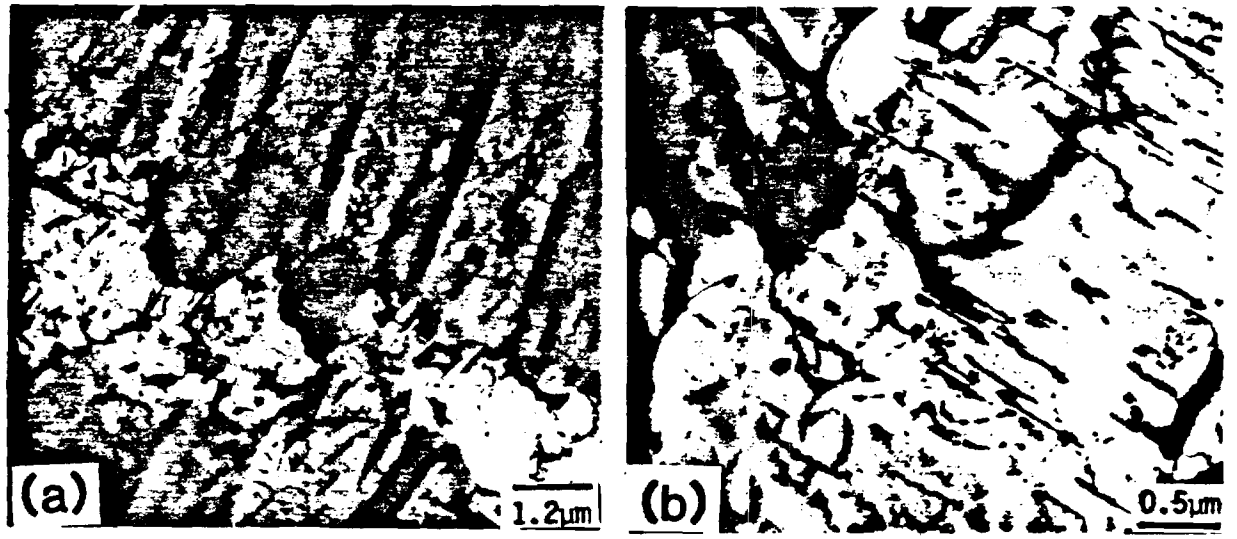

Figure 31. Transmission electron micrographs of grain boundary region of Gleeble specimen strained approximately 4% at 800°C: (a) grain boundary alpha particles formed at 800°C; (b) deformation within alpha phase.

Creep Behavior

Microstructures evaluated for creep behavior are illustrated in the optical micrographs of Figure 32. Tensile properties of these conditions are summarized in Table IV.

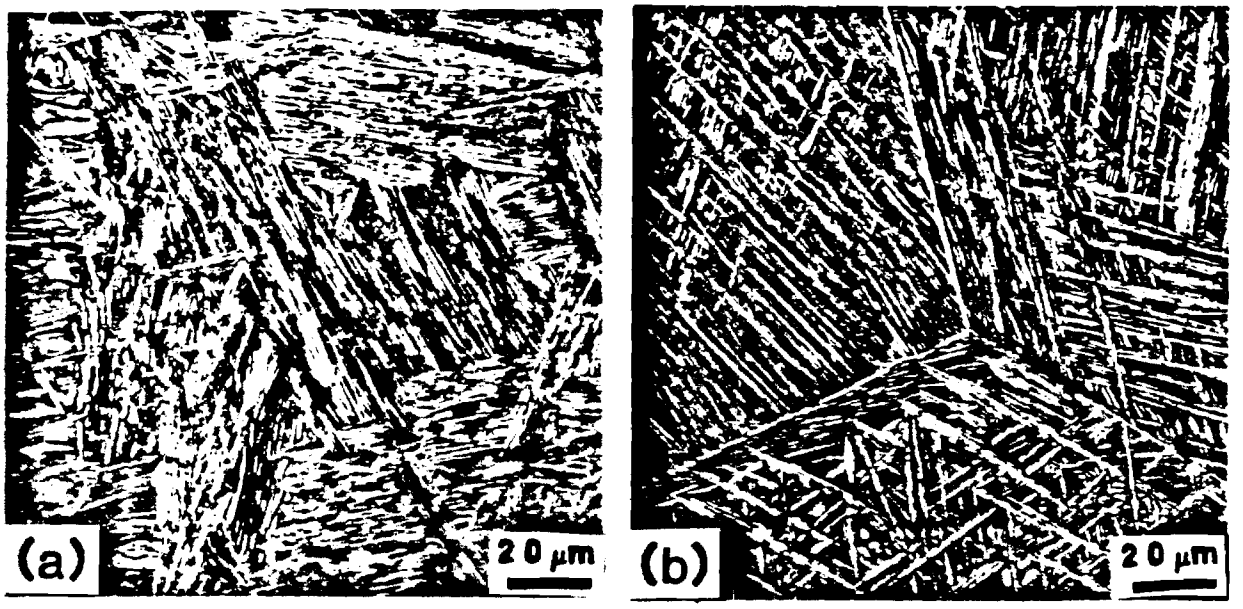

Figure 32. Optical micrographs illustrating the microstructures of the selected heat treatments: (a) W-1 (b) W-2 (c) W-3 (d) W-8 (e) W-9

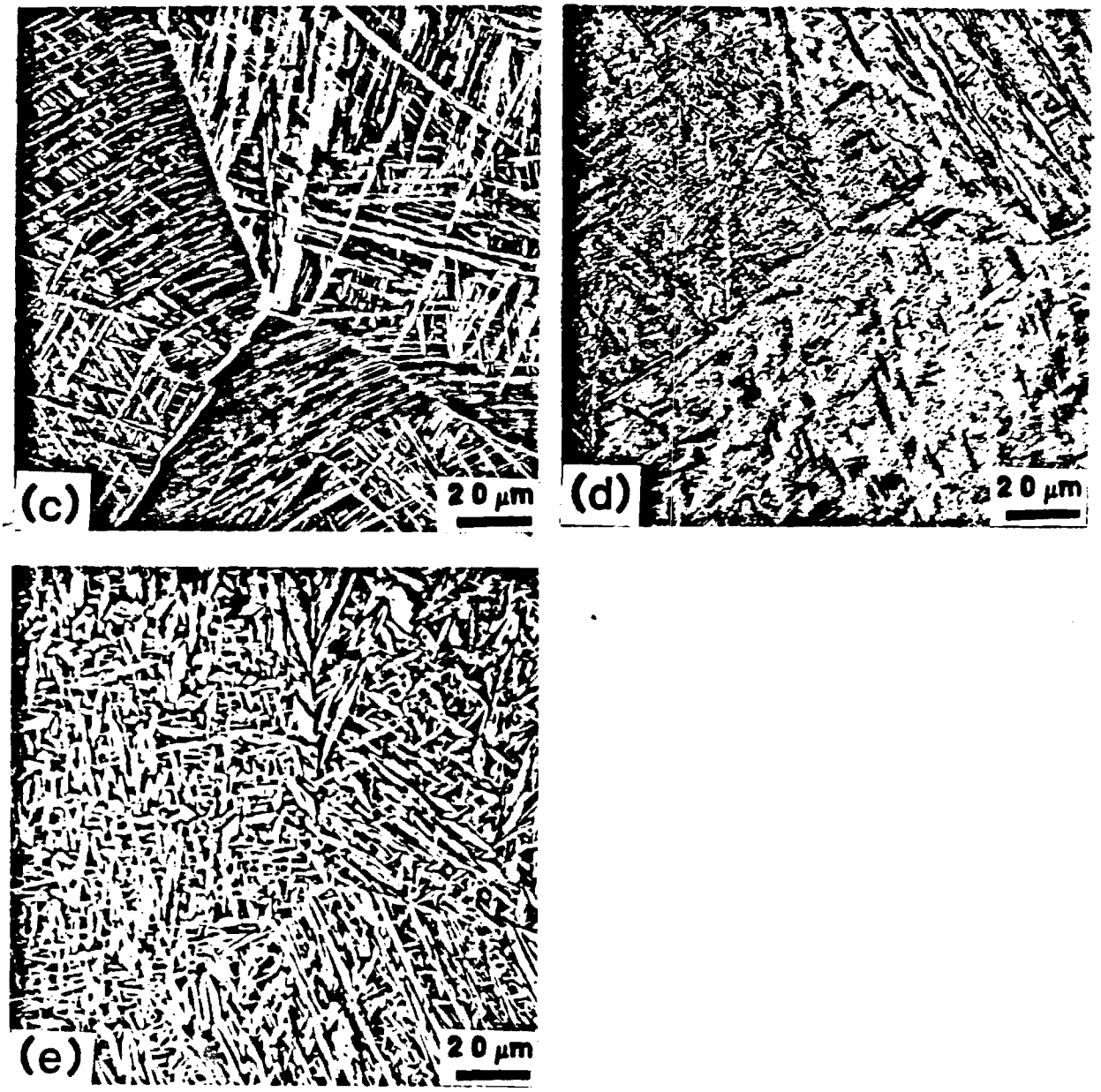

Figure 32. Continued.

TABLE IV. Tensile Properties of Selected Microstructures

Specimen Designation	Yield Stress (MPa)	UTS (MPa)	Elastic Limit (MPa)
W-1	760	864	592
W-2	796	895	616
W-3	751	885	629
W-8	757	915	553
W-9	784	884	619

Figure 33 shows creep curves for condition W-1 specimens at three stress levels (75%, 90% and 100% of the yield stress). The curves are typical of those previously observed for low temperature creep; i.e., creep was initially rapid and then decreased quickly at low stresses, or gradually at high stresses (33). Also, the creep curves appear to level off at a time which is dependent upon the applied stress. This kind of creep saturation (or creep exhaustion) is commonly observed at low temperatures. Thompson and Odegard (4) proposed that the activated process of low temperature creep is probably the overcoming of interstitial solute atoms, and that the exhaustion of the easiest dislocation sources at each stress level could be the reason for creep saturation. Extensive studies of dislocation structures after creep (5), and the investigation of prior straining effects on creep saturation, have provided evidence to support this explanation. Figure 34 shows creep curves for five different microstructures tested at the same stress level, 684 MPa, which is equal to 90% of the yield stress of the W-1 condition. It can be observed from this plot that creep strain varied for specimens with different heat treatments. Inman and Gilmore (1) have shown that creep in Ti-6Al-4V is sensitive to microstructural changes with the important variables being grain size, microchemistry, phase morphology, and preferred orientation. In the present study, phase morphology might be the primary factor affecting the differences in creep behavior. Generally, for creep at low temperatures, the creep strain/time relationship follows a power law (3,4); i.e., $\varepsilon = At^n$, where A is a constant depending on stress and material property, ε is creep strain (total strain minus elastic strain), t is the duration of creep, and n is the time exponent. Figure 35 shows an example of log ε-log t plot for specimen W-1 crept at 684 MPa. The time exponent can be estimated from the slope of the straight line and is given in Table V for each microstructure examined.

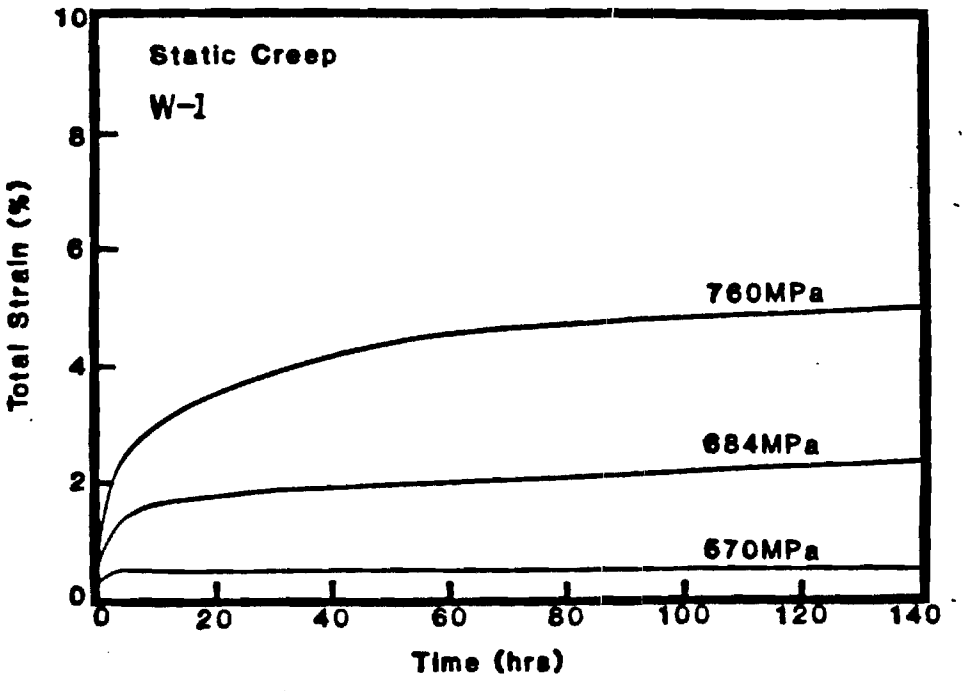

Figure 33. Static creep results for W-1 Ti-6211 at different stress levels.

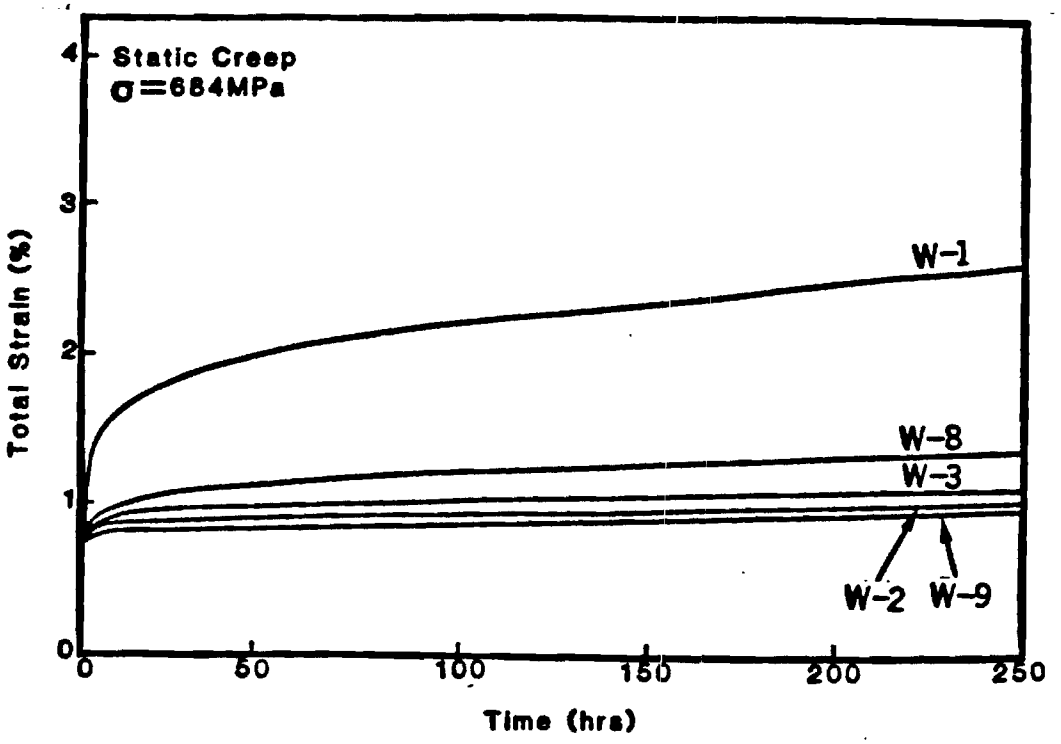

Figure 34. Static creep results at 684 MPa (90% of W-1 yield strength) for the different microstructures.

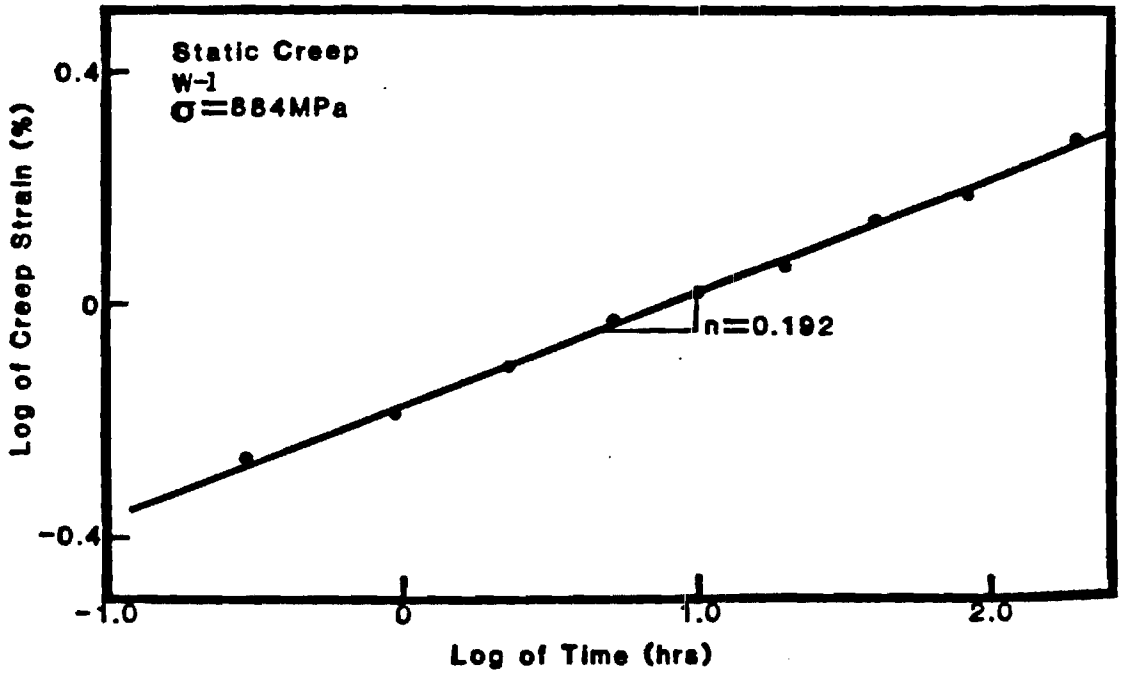

Figure 35. A log-log plot of creep strain vs. time for W-1 Ti-6211 crept at 684 MPa.

TABLE V. Time Exponent in Creep Strain/Time Relationship

Specimen Designation	Creep Stress (MPa)	Time Exponent (n)
W-1	684	0.19
W-2	684	0.10
W-3	684	0.09
W-8	684	0.06
W-9	684	0.04

For creep tests at high stresses near the yield stress, a tertiary stage creep might occur. Figure 36 shows creep curves for the four microstructures. Specimen W-1 shows an early onset of tertiary creep compared with cndition W-2 and W-3. Specimen W-3 shows an even shorter time to the onset of tertiary creep (too short to be included in the plot). It is believed that easy void formation at the grain boundary alpha/matrix interface in the W-8 condition, and at the grain boundary alpha/martensite plate interface in the W-9 structure, is responsible for the early onset of tertiary creep. Void formation of this type has been reported for tensile samples of Ti-6Al-4V by Margolin and Mahajan (20). Evidence for this mechanism can be provided by examining the two stage replica taken from the polished gage section using the TEM, and this method will be employed in this study. In addition, strain localization which occurs in the grain boundary alpha region could also be the cause of the early onset of tertiary creep.

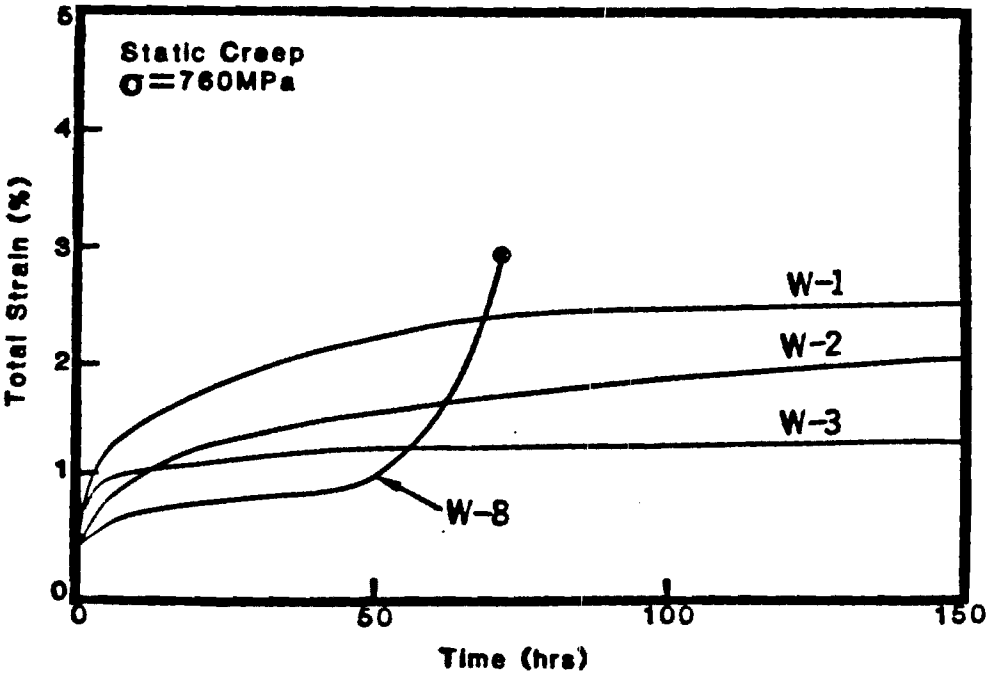

Figure 36. Static creep results at high stress. (Test for W-8 was stopped at 72 hours due to failure of strain gage).

The wave form used for the cyclic creep test is shown in Figure 37. The cyclic creep strains are plotted against the actual loading time and superimposed on the plot of the static creep curves, as shown in Figure 38. Cyclic loading accelerated creep in the forward direction; i.e., under tension. Inman and Gilmore (5) concluded from their studies on Ti-6Al-4V under dead weight torsion loading, that even at a stress well below the yield strength creep was accelerated in the forward direction when it was preceded by loading in the reverse direction. Although our studies have not involved any compressive loading cycle, dislocation motion in the unloading half cycle is probably different from that under tension, and may affect the creep behavior under tensile loading. Thin foil TEM will be used to characterize the dislocation substructures developed with and without cyclic loading in order to elucidate this point.

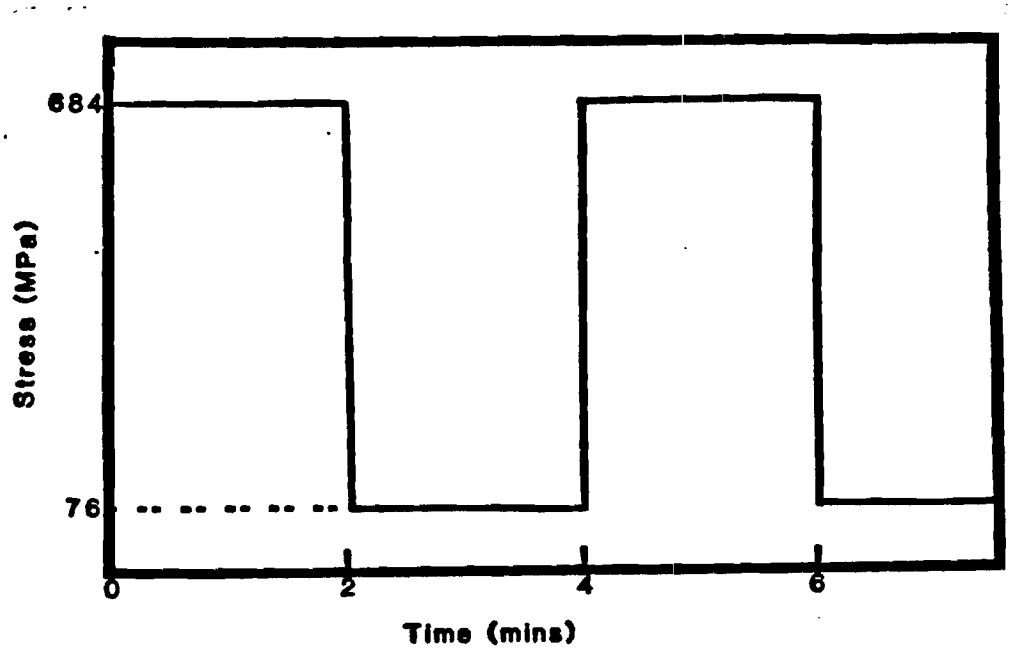

Figure 37. Loading spectrum for cyclic creep.

Surface replicas of specimens W-1 and W-8 (crept at 684 MPa with creep strains of 2.0% and 0.9%, respectively) were used for surface damage characterization. Slip lines and small steps at colony boundaries were observed. No offsets of the inscribed scratches were noted indicating that grain boundary sliding did not occur. Chakrabarti and Nichols (21) studied the surface deformation of crept samples by inscribing a grid on a flat gage section sample and examining the grid distortion after creep. Using this method they were able to detect grain boundary sliding for samples crept at 450K with 1.25% creep strain. Grain boundary sliding may be more difficult for large prior beta grained material tested at low temperatures. However, alpha-beta interface sliding and grain boundary sliding at room temperature have been reported by Boreslack and Mahajan (22) in a Ti-4.5Al-5Mo-1.5Cr (Corona 5) weld zone. Consequently, careful surface preparation and more observations are necessary before we can conclude whether or not grain boundary sliding is a significant factor in room temperature creep in Ti-6211.

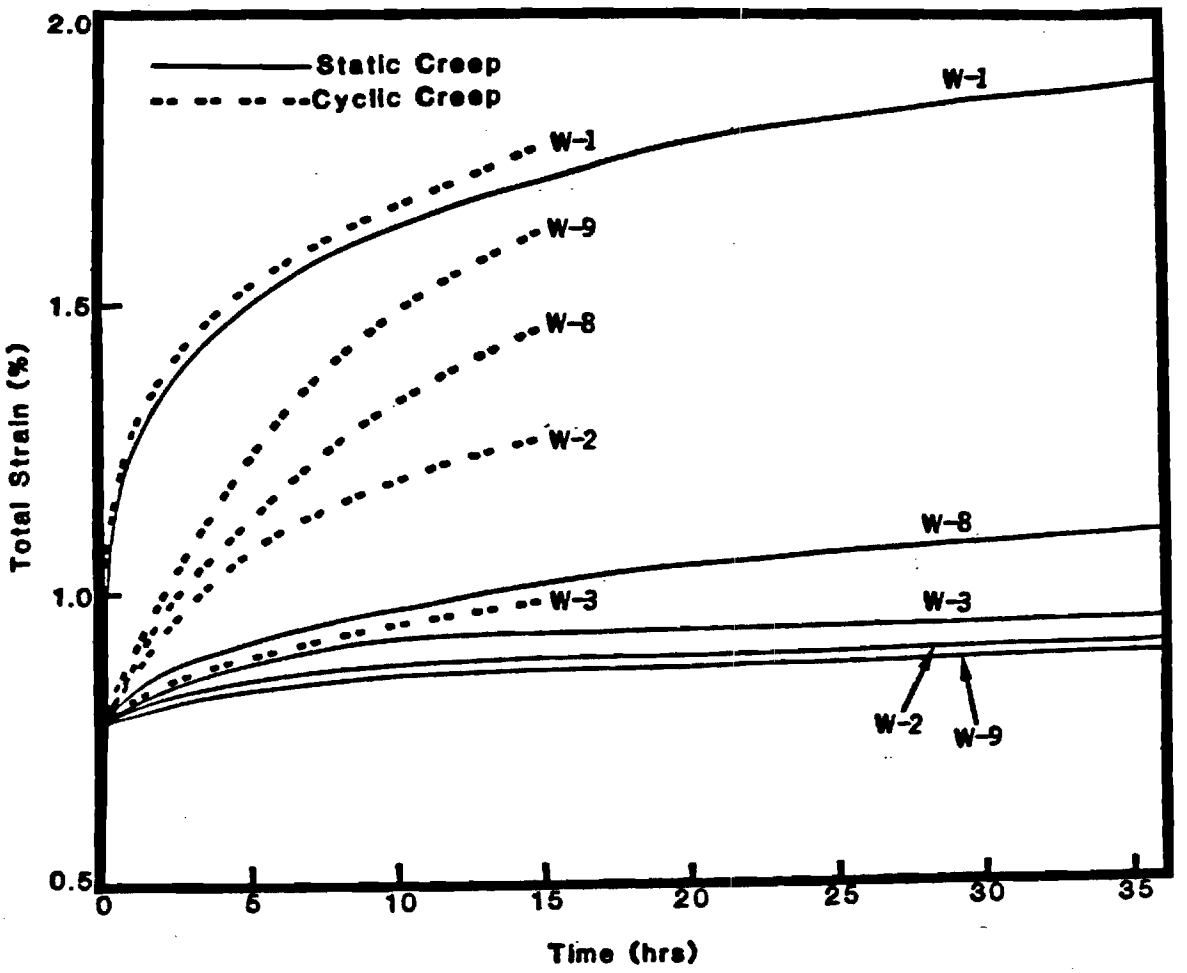

Figure 38. Comparison of cyclic creep with static creep. σ = 684 MPa for static creep. The stress condition for cyclic creep is shown in Figure 37 with a peak strength of 684 MPa.

Fatigue

Microstructure. Figure 39a shows the Widmanstatten alpha + beta microstructure of the W-1 beta processed plate. The transmission electron micrograph of 39b illustrates the discontinuous beta phase between alpha platelets. When the W-1 condition is annealed at 970°C, the volume fraction of the beta phase increases, and transforms to the random platelet martensite phase upon quenching as shown in Figure 39c. The equiaxed alpha microstructures, produced by the ITMT processing and recrystallization treatments, are shown in Figure 39d and e. The dark areas in Figure 39e are fine Widmanstatten alpha + martensite. These structures are continuous around the equiaxed alpha grains. The alpha phase represents about 90 volume percent of the total. The alpha grains are approximately 4 μm in size, and the Widmanstatten alpha + martensite regions are about 0.62 μm thick. Ti_3Al was not detected after aging at 500°C for 2 hours for either type of microstructure, although Williams (23) has suggested that Ti Al can precipitate in the alpha phase and result in increased strength during aging.

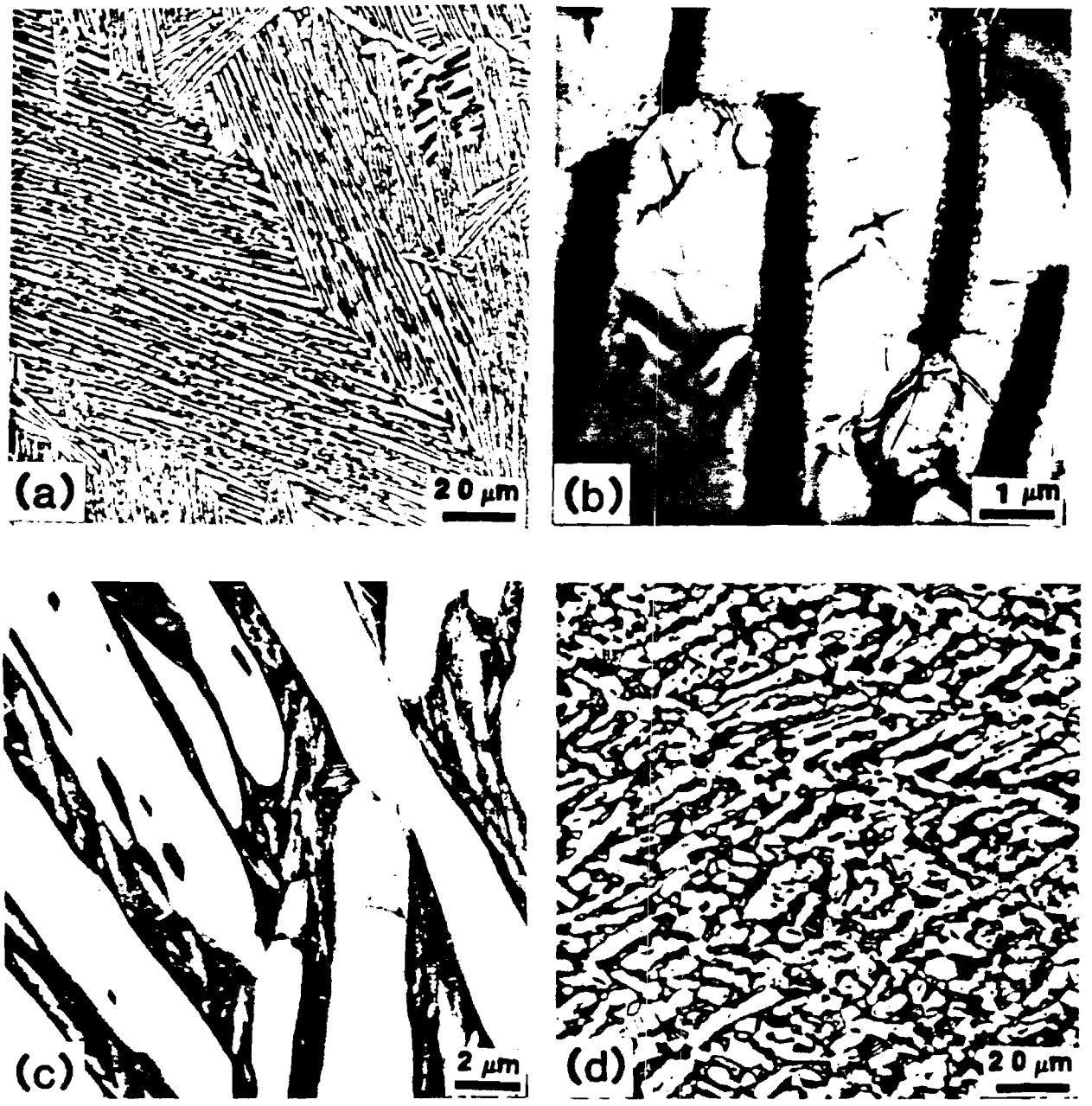

Figure 39. (a) optical micrograph shows the Widmanstatten alpha + beta structure of the W-1 Ti-6211; (b) TEM shows dislocation networks (arrow) connecting the discontinuous beta plates; (c) volume percent of beta increases, and then transforms to martensite during the W-10 treatment; (d) ITMT processing + recrystallization treatment results in an equiaxed alpha structure; (e) TEM shows the alpha grain is surrounded by Widmanstatten alpha + martensite.

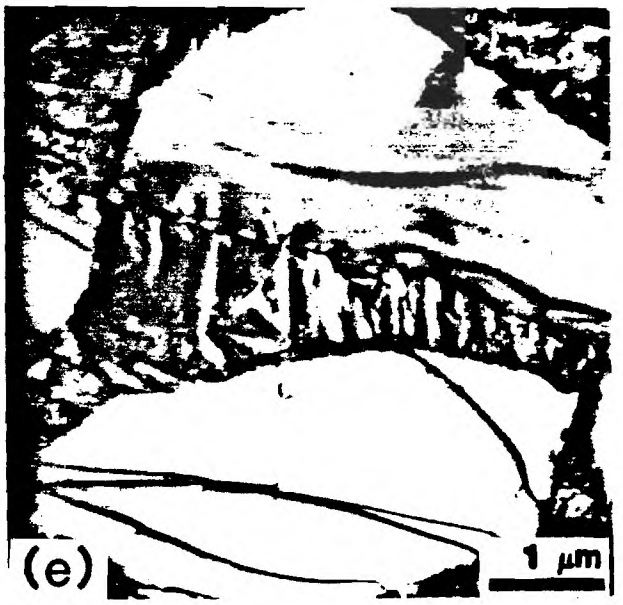

Figure 39. Continued.

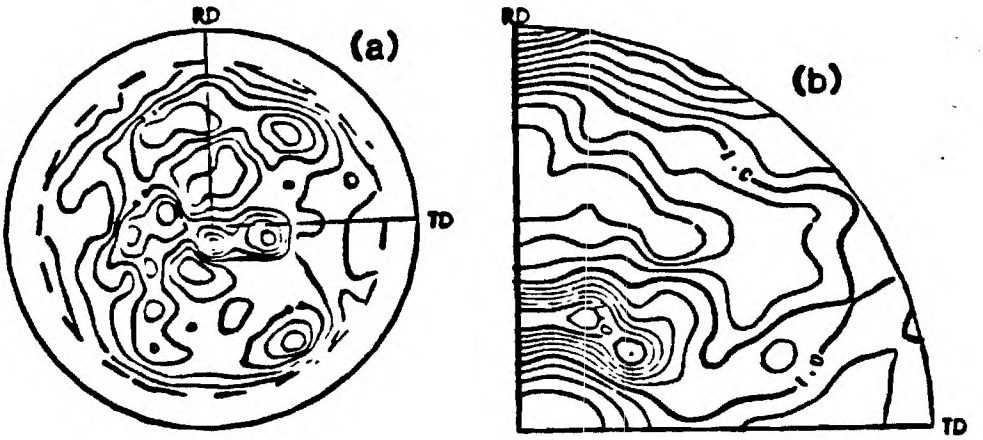

Figure 40. (a) $(10\bar{1}1)$ pole figure displays the nearly random texture of the W-1 Ti-6211 at plate surface; (b) at plate center, a weak transverse texture $(11\bar{2}0)[10\bar{1}0]$.

Texture. The pole figures show that the preferred orientation at the center of the W-1 plate is different from that at the surface. Figure 40a and 40b represents the $(10\bar{1}1)$ pole figures of the plate surface and plate center, respectively. The surface texture is nearly random and is characteristic of that

produced by beta processing. The texture averaged through the thickness exhibits a weak $(11\bar{2}0)[10\bar{1}0]$ transverse texture which may have resulted from the finishing operation being conducted slightly below the beta transus. The preferred crystallographic texture remains unchanged during the W-10 treatment. The (0002) and $(10\bar{1}1)$ pole figures of both the 850°C cross rolled and the 950°C unidirectional rolled plates are given in Figure 41. The rolling direction is parallel to $[10\bar{1}0]$. These results confirm that the appropriate ITMT processing and recrystallization treatment develops the desired basal and transverse textures.

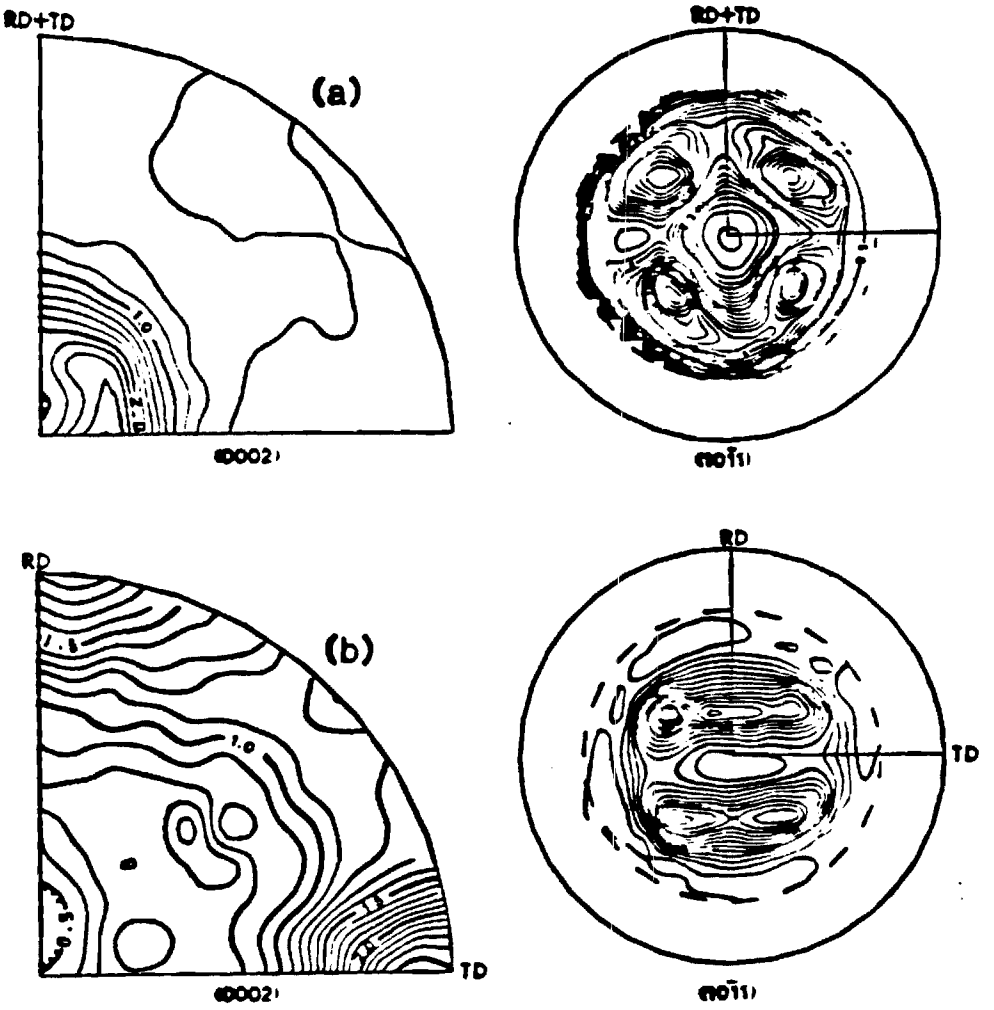

Figure 41. (a) (0002) and $(10\bar{1}1)$ pole figures of the E-2 Ti-6211 show the basal texture; (b) (0002) and $(10\bar{1}1)$ pole figures of the E-3 Ti-6211 show the transverse texture.

Monotonic Properties. The monotonic properties of Ti-6211 for the different conditions are listed in Table VI. The tensile properties of the W-1 plate are the same in the RD and TD directions. The W-10 material was tested only in the TD since both materials possess a random texture. The basal texture of the E-2

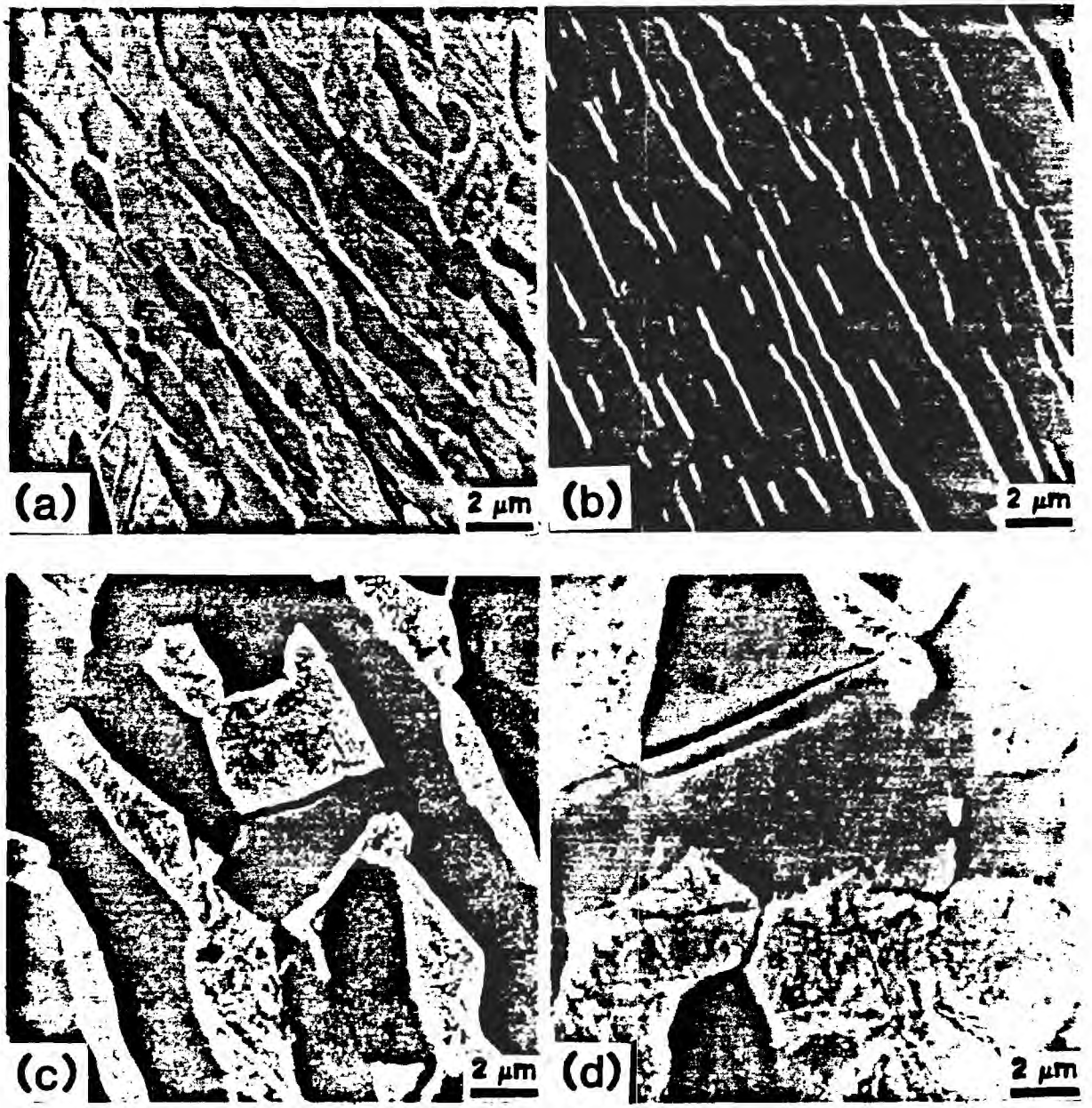

Figure 42. (a) fatigue cracks nucleate at alpha/beta interfaces for most of the Widmanstatten-type structures, except (b) cracks nucleate at slip bands when the W-1 Ti-6211 is tested at 1.5% total strain amplitude; (c) cracks nucleate at interfaces for most of the E-2 and E-3 Ti-6211, except in (d) the E-3 Ti-6211 when stressed parallel to the RD, the cracks nucleate at slip bands. The SA was along the vertical direction of this figure.

TABLE VI. Monotonic Properties of Ti-6211

Alloy Condition	Stress Axis	0.2% Yield Strength MPa	Ultimate Tensile Strength MPa	Elongation %	Reduction in Area %
W-1	RD*	760	855	15.4	30.0
	TD*	799	874	14.1	28.1
W-10	TD	937	1012	12.3	31.9
E-2	TD	1010	1093	16.3	55.7
E-3	RD	998	1082	15.4	54.0
	TD	1018	1106	15.6	55.3

* RD:SA is parallel to the rolling direction
TD:SA is parallel to the transverse direction

plate also suggests isotropic tensile properties and measurements are only reported for the TD. However, the monotonic properties of the E-3 plate, which has the transverse texture, are anisotropic and results of tensile tests in both the RD and TD are given. A 22% increase in yield strength with no significant loss in ductility is achieved by W-10 treatment because the slip length is decreased from the width of a platelet colony to that of a single alpha platelet due to the ability of the interplatelet martensite to block slip. The improvement in strength can be explained in terms of a Hall-Petch type relationship.

A significant increase in strength with no loss in ductility is obtained by ITMT processing. A detailed discussion of monotonic properties can be found in last year's report.

Fatigue Properties. The low cycle fatigue cracks initiated at alpha/beta interfaces and/or slip bands, as shown in Figure 42. Nucleation of microcracks at slip bands is only observed for the W-1 plate tested at 1.5% total strain amplitude (cracks also nucleate at interfaces) or when the unidirectional-rolled material is stressed parallel to the RD. Cracks nucleate at alpha/beta interfaces for the other conditions examined. For all the microstructural modifications investigated, the incompatibility between alpha and beta (or transformed beta) phases enhances fatigue crack initiation at alpha/beta interfaces. This initiation mechanism may also be associated with an alpha/beta interface phase.

A representative cyclic stress response curve for LCF tests is shown in Figure 43. At high total strain amplitude (1.5%) the materials cyclically harden in the first few cycles as the dislocation density increases, and then soften until fracture occurs. Cyclic softening was observed during the first cycle at lower strain amplitudes. The cyclic softening may be associated with the formation of microcracks since its occurrence correlates well with the first observation of fatigue cracks.

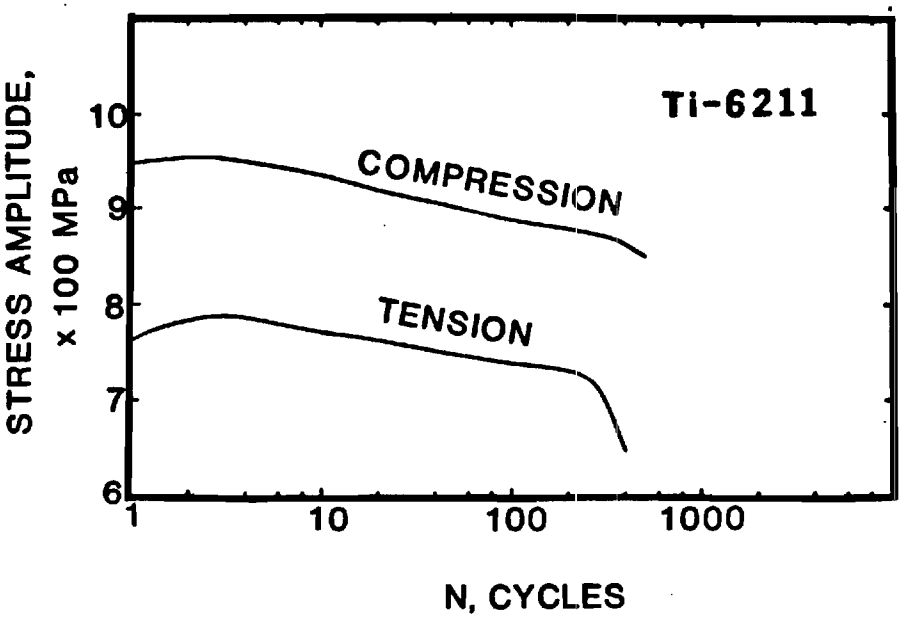

Figure 43. A representative cyclic stress response curve.

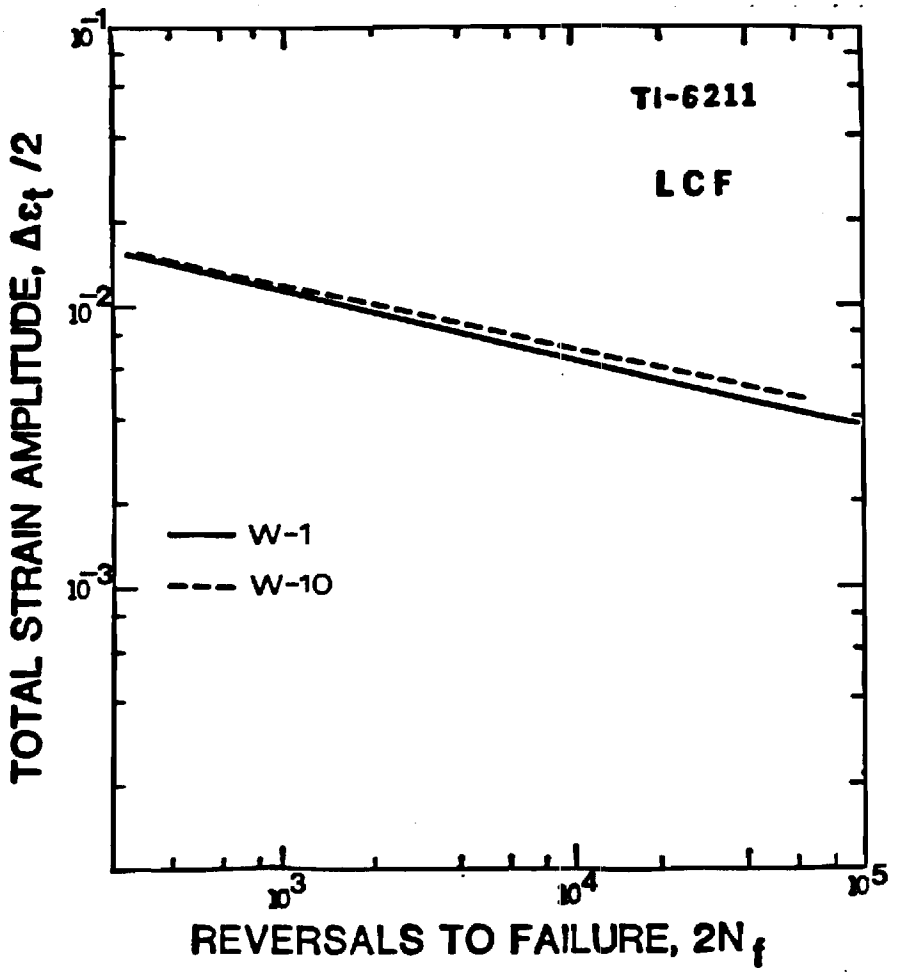

Figure 44. The relationship between total strain amplitude and reversals to failure for the W-1 and W-10 Ti-6211.

In the case of the W-1 and W-10 materials, the W-10 material has a greater fatigue resistance than the W-1 material as shown in Figure 44, where total strain amplitude is plotted versus reversals to failure. However, the strain-life of the W-1 condition is greater than that of the W-10 condition over a comparable strain range as shown in Figure 45. This result is associated with the higher incompatibility between alpha and beta (or martensite) for the W-10 condition since the beta phase has transformed to martensite during the W-10 annealing treatment. Moreover, the lower monotonic ductility of the W-10 condition when compared to that of the W-1 material (12.3% to 15% elongation) is enhanced by cyclic fatigue damage accumulation. The break points of these curves could be due to either strain localization or environmental effects (26). Figure 46 shows that the W-10 heat treatment greatly improves the fatigue propagation resistance. The fatigue threshold for the W-10 condition is about 13 MPa $m^{\frac{1}{2}}$ and about 6.5 MPa $m^{\frac{1}{2}}$ for the W-1 condition. This improvement can be correlated with the occurrence of fatigue crack closure and fracture mode.

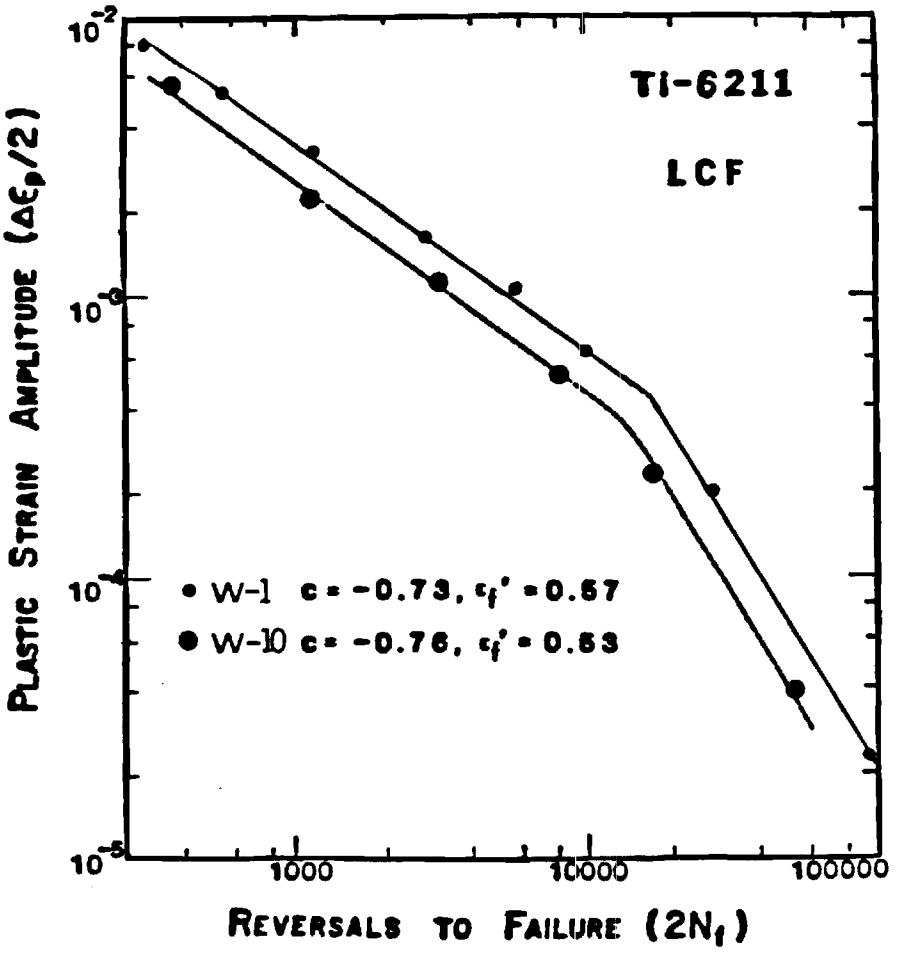

Figure 45. Strain-life curves for the W-1 and the W-10 Ti-6211.

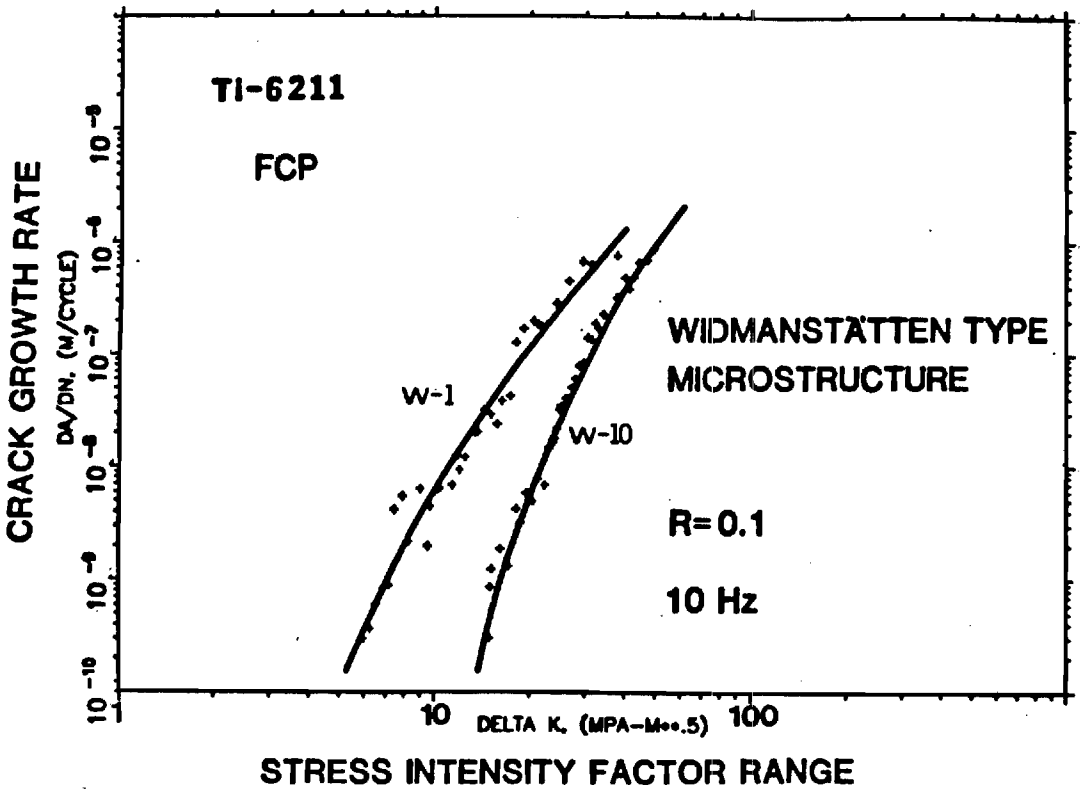

Figure 46. Fatigue crack propagation behavior for the W-1 and W-10 Ti-6211

The phenomenon of fatigue crack closure during cyclic tensile loading has been observed in a variety of materials (27-30). The fatigue crack remains closed at the crack tip even though the specimen remains in tension. Thus, the fatigue crack growth rate (FCGR) is more adequately expressed in terms of effective stress intensity factor, ΔK_{eff}, rather than the applied stress intensity factor, ΔK_{app}. The factors ΔK_{app} and ΔK_{eff} can be expressed in the form:

$$\Delta K_{app} = K_{max} - K_{min}$$
$$\Delta K_{eff} = K_{max} - K_{op} \qquad [2]$$

where K_{op} is the stress intensity factor at which the crack is first opened. In order to present the results, an effective stress range ratio, U, is then defined as (31):

$$U = \frac{\Delta K_{eff}}{\Delta K_{app}} \qquad [3]$$

The relationship between load applied and crack opening displacement (COD) obtained from the COD gage is schematically illustrated in Figure 47. The increase in specimen compliance from a closed crack to an open one results in the decrease in slope from A to D (32). Therefore, the crack is fully closed over the linear region AB. The crack opens in the curved region between B and C, and fully opens over the linear region CD. Then, the tensile load where the

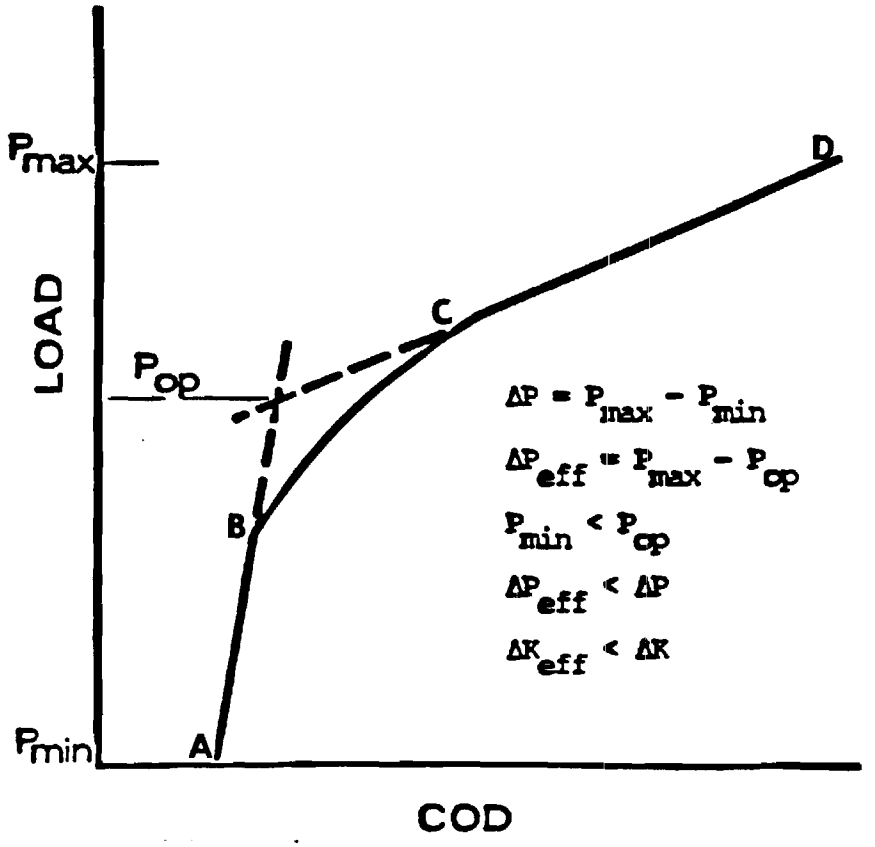

Figure 47. A schematic graph showing load applied and COD relationship.

crack first opens is determined by the interception point of the extension of AB and CD.

For the W-10 treatment, the FCGR is plotted versus ΔK_{eff} as shown in Figure 48. The value of U is in the range of 0.6-0.7. Apparently, the occurrence of fatigue crack closure[1] retards the fatigue crack growth rate significantly. Frequently, a combination of Mode I and Mode II crack growth can be observed in the near threshold region when fatigue crack closure occurs (33). The shear component (Mode II) tends to produce points of contact which wedge the crack open. This mechanism is schematically illustrated in Figure 49. The optical micrograph of Figure 49b reveals this phenomenon for the W-10 condition at about 15 MPa $m^{\frac{1}{2}}$. Although the degree of fatigue crack closure for the W-1 condition is not determined at this time, it is believed that it does occur. Therefore, the W-10 condition probably still has a better FCP resistance than the W-1 condition.

Figure 50 shows that the equiaxed alpha structures have a greater strain-life than the Widmanstatten-type structures. This may be due to the fine

[1] This kind of closure is usually termed "roughness-induced closure."

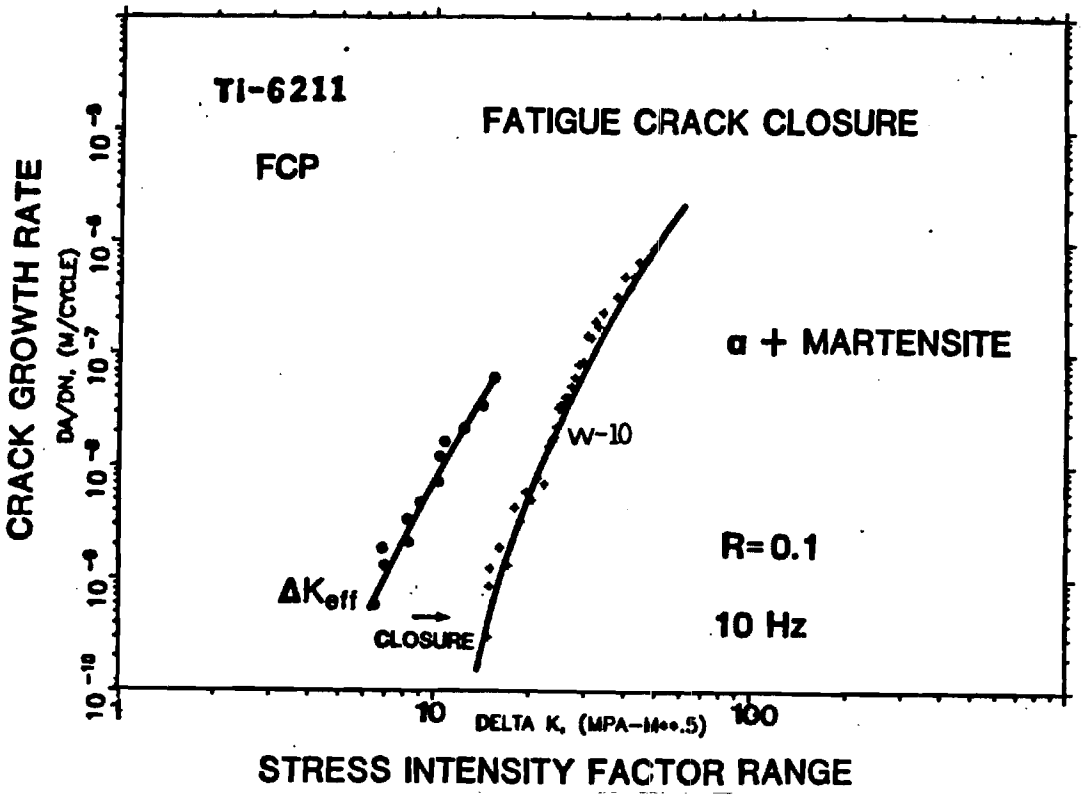

Figure 48. The effect of fatigue crack closure on the FCP behavior of the W-10 Ti-6211.

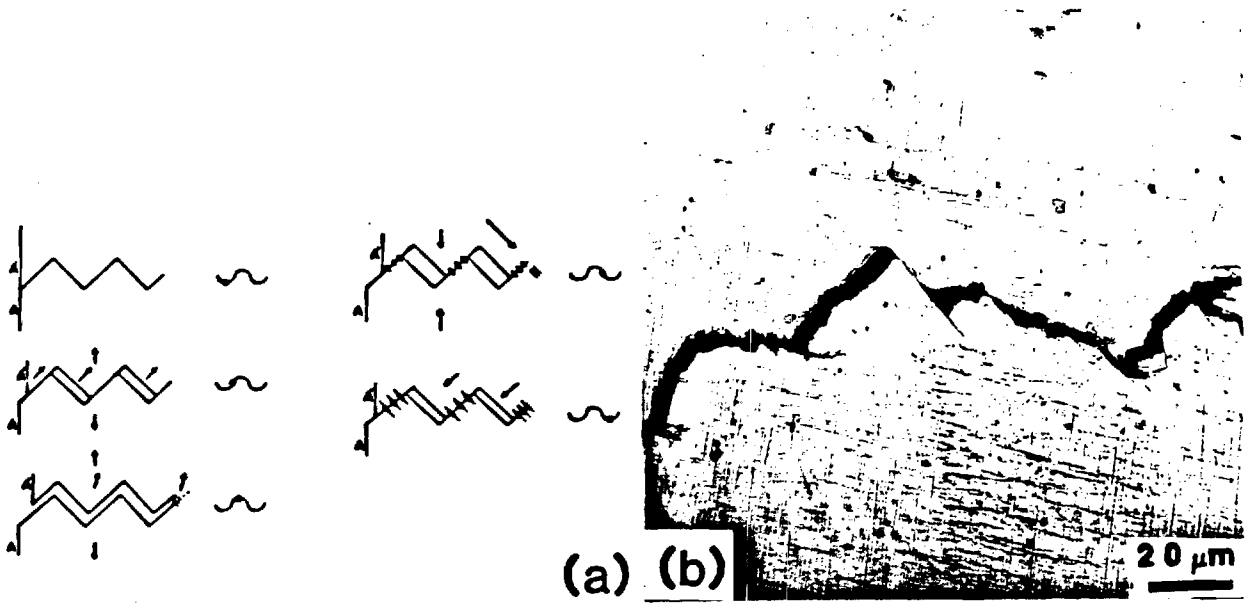

Figure 49. (a) a schematic diagram of Mode V and Mode I crack growth (ref. 33) (b) the points of contact confirms the occurrence of fatigue crack closure.

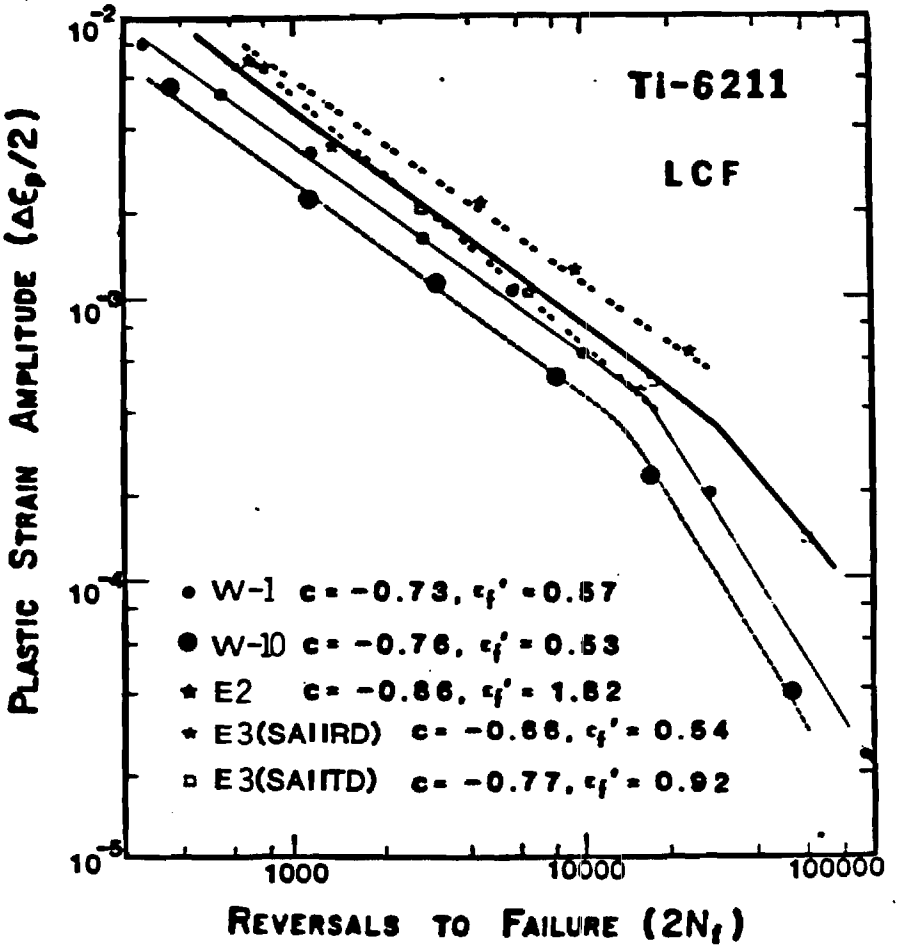

Figure 50. Strain-life curves of Ti-6211 under five conditions examined.

equiaxed structure producing a more homogeneous deformation mechanism (26). The LCF behavior for both the cross-rolled and the unidirectionally rolled material is identical, when the SA is parallel to the TD. Moreover, the transverse textured condition with the SA along the RD shows the best strain life behavior. This may be a result of the cracks nucleating at slip bands instead of at interfaces, which may reduce the degree of strain localization. Of course, this explanation is speculative at this point.

The three materials having the same equiaxed alpha microstructure have an identical FCP behavior in spite of textural variations as shown in Figure 51. The threshold value is about 6 MPa $m^{\frac{1}{2}}$. Moreover, this behavior is about the same as that of the W-1 condition, not considering crack closure.

The LCF fractography investigation reveals that the fracture features are similar for Ti-6211 under the five conditions examined. During the LCF tests, the fracture is promoted by fatigue (which is characterized by fatigue striation) and overload fracture (which is characterized by ductile dimple rupture) as shown in Figure 52. Figure 52b indicates the fatigue main crack originates at the surface. No subsurface crack initiation is observed.

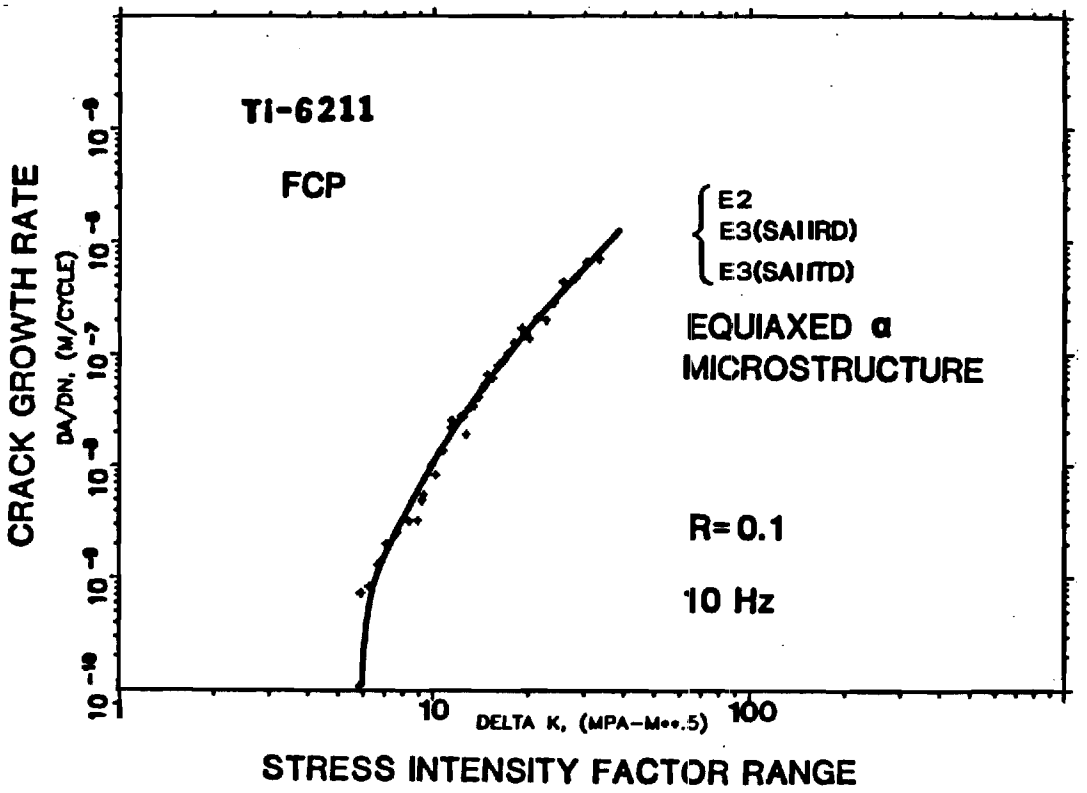

Figure 51. FCP behavior for the Ti-6211 with an equiaxed alpha microstructure.

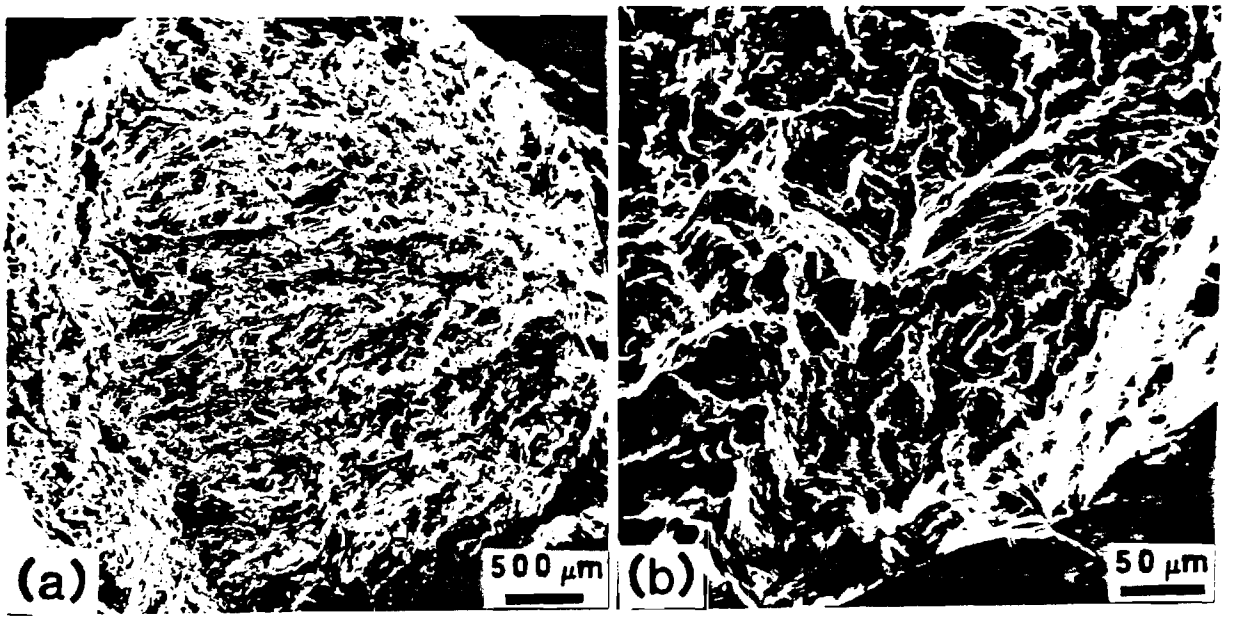

Figure 52. LCF fractography: (a) the W-1 fracture surface morphology at 0.5% $\Delta\varepsilon_t/2$, (b) crack initiating at surface at 1.5% $\Delta\varepsilon_t/2$; (c) fatigue striation is the dominant feature in fatigue region at 0.5% $\Delta\varepsilon_t/2$; (d) ductile dimple rupture predominate the overload fracture feature at 0.5% $\Delta\varepsilon_t/2$. The SA is along the vertical direction of this figure.

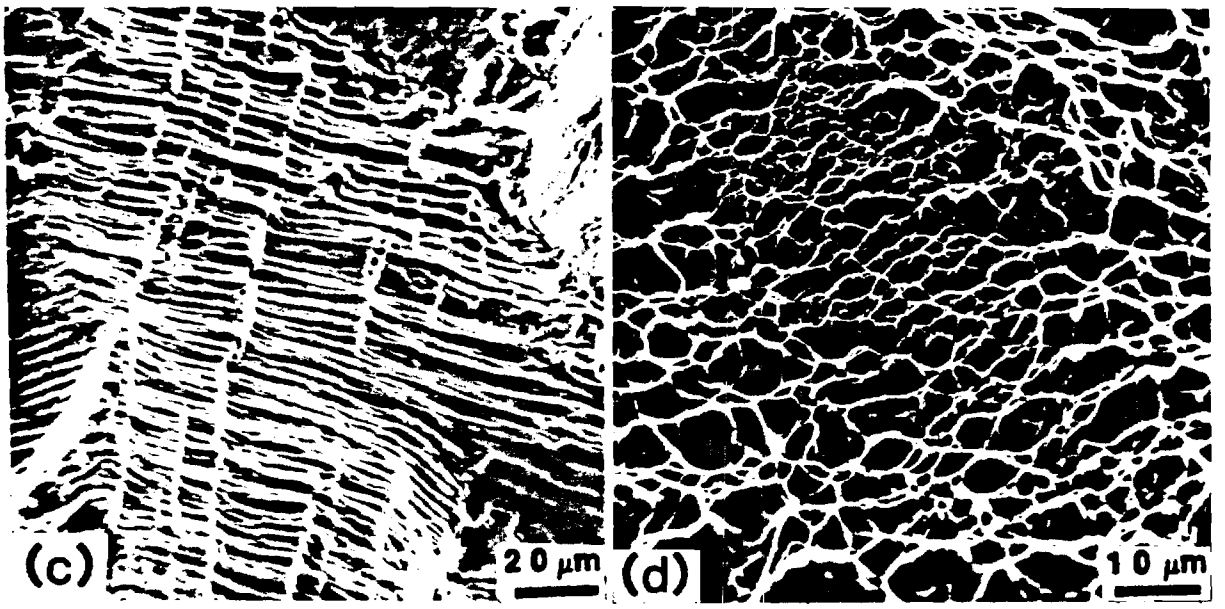

Figure 52. Continued.

Frequently, the concepts of crack bifurcation, crack path tortuosity, and secondary cracking can be accounted for reducing the FCGR in materials having lamellar-type microstructures (34). Figures 53 and 54 show that the crack path for the W-10 condition is the most tortuous one while the crack path for the equiaxed alpha structures (including E2 and E3) is fairly smooth. A less tortuous crack path propagates a longer distance than the projected linear length, therefore, yielding a faster FCGR. Moreover, Figure 54 shows that the W-10 condition has higher frequency of crack bifurication occurrence than the W-1 condition, which will dissipate more energy available for crack extension and result in a retarded crack growth. Crack branching was seldom observed for the equiaxed alpha structures despite the textural variations.

Generally, cleavage facets and ridge patterns characterize the W-1 and W-10 condition fractography, respectively, while a smooth, but faceted pattern characterizes the equiaxed alpha structure fractography.[2]

In the case of the W-1 Ti-6211, a rough and faceted fracture fractography over the entire range of ΔK is observed as shown in Figure 55. Figure 55a suggests that the rough and faceted fracture topography near the threshold regime ($\sim$6.5 MPa $m^{\frac{1}{2}}$) causes a roughness-induced crack closure. At the intermediate ΔK range ($\sim$12 MPa $m^{\frac{1}{2}}$), a river pattern characterizing cleavage facets is observed as shown in Figure 55b. The fracture surface morphology of the W-1 Ti-6211 at the fast fracture region ($\sim$25 MPa $m^{\frac{1}{2}}$) as shown in Figure 55c is characterized by duplex-slip striation and indicates a complex mechanism involving shear or secondary slip systems. Frequently, the cleavage facets can be identified as alpha + beta colony boundaries from size measurements ($\sim$45 μm). The investigation

[2] The fractography for the E-2 and E-3 is identical. Thus, equiaxed alpha is designated to refer to all three conditions examined.

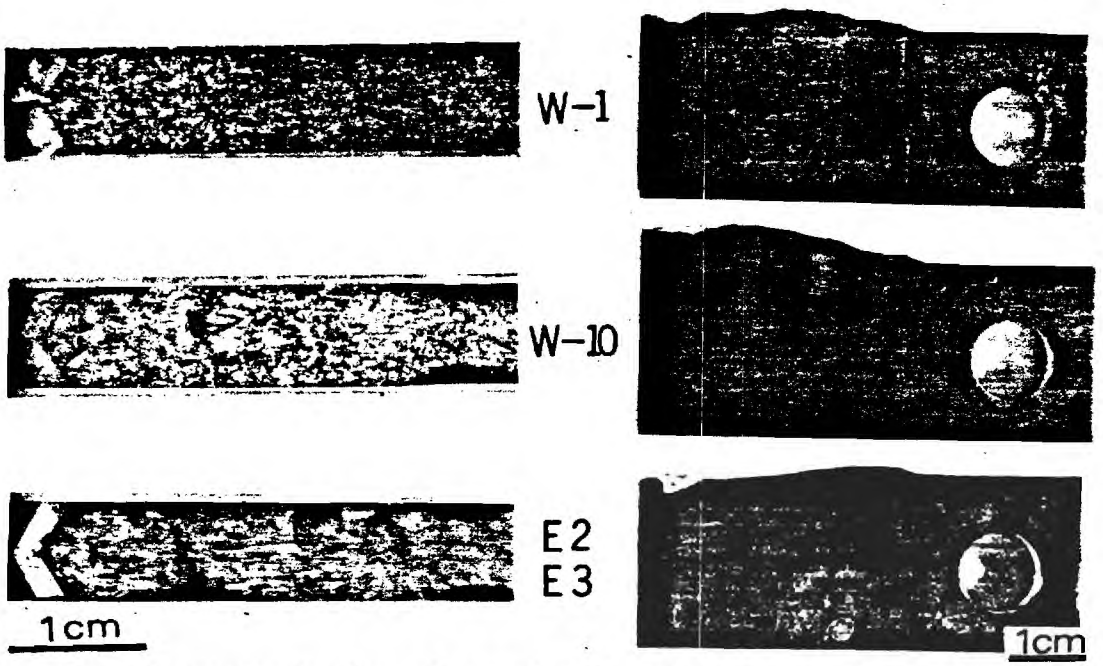

Figure 53. Macroscopic view of crack path and fracture topography for the materials tested.

of microstructure-fractography correlation evidently reveals that cracks grow primarily along colony boundaries as illustrated in Figure 55d. Therefore, the fracture mode for the W-1 Ti-6211 during the FCP is primarily intercolonial especially at low ΔK regime.

In the case of the W10 Ti-6211, a repeating reidge pattern represents the fracture topography as shown in Figure 56. The morphology is rougher and it reveals more crack branching when compared to that of the W1 condition. Moreover, the same morphology is obtained through the whole range of ΔK tested ($13 \sim 40$ MPa m). Figure 56c evidently indicates that the repeating ridge pattern is produced by ligament FCP mechanism (12) when the fractography is correlated with microstructure. In this case the random martensite phase (ligament phase which appears as white area in Figure 56c and 56d) is the crack growth barrier. Therefore, fatigue cracks grow in the alpha phase ($\sim$1.2 μm) and around the ligament phase ($\sim$1.3 μm) and result in a semi-cohesive zone. Finally, decohesion occurs and a ridge patterns results.

In the case of the equiaxed alpha structures, a smooth and faceted surface is is obtained over the entire range of ΔK tested as illustrated in Figure 57. It is believed that the facets which are about the same size as alpha + martensite phase ($\sim$5 μm) are produced by ligament phase mechanism. The fatigue crack may propagate in the alpha phase and fracture in the alpha + martensite region; i.e., the legament phase, as shown in Figure 57c and 57d. Moreover, the secondary cracking is frequently observed occurring in the alpha phase.

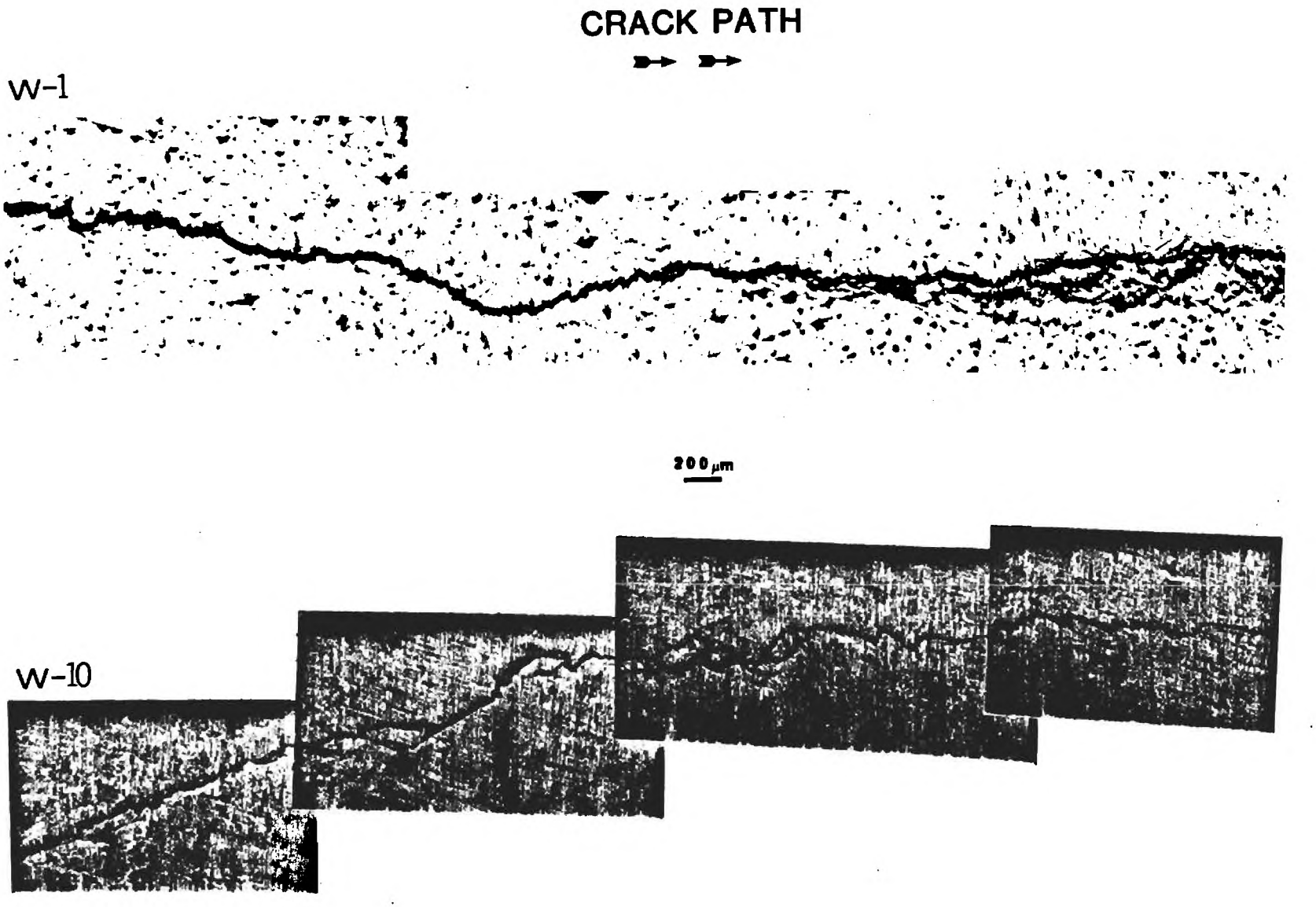

Figure 54. A comparison of crack path tortuosity and crack branching between the W-1 and the W-10 Ti-6211.

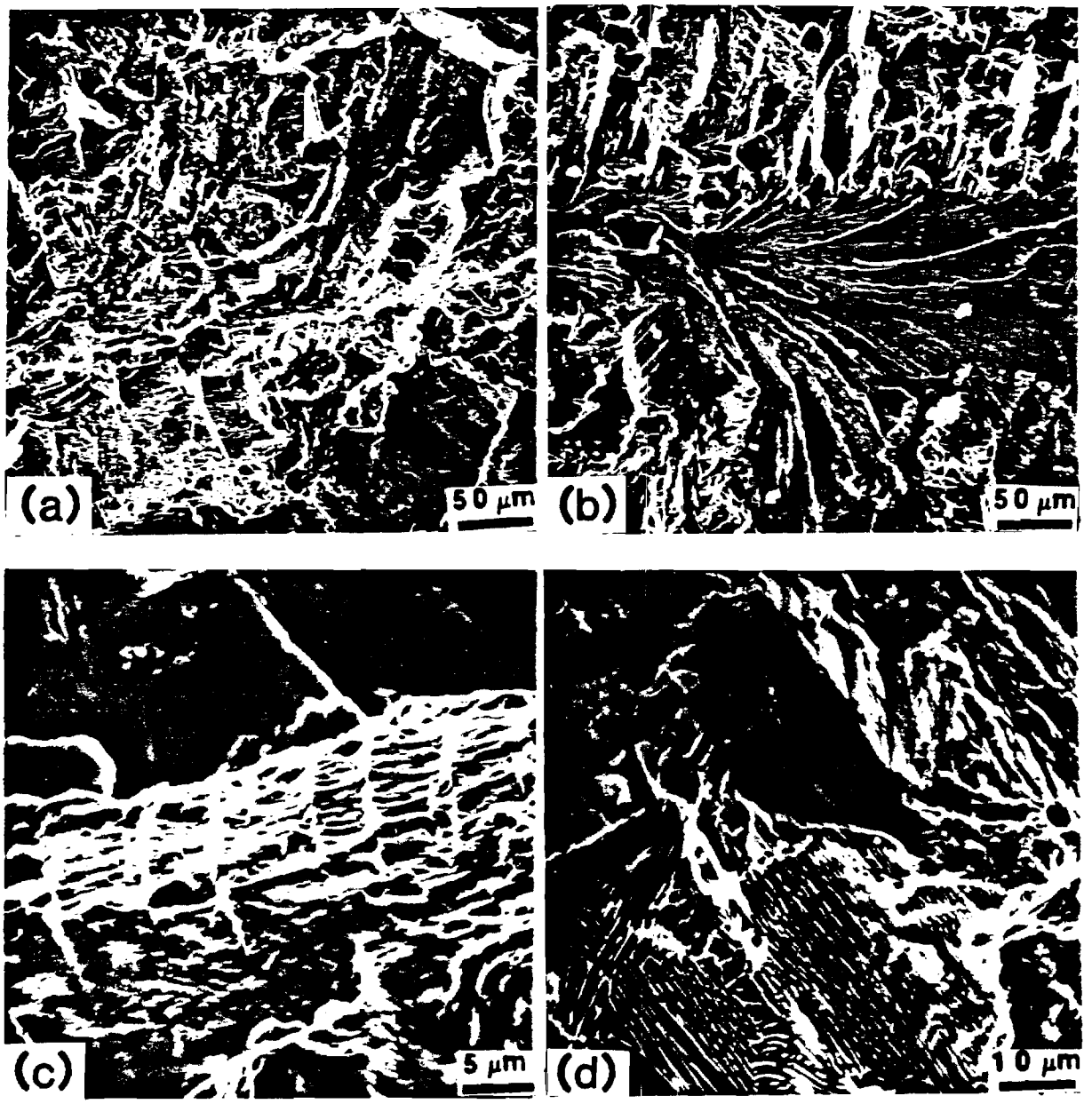

Figure 55. The FCP fractography and fracture mode of the W-1 Ti-6211:
(a) near threshold regime (∿6.5 MPa $m^{\frac{1}{2}}$) and FCGR∿2x10^{-10}m/cycle;
(b) at intermediate ΔK regime (∿12MPa $m^{\frac{1}{2}}$) and FCGR∿2x10^{-8}m/cycle;
(c) at fast fracture regime (∿25 MPa $m^{\frac{1}{2}}$) and FCGR∿2x10^{-7}m/cycle;
(d) fracture mode is intercolonial (ΔK∿6.5 MPa $m^{\frac{1}{2}}$, and FCGR∿2x10^{-10} m/cycle). The crack advanced from left to right.

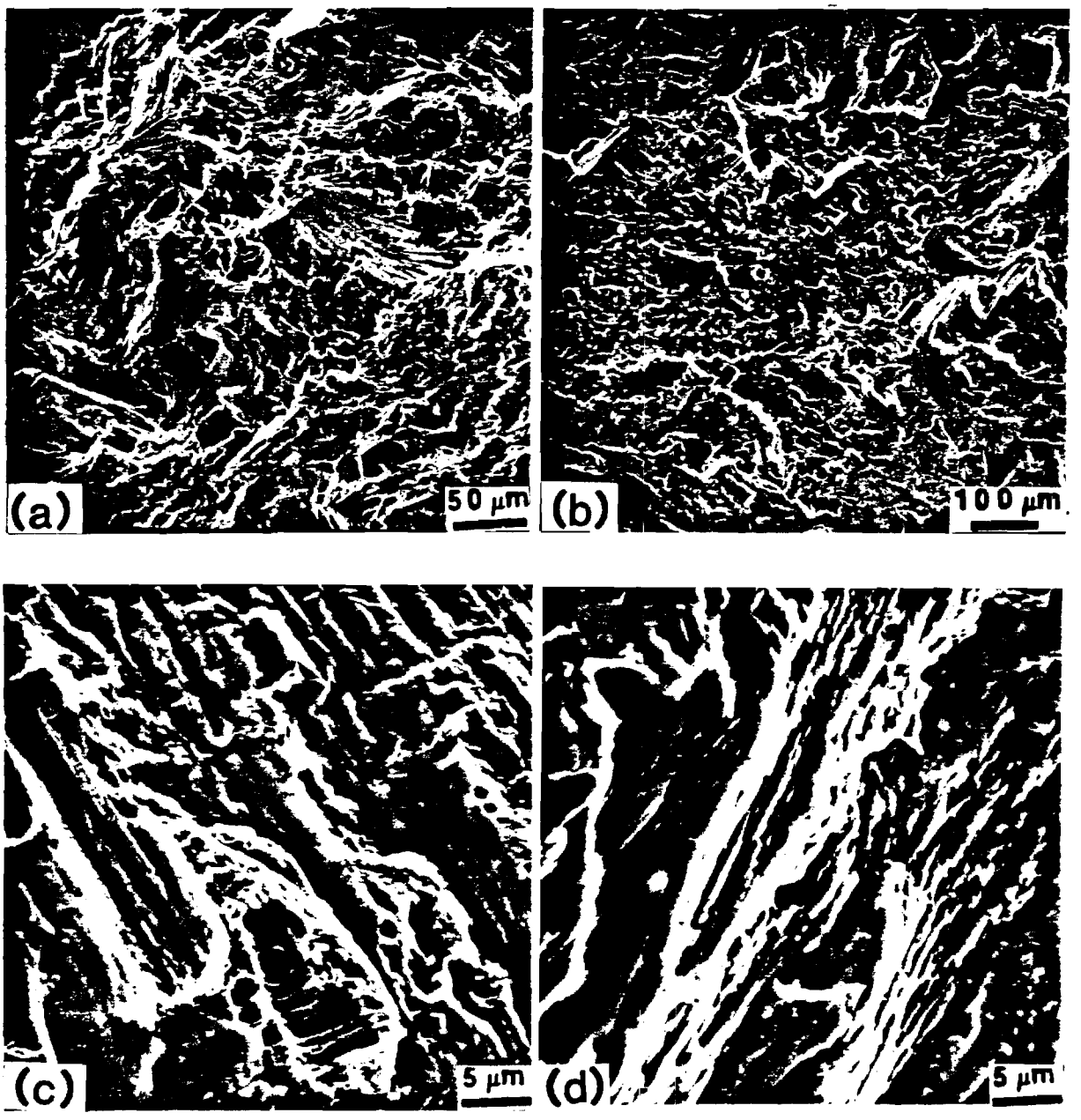

Figure 56. The FCP fractography and fracture mode of the W-10 Ti-6211: (a) near threshold regime (∿13 MPa $m^{\frac{1}{2}}$) and FCGR $2x10^{-10}$m/cycle; (b) at intermediate ΔK regime (∿25 MPa $m^{\frac{1}{2}}$) and FCGR $2x10^{-7}$m/cycle; (c), (d) facets are produced by ligament phase mechanism, alpha + martensite phase is the crack growth barrier. (c) and (d) reveal the fracture mode at (a) and (b), respectively. The crack advanced from left to right.

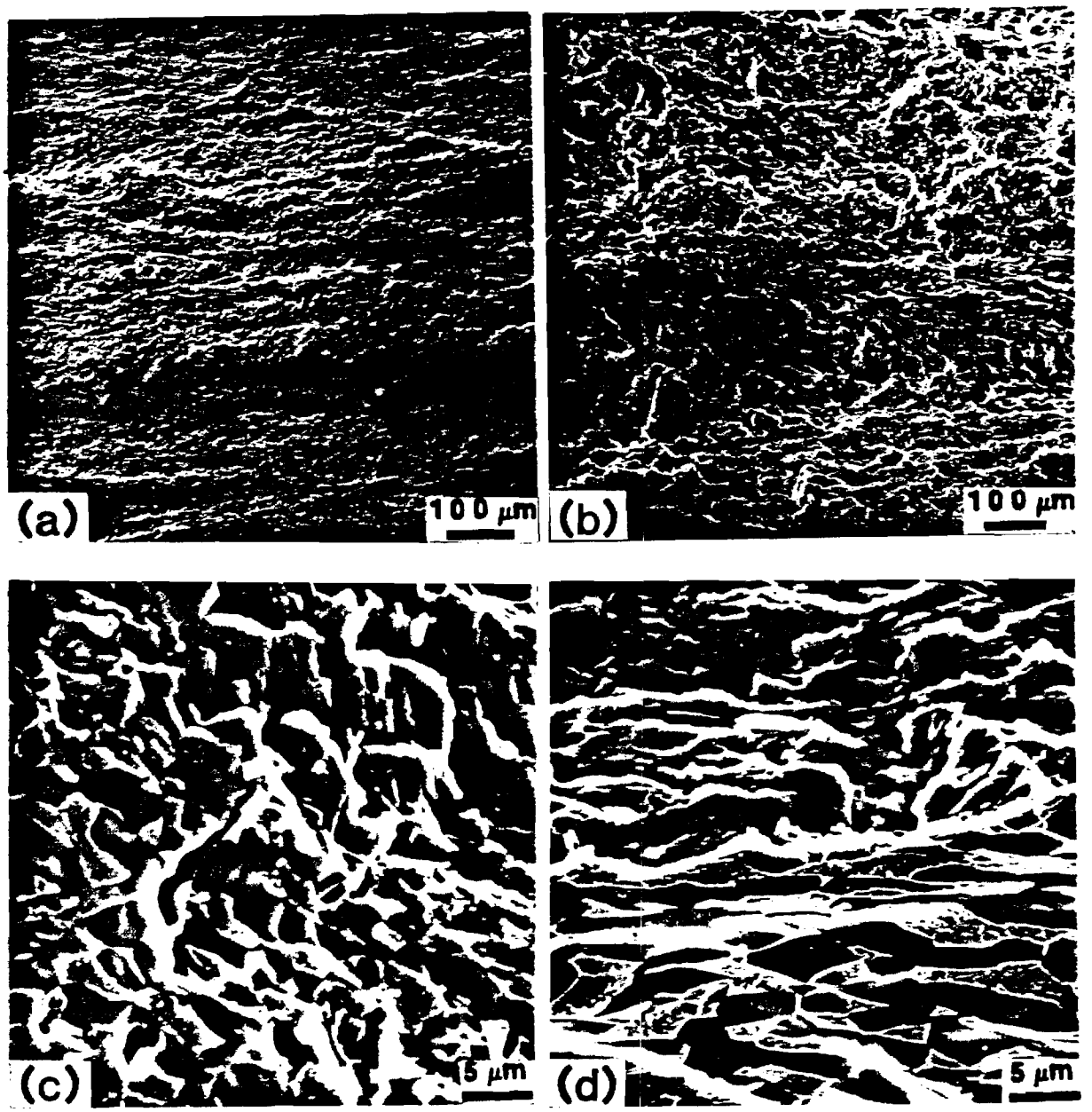

Figure 57. The FCP fractography and fracture mode of the equiaxed alpha structured Ti-6211: (a) near threshold regime ($\sim$6 MPa $m^{\frac{1}{2}}$) and FCGR is $\sim 2 \times 10^{-10}$ m/cycle; (b) at intermediate ΔK regime ($\sim$12 MPa $m^{\frac{1}{2}}$) and FCGR is $\sim 6 \times 10^{-7}$ m/cycle; and (c), (d) facets are produced by ligament phase mechanism. Alpha + martensite phase is the crack growth barrier. (c) and (d) reveal the fracture mode at (a) and (b) respectively. The crack advanced from left to right.

Conclusions

Hot Ductility

1. The hot ductility dip experienced by thermally cycled Ti-6211 synthetic weld heat-affected zone "Gleeble" specimens between 750-850°C corresponds to a change from fracture in the base metal at lower temperatures to fracture in the weld zone in the temperature range of the ductility dip.

2. Low ductility fracture in the weld zone at 800°C occurs by void formation resulting in ductile rupture along prior beta grain boundaries.

3. Low ductility intergranular fracture is microstructure controlled rather than the result of rapid thermal cycling.

4. Equiaxed alpha phase morphologies show excellent ductility in the temperature range of the ductility dip, while Widmanstatten + grain boundary alpha morphologies produce low ductility intergranular fracture.

5. Beta grain shape together with alpha phase morphology are critical factors in producing low ductility intergranular fracture at 800°C.

6. For Widmanstatten + grain boundary alpha morphologies with elongated prior beta grains such as those found in beta processed plate material, strain localization within the grain boundary alpha phase is limited due to low resolved shear stress within the grain boundary layer.

7. For Widmanstatten + grain boundary alpha morphologies with equiaxed beta grains, the grain boundary alpha orientation results in significant strain localization within the grain boundary layer, resulting in void formation along the prior beta grain boundaries and subsequent ductile rupture.

8. For Widmanstatten + grain boundary alpha phase morphologies, transformed beta phase has no effect on hot ductility behavior.

9. Subsequent cooling rate after temperature excursion above the beta transus temperature is not critical in producing low hot ductility.

10. Martensitic specimens quenched from above the beta transus rapidly form grain boundary alpha phase within the temperature range of the hot ductility dip, resulting in strain localization within the grain boundary alpha phase similar to that found in Widmanstatten + grain boundary alpha phase morphologies.

11. Sulfur segregation to prior beta grain boundaries during high temperature exposure is not believed to be a critical factor involved in producing low hot ductility.

Creep Behavior

1. Titanium 6211 shows an appreciable amount of creep at room temperature and the creep strain/time relationship follows a power law.

2. Creep deformation is microstructurally sensitive, and the creep resistance can be changed by thermal treatments.

3. Cyclic loading accelerates creep at room temperature.

Fatigue

1. A high strength, high ductility and high strain life combination is achieved by developing an equiaxed alpha microstructure completely surrounded by a strong alpha + martensite deformation barrier by appropriate ITMT processing and recrystallization treatments.

2. LCF microcracks were observed to nucleate at alpha/beta interfaces or slip bands.

3. Heat treatment W-10 results in an increase of 22% in yield strength without loss of ductility. However, increase in incompatibility between the alpha and beta phases decreases the LCF strain-life.

4. The W-10 heat treatment improves the FCP resistance over the W-1 condition by changing the fracture mode from fracture along colony boundaries to ligament phase fracture mechanism.

5. For the W-1 condition, the platelet colony boundary is the easy crack path, producing a faceted cleavage pattern in which facets are identified as platelet colonies.

6. A ridge pattern is the characteristic fractography for the W-10 condition material, and the decohesion zone is identified as the martensite phase, i.e., martensite is the strong crack growth barrier.

7. The greater FCP resistance in the W-10 condition is partially due to the occurrence of the roughness-induced fatigue crack closure.

8. The FCP behavior of the equiaxed alpha microstructure is nearly the same as that of the W-1 condition without the concern of fatigue crack closure.

9. The fracture topography of the equiaxed alpha structures is characterized by a smooth, but faceted pattern and the alpha + martensite region is the fatigue crack propagation barrier.

REFERENCES:

1. J. Gordine, Weld. J., 53 (1974) p. 117.

2. R. E. Lewis, Technical Report, LMSC-D623740, Lockheed Missles & Space Company, December 1978.

3. A. J. Hatch, J. M. Partridge, and R. G. Broadwell, J. Mater., 2 (1967) p. 111.

4. A. W. Thompson, B. C. Odegard, Met. Trans., 4A (1973) p. 899.

5. M. A. Inman, C. M. Gilmore, Met. Trans., 10A (1979) p. 419.

6. W. H. Reimann, J. Mater., 6 (1971) p. 926.

7. B. C. Odegard, A. W. Thompson, Met. Trans., 5A (1974) p. 1207.

8. H. P. Chu, J. of Materials, 5 (1970) p. 633.

9. J. C. Chesnutt, R. A. Spurling, Met. Trans., 8A (1977) p. 216.

10. E. S. Meieran, Rev. Sci. Ins., 33 (3) (1962) p. 319.

11. ASTM Standards, E8-69 (1974) p. 90.

12. ASTM Standards, E399-74 (1974) p. 561.

13. B. I. Savelor, Fundamentals of Cyclic Stress and Strain, University of Wisconsin Press, Madison, WI (1972) p. 45.

14. M. J. Blackburn, J. C. Williams, Trans. TMS-AIME, 239 (1970) p. 287.

15. E. D. Hondros, M. P. Seah, Int. Met Rev, Review 222 (Dec. 1977)

16. E. A. Starke, S. B. Chakrabortty, F. S. Lin, A. Geisler, unpublished research.

17. E. A. Starke, G. Lutjering, Fatigue and Microstructure, ASM, (1979) p. 205.

18. M. A. Greenfield, H. Margolin, Met. Trans, 2 (1971) p. 841.

19. M. A. Greenfield, H. Margolin, Met. Trans, 3 (1972) p. 2649.

20. H. Margolin, Y. Mahajan, Met. Trans.., 9A (1978) p. 781.

21. A. K. Chakrabarti, E. S. Nichols, Titanium 80, Proc. Fourth Int. Conf. on Titanium, AIME, (1980) p. 1081.

22. W. A. Baeslack, Y. Mahajan, Met. Trans., 11A (1980) p. 1234.

23. J. C. Williams, Titanium Science and Technology, ed. by R. I. Jaffee and H. Mi Burte, 3, Plenum Press, NY (1973) p. 1433.

24. F. S. Lin, E. A. Starke, Jr., S. B. Chakrabortty, A Gysler, ONR C-N00014-79-C0207.

25. J. C. Chesnutt, R. A. Spurling, Met Trans., 8A (1977) p. 216.

26. E. A. Starke, Jr., G. Lutjering, Fatigue and Microstructure, ed. M. Meshii, ASM (1978) p. 205.

27. W. Elber, Damage Tolerance in Aircraft Structures, ASTM STP 486, (1971) p. 230.

28. P. E. Irving, J. L. Robinson, C. J. Beevers, Int. J. Frac. Mech., 9 (1973) p. 105.

29. N. Walker, C. J. Beevers, Fatigue of Eng. Mat. Structure, 1 (1979) p. 135.

30. C. J. Beevers, Proc. Int. Symposium on "Fatigue Threshold," June 1-3, 1981, Stockholm, Sweden.

31. V. Bachmann, D. Munz, Int. J. of Fracture, 11 (1975) p. 713.

32. M. D. Halliday, C. J. Beevers, J. Testing Evaluation, 9 (4) (1981) p. 203.

33. K. Minakawa, A. J. McEvily, Proc. Int. Symposium on "Fatigue Threshold," June 1-3, 1981, Stockholm, Sweden.

34. A. W. Thompson, J. C. Williams, J. D. Frandsen, J. C. Chesnutt, Titanium and Titanium Alloys, Scientific and Technological Aspects, ed. J. C. Williams, A. F. Belov, 1 Plenum Press, (1976) p. 691.